Hydrocarbon Ionomer Catalyst Layers in Proton- and Anion-Exchange Membrane Fuel Cells

by

Benjamin Britton

B.Sc. (Chemistry), Trinity Western University, 2009
B.A. (English Literature), Trinity Western University, 2009

Thesis Submitted in Partial Fulfillment of the
Requirements for the Degree of
Doctor of Philosophy

in the
Department of Chemistry
Faculty of Science

SIMON FRASER UNIVERSITY
Fall 2018

Approval

Name: **Benjamin Britton**

Degree: **Doctor of Philosophy**

Title: **Hydrocarbon Ionomer Catalyst Layers in Proton- and Anion-Exchange Membrane Fuel Cells**

Examining Committee:

Hua-Zhong Yu
Chair
Professor

Steven Holdcroft
Senior Supervisor
Professor

Michael Eikerling
Supervisor
Professor

Zuo-Guang Ye
Supervisor
Professor

Erik Kjeang
Internal Examiner
Associate Professor
School of Mechatronics Systems Engineering

Bruno G. Pollet
External Examiner
Professor
Department of Energy and Process Engineering,
Norwegian University of Science and Technology
(NTNU)

Date Defended/Approved: September 17th, 2018

Abstract

Through electrochemical and physical characterization, the structure and morphology of fuel cell catalyst layers and concomitant system properties were investigated, specifically the effects of 1) controlling the ratio of high-boiling solvent in catalyst ink; 2) controlling the conditions of catalyst ink deposition; and 3) altering both interfacial interactions of catalyst layers through an alternative MEA construction methodology.

Catalyst layers designed for proton-exchange membrane fuel cells (PEMFCs) incorporated a hydrocarbon ionomer (sP4c) soluble in low-boiling solvents. These were used to probe the property alterations effected by increasing ionomer coverage within the catalyst layer, and also to measure the impact an extremely small quantities (0.38 wt%) of a commonly employed high-boiling solvent, DMF, in the catalyst ink. High-boiling solvents are difficult to eliminate during electrode formation, and resultant solvent-annealed catalyst layers lost electrocatalytic surface area, resulting in markedly greater kinetic losses compared to catalyst layers formed without high-boiling solvents.

Catalyst layers designed for anion-exchange membrane fuel cells (AEMFCs) incorporating hydrocarbon ionomer in the catalyst layer (FAA-3) requiring high-boiling solvent (NMP, 2.3 wt% of total solvent) were formed over a broad array of conditions. Catalyst layers formed slowly at high temperatures to drive off high-boiling solvent displayed significantly enhanced mesoporosity, relating to enhanced transport characteristics, over solvent-annealed analogues with low mesoporosity, despite comparable total volumes. The impacts of solvent annealing on AEMFC electrode properties and resultant achievable power density and degradation were disproportionate compared to the similar PEMFC study.

A new methodology for fuel cell membrane-electrode assembly construction, direct membrane deposition (DMD), enabled lower interfacial resistances and enhanced water transport, desired properties for hydrogen fuel cells. Initially developed with inkjet printers, this adaptation to spray-coating systems addressed major scalability and reproducibility issues that caused fuel and electrical crossover. A perfluorinated sulfonic acid ionomer reference material (Nafion D520) was employed for direct comparison and highly reproducible DMDs with low fuel and electrical crossover resulted.

Keywords: PEMFC; AEMFC; DMD; catalyst layer; ionomer; fuel cell

Dedication

For Pamela Linkewich, Heidi Britton, and Steve Holdcroft – you made this possible – and in memory of Linc Alexander, who showed me that discovery is endless, lifelong joy

Acknowledgements

It takes a community to mint a doctor of philosophy, and eternal thanks to mine:

To my committee with special and continuous gratitude, Professor Michael Eikerling, Professor Zuo-Guang Ye, and most of all to Professor Steven Holdcroft, who gave me this opportunity, the freedom to investigate & collaborate, and a research path exploring the cutting edge in this exciting field that will revolutionize the energy economy.

To my incredible colleagues in the Holdcroft Group, who honed my knowledge, mercilessly questioned me, and became dear friends, especially Dr. David Novitski and Dr. Tim Peckham, both of whom offered to proof-read this thesis without my asking, despite knowing full well what that entailed, Dr. Graeme Suppes, Dr. Thomas Weissbach, Dr. Ben Zhang, Dr. Andrew Wright, Dr. Jiantao Fan, Dr. Aki Lee, and the soon-to-be Drs. Thomas Skalski, Mike Adamski, Patrick Fortin, Jon Ward, and Amelia Hohenadel.

To all within the SFU Chemistry Department who have inspired & encouraged me, in particular Professor Byron Gates, Professor Gary Leach, the inestimable Finlay MacNab, Dr. Benson Jelier, Dr. Mike Paul, the Eikerling group as a whole for being so very welcoming to me at all the electrocatalysis-related events they attended as a group and I typically alone, in particular Dr. Tasleem Muzaffar, Dr. Heather Baroody, Dr. Mohammad Eslamibidgoli, Dr. Ali Malek, and Dr. Thomas Kadyk, and to those without, especially Professor Elicia Maine, Professor Sarah Lubik, and Dr. Iain Begg.

To all the people who have trained me and made all systems go at NRC-IFCI and 4D Labs, especially Dave Edwards, Frank Orfino, and Nathanael Sieb.

To my comrades-in-arms at the University of Freiburg / IMTEK who have helped and inspired me along the way – Prof. Matthias Breitwieser and Dr. Matthias Klingele (collectively Matthias^2), Prof. Severin Vierrath, and Prof. Simon Thiele.

To my family with love, especially to my wonderful mom - Pamela Linkewich, who has constantly loved, encouraged, and supported me throughout my fourteen years of higher education; to my darling wife, Heidi Britton, whose love keeps me going each day; and to my dad Greg Britton, uncle Zach Linkewich, auntie Coby Schneider, Pat & John Sturdy, and Grandpa Jim & Grandma Silvija – your excitement at what I'm doing means the world to me.

Table of Contents

List of Tables

List of Figures

List of Symbols and Abbreviations

Symbol	Definition, Typical Units
C_{DL}	Double layer capacitance
E°	Standard potential, V
E_{cell}	Cell potential, V or mV
F	Faraday's constant, $C \cdot mol^{-1}$
i	Current, mA
j	Current density, mA/cm^2
m	Mass, mg
n	Number of electrons involved in a chemical process, mol
R	Resistance, mΩ
σ	Conductivity, $mS \cdot cm^{-1}$
t	Thickness, µm
T	Temperature, K

Abbreviation	*Definition*
AAEM	Alkaline anion-exchange membrane; see AEM
AC	Alternating current
AEM	Anion-exchange membrane, also known as AAEM, AM, HEM
AM	Anion-exchange membrane; see AEM
AST	Accelerated stress test

BOL	Beginning of life, i.e. initial operation of a fuel cell
BET	Brunauer-Emmet-Teller surface area (gas adsorption method)
CA	Chronoamperometry
CCM	Catalyst coated membrane, a method of fabricating MEAs involving the deposition of electrodes onto a membrane prior to adding GDLs to form an MEA
CCS	Catalyst coated substrate, a method of fabricating MEAs involving the deposition of electrodes onto GDL substrates and subsequent compression of these onto a standalone membrane to form an MEA
CNT	Carbon nanotube
CL	Catalyst layer
CV	Cyclic voltammetry
DC	Direct current
DMD	Direct membrane deposition, a method of fabricating MEAs
DOE	United States Department of Energy
ECSA	Electrochemically active surface area, AKA ESA
EIS	Electrochemical impedance spectroscopy
EDX	Energy-dispersive X-ray spectroscopy
EOL	End of life, i.e. degraded
ex situ	Determined outside of an operational fuel cell stack
FC	Fuel cell
FIB	Focused ion beam
FRA	Frequency-response analysis

GISAXS	Grazing-incidence small-angle scattering
GIWAXS	Grazing-incidence wide-angle scattering
GDE	Gas diffusion electrode, a catalyst layer deposited onto a GDL
GDL	Gas diffusion layer, typically describing a 2-layer system comprising macroporous layer known as the gas diffusion layer, GDL, typically carbon fiber, to face the flow field and a microporous layer, MPL, typically carbon black, to face the electrode
HEM	Hydroxide-exchange membrane; see AEM
HER	Hydrogen emission reaction
HOR	Hydrogen oxidation reaction
HFR	High-frequency resistance by EIS
iR	Resistance equivalent to HFR by current-interrupt method
in situ	Determined in an operational fuel cell stack
IV	Polarization
LFR	Low-frequency resistance
LSV	Linear-sweep voltammetry
MA	Mass Activity (W/mg Pt = kW/g Pt)
MEA	Membrane-electrode assembly
MPL	Microporous layer
Nafion®	The archetypal PFSA used in fuel cells, produced by DuPont
ND520	Nafion dispersion, 5 wt% in mixed alcohol
N211	Nafion 211 membrane, a 25 µm (1 mil) film

N212	Nafion 212 membrane, a 50 µm (2 mil) film
N117	Nafion 117 membrane, a 175 µm (7 mil) film
OCV	Open circuit voltage; occasionally open circuit potential, OCP
OER	Oxygen emission reaction
ORR	Oxygen reduction reaction
PEM	Proton-exchange membrane, a cation-exchange membrane designed for proton conductivity; the alternative ‘polymer electrolyte membrane’ is insufficiently nuanced, encompassing anion-exchange membranes
PFSA	Perfluorinated sulfonic acid, the class of polymeric, strongly acidic proton-exchange membranes and ionomers that form the present standard in proton-exchange membrane fuel cells
PFSI	Pefluorinated sulfonic acid ionomer, specific to a PFSA employed as ionomer in the catalyst layer
P_{max}	Maximum power density
Pt/C	Platinum nanoparticles on a carbon support, the standard electrocatalyst for fuel cells
PTFE	Polytetrafluoroethylene
R_{CT}	Charge transfer resistance
R_{MT}	Mass transport resistance
RH	Relative humidity, % of water vapour out of maximum water vapour at a given temperature
SA	Surface area
SANS	Small-angle neutron scattering
SAXS	Small-angle X-ray scattering

SEM	Scanning electron microscopy
slpm	Standard litres per minute, gas flow volume-corrected to STP conditions
STP	Standard temperature and pressure (273.15 K, 1 atm)
TEM	Transmission electron microscopy
WAXS	Wide-angle X-ray scattering
XRD	X-ray diffraction
XPS	X-ray photoelectron spectroscopy
wt%	Weight percent

Preface

Fuel cell catalyst layers are a complex topic, having been the subject of ever-expanding study for several decades. The commonly found, industrial-standard fuel cell catalyst layers are comprised of a supported electrocatalyst and ionomer in the catalyst layer, an active 'electrode binder.' The electrocatalyst and electrocatalyst support are large fields of study in their own right. This thesis will focus on ionomer in the catalyst layer, specifically the long-desired transition from perfluorinated ionomer catalyst layers high-performing, long-lived hydrocarbon ionomer systems and the effects of interfacial tuning that may be especially relevant to the adoption of hydrocarbon systems.

To be able to properly contextualize the effects that the choice of ionomer, catalyst ink, catalyst layer composition, and catalyst layer deposition effect in the operation of a fuel cell requires several aspects of the system to be understood. The first and most important is the structure-property relationships of the polymer both in bulk and as thin film with respect to microstructure, charge carrier conductivity, and gas and liquid permeabilities. The second is the microstructure of the resulting catalyst layer, heavily dependent upon both ionomer choice, catalyst ink composition, method of catalyst deposition, the method of membrane-electrode assembly preparation, and the method of fuel cell construction. Several interfaces must also be considered, in particular those between the catalyst layers and membrane, between the catalyst layers and microporous layers. Even with the majority of choices fixed to those of a standard system optimized for perfluorinated materials, the parameter space is incredibly large. Operational choices – cell temperature, relative humidity, reactant gases, and gas pressures, only add to this parameter space. As a result, elucidating fundamental properties about ionomer in the catalyst layer, the object of this thesis, requires an understanding of this broader context, comprising Chapter 1. Understanding and tuning catalyst layer microstructure through catalyst ink composition in hydrocarbon systems in proton-exchange membrane fuel cells comprises Chapter 2. Accomplishing the same understanding and tuning of catalyst layer microstructure in anion-exchange membrane fuel cells through the lens of deposition methodology is the object of Chapter 3. A new method of creating membrane-electrode assemblies and the impact on both catalyst layer interfaces is the object of Chapter 4.

Chapter 1. Introduction

1.1. Low Temperature Fuel Cells

Fossil fuels are a finite resource, and renewable electricity generation alone cannot meet all the energy transformation needs presently served by fossil fuels, nor can electrical grids meet the energy transmission requirements. Hydrogen provides a stable basis for a renewable energy economy that can be scaled to meet global requirements. Through electrolysis, hydrogen can be formed by established methods in quantity. Paired to renewable sources of electricity, this production is entirely renewable,[1] and the only single source of portable energy capable of addressing the non-electrical portion of the 'Terawatt Challenge' of up to 30 TW_{avg} for 100% renewable energy by 2050.[2]

While hydrogen can be burned in combustion engines, effectively taking the place of natural gas, it may be employed far more efficiently in hydrogen fuel cells. Proton-exchange and anion-exchange membrane fuel cells comprise low-temperature polymer electrolyte fuel cells, and are the best renewable energy generation candidates for applications where rapid start-up, instantaneous alterations in load, fast re-fueling, long-range fuel storage, low capital cost, and/or operation in highly variable environments are necessitated, e.g. consumer automobiles,[1] unmanned aircraft,[3] heavy transport,[4] industrial machines, or small-scale electrical generation. As a result, substantial research by electrochemists has been performed on low temperature fuel cells since their development for the Gemini space programme of the 1960's to develop clean power generation suitable for mass adoption in both mobile and stationary applications.[5]

1.1.1. Categories of Fuel Cells

A fuel cell is an electrochemical device for the direct, continuous, high efficiency conversion of chemical energy into electrical energy, with reaction overpotential being converted into potentially useful heat, with combined heat and power system total efficiencies reported to 90% and above.[6–8] Fuel cells accomplish this conversion by separating a redox process into two separate half-reactions that require the transport of electrons through an external load, made possible by catalyzing the half-reactions in conductive media connected to current collectors and employing an ion-conducting but reactant-impermeable & electronically insulating material between the two active catalyst layers.[9,10] The first fuel cell was created by Sir William R. Grove in 1838 using hydrogen, oxygen, Pt electrodes, and sulfuric acid electrolyte. Significant theoretical contributions were made by Christian Schönbein at that time and Friedrich W. Ostwald in 1893.[11]

Alkaline fuel cells, AFCs, were used early in the Apollo space programme to generate electricity, employing an alkaline liquid electrolyte; fouling of the catalyst layer limited their utility.[12] Phosphoric acid fuel cells (PAFCs) were similarly constructed using an acidic liquid electrolyte, but the very high precious metal catalyst loadings required and resultant high lifetime cost limited their economic viability, and while commercial these form a small (~7%) and decreasing part of the present fuel cell market.[13]

Classes of fuel cells being developed today may be broadly classified as high-temperature or low-temperature fuel cells. High-temperature fuel cells employ ceramics, with molten carbonate fuel cells (MCFCs) using a porous polymer matrix with molten carbonate electrolyte and solid oxide fuel cells (SOFCs) using a non-porous ceramic as the electrolyte.[14] High-temperature fuel cells may directly employ reformate as fuel, or even gaseous hydrocarbons, which crack to hydrogen gas under operational temperatures, in excess of 650 °C. These are most suited to large stationary power generation, where high efficiency and low CO sensitivity are prized, and where very slow start-ups are tolerable. As above, low-temperature polymer electrolyte fuel cells are more suited to mobile or smaller stationary power generation. The two broad classifications of low-temperature polymer electrolyte fuel cells are acidic proton-exchange membrane fuel cells (PEMFCs) and the recently developed alkaline anion-exchange fuel cells (hereafter AEMFCs, also known as AMFCs, AAEMFCs, or hydroxide-exchange membrane fuel cells, HEMFCs). The most common and promising application of these catalyzes the hydrogen/oxygen redox couple, with the resultant fuel cells named PEMFCs and AEMFCs. The first commercial fuel cell car, the Toyota MIRAI, is based on PEMFC technology.[15] Other types of low-temperature fuel cells also employ PEM and/or AEM membranes but are named for the reductant, for instance direct methanol fuel cells (DMFCs) or direct ethanol fuel cells (DEFCs), by function in the case of microbial fuel cells (MFCs) or biofuel cells (BFCs),[16–18] or by the distinguishing feature with bipolar membrane fuel cells, BPMFCs.[19,20] Within low-temperature fuel cells based on soft materials, comparatively higher-temperature systems are also being investigated. The most common class of these adapt aspects of PAFCs into systems based on phosphoric acid doped polybenzimidazole (PBI) membranes as high temperature proton-exchange membrane fuel cells (HT-PEMFCs).[21]

1.1.2. Electrochemistry of Low-Temperature Fuel Cells

A research-scale PEMFC stack is illustrated in Figure 1.1. Humidified reactant gases, typically hydrogen from a compressed tank and oxygen as external air, are fed through patterned flow fields, gas-diffusion layers, microporous layers, and finally into the electrodes (described further *vide infra*, section 1.3). These layers serve multiple purposes, being conductive to help deliver electrons with low resistance, being porous to equalize reactivity across the anode or cathode, and being hydrophobic to assist in clearing the substantial volume of water produced by the operating fuel cell.[22,23]

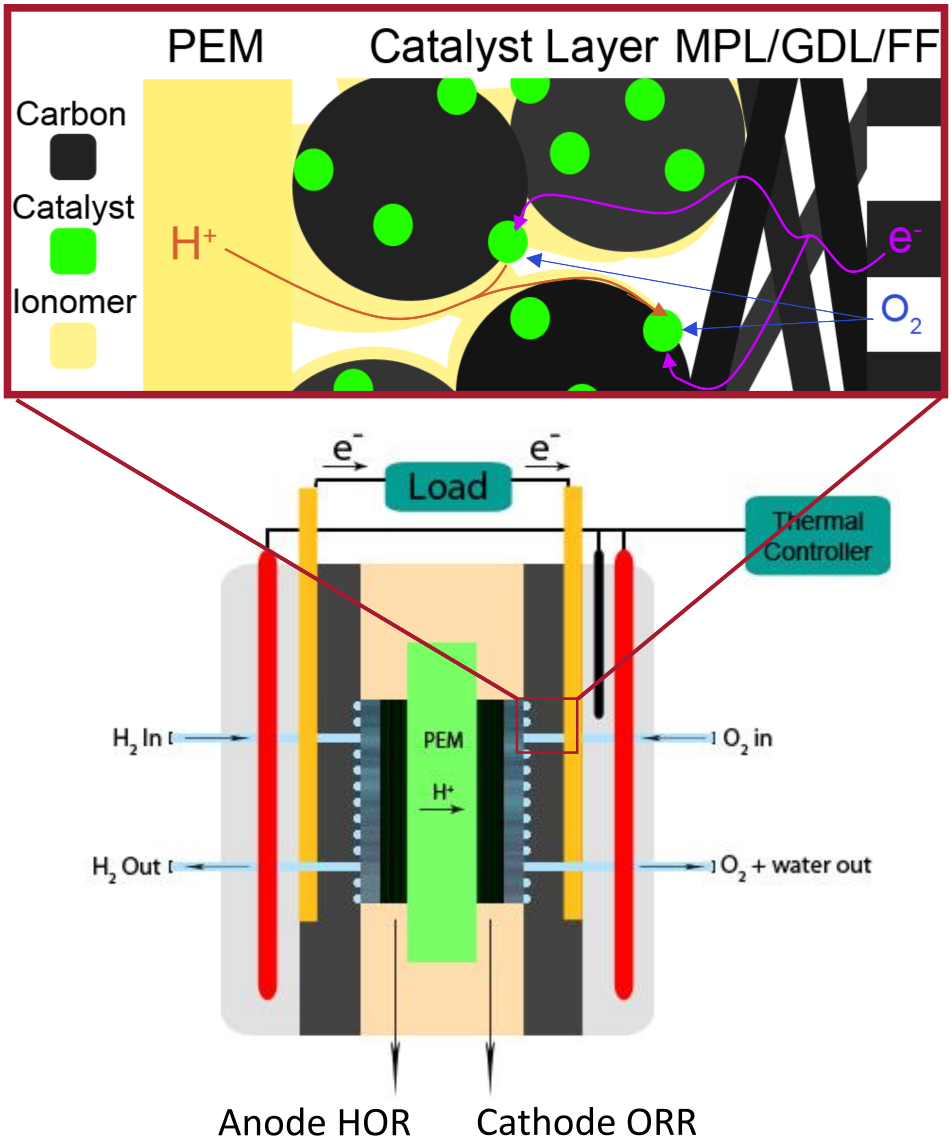

Figure 1.1: **Schematic of a research-scale proton-exchange membrane fuel cell hardware with MEA in operation; from centre outwards, components are membrane, catalyst layer, microporousl layer, gas-diffusion later, flow field, current pickup, and heat-controlled fuel cell hardware; reactions at the cathode and anode as shown in equations 1.1 and 1.2, respectively, for an overall reaction as in equation 1.5.**

The operation of PEMFCs is governed by two half reactions, the oxygen reduction reaction (ORR) and hydrogen oxidation reaction (HOR). For acidic media, reaction equations are written in equations 1.1 & 1.2. All oxidation or reduction potentials hereafter are reported relative to the standard hydrogen electrode (SHE).

$$O_{2(g)} + 4\ H^{+}_{(aq)} + 4\ e^{-} \rightarrow 2\ H_2O_{(l)} \qquad E^{\circ} = +1.229\ V \tag{1.1}$$

$$2\ H_{2(g)} \rightarrow 4\ H^{+}_{(aq)} + 4\ e^{-} \qquad E^{\circ} = +0.000\ V \tag{1.2}$$

A research-scale AEMFC is illustrated in Figure 1.2, and the reactions equations for the ORR and HOR are provided in equations 1.3 & 1.4.

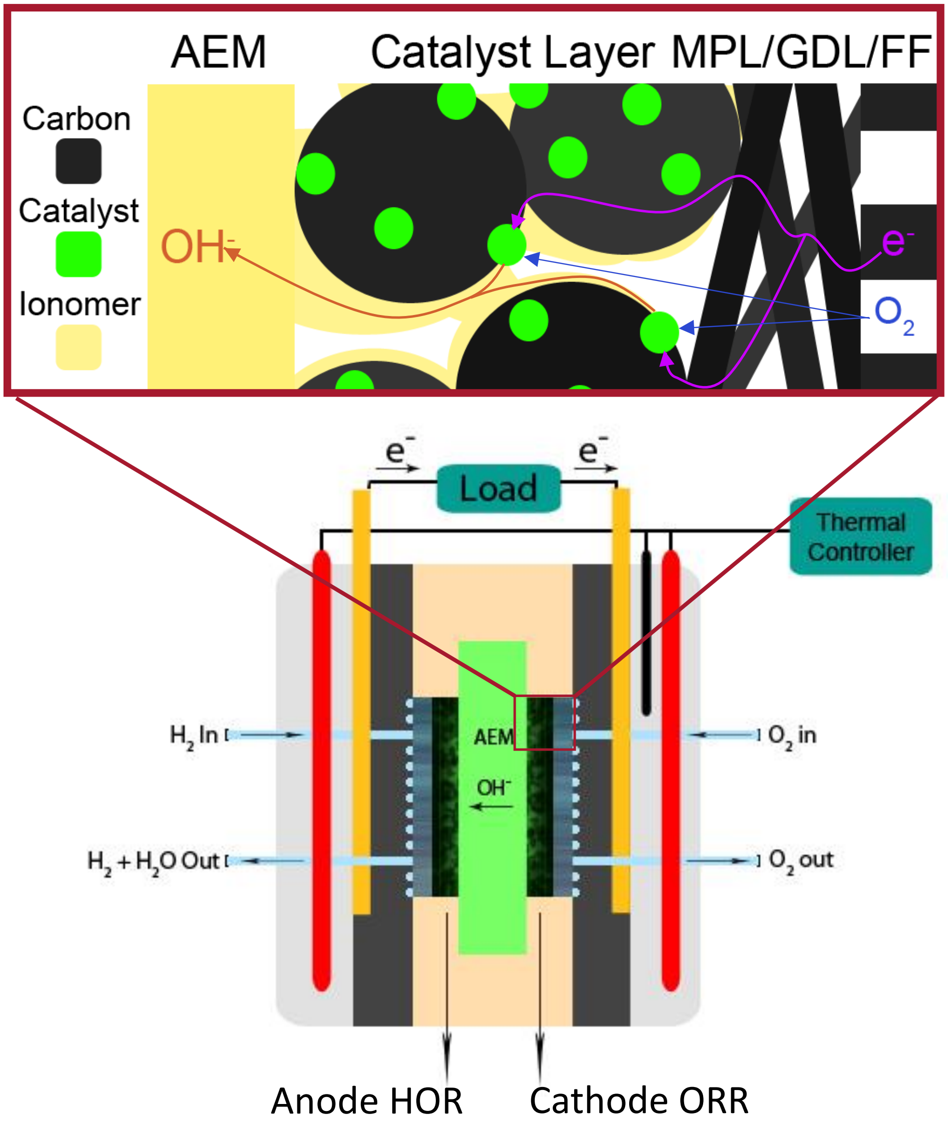

Figure 1.2: **Schematic of a research-scale anion-exchange membrane fuel cell hardware with MEA in operation; constituents as described in figure 1.1; reactions at the cathode and anode as shown in equations 1.3 and 1.4, respectively, for an overall reaction as in equation 1.5.**

$$O_{2(g)} + 2\ H_2O_{(aq)} + 4\ e^- \rightarrow 4\ OH^-_{(aq)} \qquad E^\circ = +0.828\,V \qquad \textbf{1.3}$$

$$2\ H_{2(g)} + 4\ OH^-_{(aq)} \rightarrow 4\ H_2O_{(l)} + 4\ e^- \qquad E^\circ = +0.401\,V \qquad \textbf{1.4}$$

Combining equations **1.1** and **1.2** or **1.3** and **1.4**, the same overall cell reaction and potential of +1.229 V, for the H_2/O_2 redox couple is obtained. The cell potential shown below corresponds to STP conditions and liquid water as the product. If the reaction product is water vapour, the cell potential at equilibrium is +1.18 V.

$$2\ H_{2(g)} + O_{2(g)} \rightarrow 2\ H_2O_{(l)} \qquad E_c^\circ = +1.229\,V \qquad \textbf{1.5}$$

The Gibbs Free Energy in standard state, ΔG°, for this process is -474 kJ. ΔG may be written for arbitrary conditions as

$$\Delta G = \Delta G^\circ + RT\ln(Q), \qquad \textbf{1.6}$$

where R, 8.3145101 $J\cdot mol^{-1}\cdot K^{-1}$, is the ideal gas law constant, , T is temperature (K), and Q is the reaction quotient.

ΔG is connected to the theoretical reversible cell potential by

$$\Delta G = -nFE_c, \qquad \textbf{1.7}$$

where F is the Faraday constant, 96485 $C\cdot mol^{-1}$ and n is the number of electrons transferred in the process; here, n=4 for the Pt-catalyzed reaction. Combining equations **1.6** and **1.7** results in the Nernst equation, equation **1.8**, which describes theoretical reversible cell potential for any conditions,

$$E_c = E_c^\circ + \frac{RT}{nF}\ln\left(\frac{p_{H_2}{}^2\cdot p_{O_2}}{p_{H_2O}}\right), \qquad \textbf{1.8}$$

where p_{O_2} and p_{O_2} represent the partial pressures of reactant gases and p_{H_2O} represents the partial pressure of water if produced in vapour form, or if the reaction product is liquid water, the activity of water, $a_{H_2O} \approx 1$, must be used instead of the partial pressure. Notably, the theoretical reversible cell potential drops to +1.18 V when water vapour is considered the product instead of liquid water. The practical operational window of present-day low-temperature fuel cells (0-120 °C, 0.209-3 atm O_2, 1-3 atm H_2) results in less than a ±0.01 V alteration to this theoretical cell potential (see Appendix A). Higher temperatures significantly improve reaction kinetics and increase the conductivities of membrane and ionomer in the catalyst layer (hereafter 'ionomer'). In addition, higher temperatures diminish the negative effects of CO poisoning of the catalyst layer in acidic media. Stability at higher temperatures is accordingly a goal of both PEM and AEM development.[24]

Despite equivalent overall reactions (Eqn. 1.5), reactant ion flows occur in opposite directions between acidic and alkaline cells. In acidic media, protons are transported from anode to cathode, and water is a product at the cathode. The anode catalyst layer and anode side of the membrane may dehydrate due to electroosmotic drag. In alkaline media, water is a reactant at the cathode, hydroxide ions are transported cathode to anode, and water is product at the anode. Dehydration occurs at the cathode from both electroosmotic drag and use in the ORR. Water is produced at the anode, double the water at a given current density. These significant differences in ion and water transport engender different considerations for every component of the fuel cell and its characterization.[25–28]

1.1.3. Membrane electrode assembly (MEAs)

A membrane electrode assembly (MEA) refers to the ion-conducting functional polymer membrane ('membrane' hereafter) and the two catalyst layers on either side of the membrane that become cathode and anode of the resultant electrochemical device (Fig. 1.3). Together, these form a catalyst-coated membrane (CCM), also known as a '3-layer MEA.' The addition of gas-diffusion layers is called a '5-layer MEA' and this forms the core of a fuel cell stack. The large majority of efficiency losses occur within this MEA, particularly the catalyst layers, and as a result the determination of structure-property relationships of materials incorporated into these layers has been a major focus of the field for many years. To form an MEA, catalyst ink is transformed into catalyst layers by a deposition process whereby the solvent is driven off and solids thereby deposited. This catalyst layer may be deposited on the membrane, microporous layer (MPL) of the gas-diffusion layer (GDL), or on an inert substrate (e.g. PTFE) to create free-standing catalyst layers transferred into the system by the 'decal transfer method.'

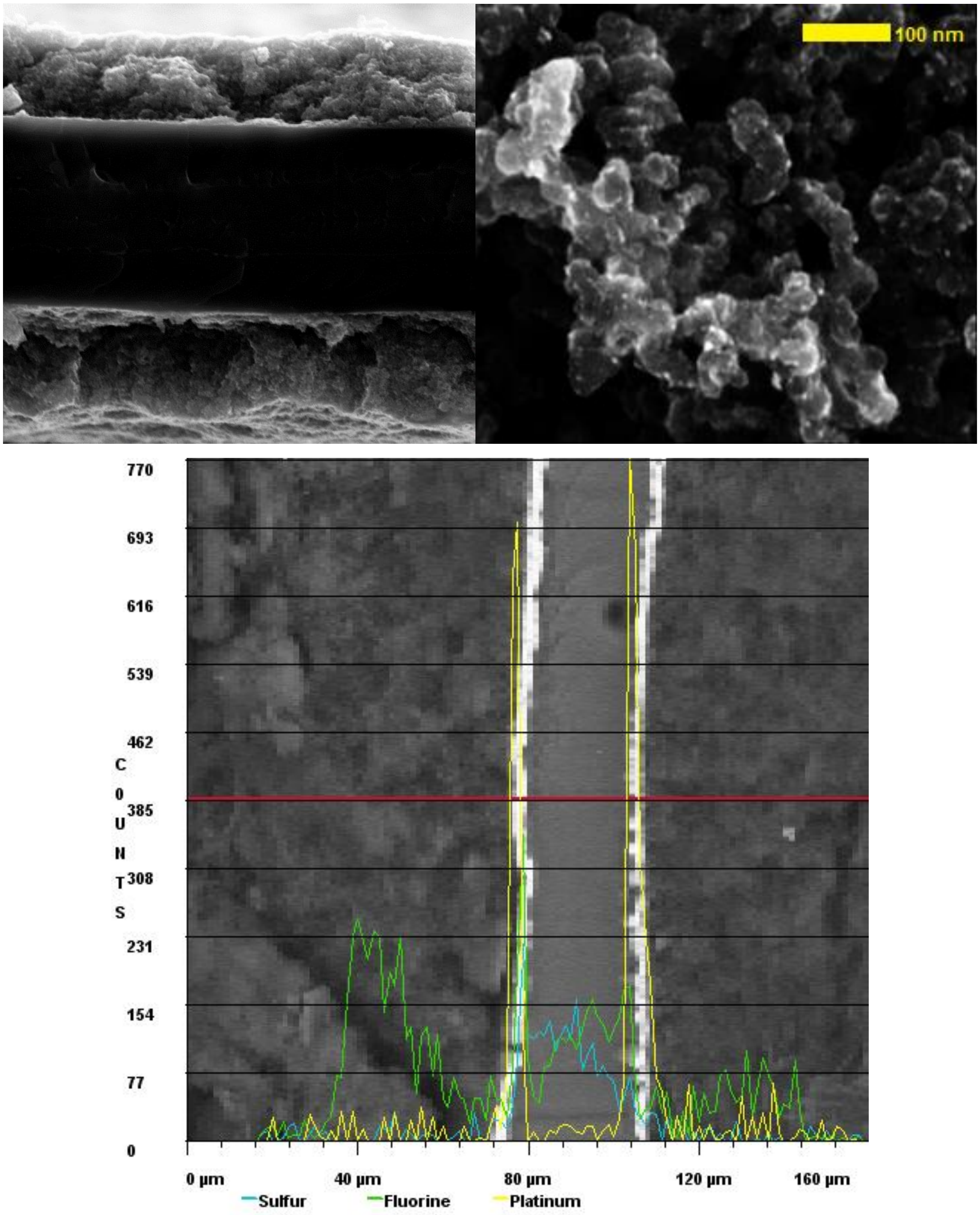

Figure 1.3: **Scanning electron microscopy (SEM) images of A) a catalyst-coated membrane (CCM), AKA 3-layer MEA; B) close zoom on catalyst layer, noting clusters of ionomer-bound carbon particles decorated with platinum nanoparticles; and B) CCM with gas-diffusion layers (GDLs), AKA 5-layer MEA, with energy-dispersive x-ray (EDX) signal overlay confirming Pt-containing electrodes, PFSA membrane, and PTFE-treated GDLs.**

1.2. Membranes

1.2.1. Proton-Exchange Membranes (PEMs)

Perfluorinated sulfonic acids (PFSAs) comprise the current standard for PEMs and ionomer. PFSAs were developed in the 1960s, with DuPont's Nafion® becoming the archetypal proton-exchange membrane (Fig. 1.4a). In the early 2000's, environmental concerns related to the emission of perfluorooctanoic acid (PFOA) and prefluorooctanesulfonic acid (PFOS) after PEMFC end-of-life inspired a greater focus within academia and industry on shorter side-chain PFSAs such as Solvay's Aquivion® (Fig. 1.4b) or 3M's 3Mion® (Fig. 1.4c).[29] PFSAs generally combine high conductivities, chemical stability, physical stability, and processability as ionomer solution in a fully low-boiling solvent mix, making them well-suited to fuel cell use.

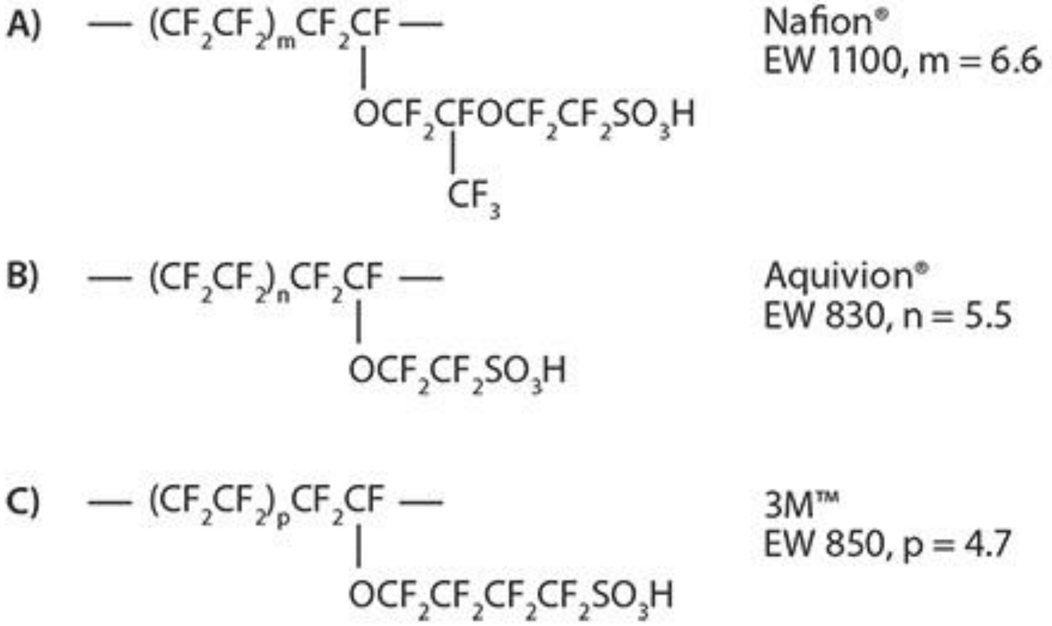

Figure 1.4: Chemical structures for common variants of commercial PFSA membrane/ionomer materials A) Nafion, B) Aquivion, and C) 3Mion; varying equivalent weights (EWs) are achieved by varying the repeating main chain unit (i.e. the values of m,n, or p for the PFSAs shown); see also Appendix B.

High conductivities require a high number of functional units per unit volume for greater proton mobility and the formation of water channels with low tortuousity, i.e.

straight channels formed in the through-plane direction, wide enough to minimize dead-ends within these channels without causing excessive swelling or solubility.[30,31] These materials properties are best realized by good hydrophobic-hydrophilic phase segregation, where hydrophilic groups can rearrange into hydrophilic domains and absorb water to form water channels, while hydrophobic domains counteract swelling and maintain the structural integrity of the material. Examining the structure-property relationships of phase segregation by different chemical strategies has been the focus of significant research that guides materials discovery efforts (see also 1.2.1 & 1.2.2).[32,33]

Insights into structure-property relationships for ion-exchange membranes are found by a number of *ex situ* tests typically performed on new materials. Electrochemical impedance spectroscopy measures in-plane conductivity, determined from the high- and low-frequency intercepts on the Nyquist plot (see 2.2.6).[34] Water uptake is determined by gravimetric methods, while liquid-liquid, liquid-vapour, vapour-vapour, and electro-osmotic transport properties are determined either by physical or electrochemical methods.[35–37] Dimensional swelling, expansion of membranes caused by water uptake into the hydrophilic domains of the polymer, is typically reported as linear expansion in the xy-dimensions and separately as linear expansion in the z-dimension. Dimensional swelling is found by measurement of a material dry and after equilibration in an environmental chamber under relevant conditions (e.g. 80 °C, 100% RH). Similar water adsorption-desorption experiments have been performed on ionomer in the catalyst layer to differentiate properties of ultra thin films, and important and increasingly more common consideration.[38] Ion-exchange capacity (IEC) is a measure of the number of functional ion-exchange groups per unit mass ($meq \cdot g^{-1}$), e.g. the number of sulfonic acids per 1000 g polymeric weight. IEC is measured both by NMR, the theoretical IEC, and titration, the IEC accessible to water.

The IEC is the factor determining various properties including water uptake and dimensional swelling. These properties impact conductivity and mechanical strength. Ion-exchange membranes and ionomer materials are typically classified by their IEC. The IEC of Nafion lies in the range of 0.9-1.0 $meq \cdot g^{-1}$, the upper limit dictated by its water solubility in relevant operational conditions. Aquivion (Fig. 1.3b), representative of shorter side-chain polymers, achieves an IEC of 1.2 (see also Appendix B). At 80 °C, 100% RH by *ex situ* in-plane electrochemical measurement, Nafion achieves a conductivity of 110 mS/cm and Aquivion 230 mS/cm , both with less than 50 wt% water uptake. These examples effectively provide the practical limits of conductivities and water transports relevant to application in PEMFC membranes and ionomer, although some of the producers of PFSA ionomers such as 3M supply materials for research using higher IEC materials.[39]

While membrane conductivities are generally reported as constant for a given equivalent weight, the measurement theoretically normalized for membrane thickness, the skin of PFSAs is more resistive than the bulk in membranes when the membrane is equilibrated to water vapour, even at 100% RH. This results in membrane conductivity dropping significantly as thin membranes are employed. As with other physical properties of membranes, skin effects are not simply innate to a given polymer formula and molecular weight, but also a function of the conditions used in processing this polymer into a membrane such as solvent, annealing temperature and time, as well as subsequent integration, such as lamination. As a result, substantial research has been directed at understanding skin effects and improving interface design to minimize the impact on transport properties.[40]

The morphology and film thickness of ion-exchange materials are significant consideration for both the membrane and ionomer in the catalyst layer. From the 1980's to the 2000's, the commercial baseline for membranes in PEMFCs transitioned from extruded 175 µm Nafion 117 to dispersion-cast 25 µm Nafion 211, and more recently to 5-20 µm ePTFE-reinforced membranes. Thinner membranes have several benefits including allowing for higher total conductance and high back-diffusion of water.[15] and the alteration of membrane production process reduced the PFSA skin effect.[41] This is further complicated in short side-chain membranes which require hot-pressing to induce crystallinity by enhancing molecular ordering in the annealing process. This is effective in preventing over-swelling of the membrane and dissolution of ionomer in the catalyst layer despite the higher IECs of these materials.

Ionomer in the catalyst layer forms films sub 20 µm, necessitating separate research into ionomer properties as extremely thin films. Only probing the effects of volume confinement, surface interactions, and skin effects at the correct scale can elucidate what materials properties are important for ionomer and how these may differ from the requirements of membranes (see 1.2.3 & 1.2.4).

Chemical stability is a blanket term for the stability of membrane/ionomer in acid, to oxidative conditions, to hydrolysis, and to radical attack. Acid stability is not an issue below thermal decomposition limits. While the oxidative stability of PFSAs was vital to the adoption of PFSA membranes in several major applications – e.g. electrolytic and electrodialysis cells for water treatment, PEM electrolyzers, and chlor-alkali systems – potentials remain below 1.23 V in fuel cells and oxygen is the only oxidant in the system, so development of oxidative stability is not a major concern beyond the low threshold of stability under pressurized air. Hydrolysis is not of concern in PFSA, although the hydrolysis of persulfate precursors leads to -COOH end groups that in turn accelerate PFSA degradation by radical attack. The stability of PFSA membrane and ionomer to degradation by radical attack is a major determinant of fuel cell lifetimes. Radicals form when 2 e^- ORR occurs; while this is typically prevented on Pt, direct reaction of O_2 and H_2 at the cathode caused by fuel crossover provides the major source of radical density in an operating fuel cell (see 2.2.3). Oxidized impurities in precursors cause carboxylic acid end-groups in PFSAs, providing a facile pathway for PFSA degradation according to the following mechanisms:

$$\text{R-CF}_2\text{COOH} + \text{OH}^{\cdot} \rightarrow \text{R-CF}_2^{\cdot} + \text{CO}_2 + \text{H}_2\text{O} \qquad \mathbf{1.9}$$

$$\text{R-CF}_2^{\cdot} + \text{OH}^{\cdot} \rightarrow \text{R-CF}_2\text{OH} \rightarrow \text{R-COF} + \text{HF} \qquad \mathbf{1.10}$$

$$\text{R-CF}_2^{\cdot} + \text{H}_2\text{O} \rightarrow \text{RF-COOH} + \text{HF} \qquad \mathbf{1.11}$$

A major breakthrough in the realization of target fuel cell lifetimes was the post-functionalization of these carboxylic acid end groups in PFSAs, conclusively demonstrating that targeting degradative pathways can be effective in significantly reducing radical degradation in fuel cells. However, solid-state NMR work indicates side chains are still susceptible to radical attack. It has also been suggested that main chain scission results from radical attack by $H\cdot$. As HF results after recombination in all of these pathways, the fluoride emission rate is considered an accurate measure of membrane/ionomer degradation in operating fuel cells. In *ex situ* studies, both loss of polymer molecular weight as well as titratable and/or NMR-derived IEC are also considered as indicative of degradation, representing loss of mechanical strength and functionality, respectively. As the ionomer constitutes a small fraction of the total polymer electrolyte in the system, the majority of polymeric degradation is thought to occur in the membrane, i.e. if the fluorine emission rate was predominantly attributable to degradation of the ionomer, none would remain within a short period of time. Chemical degradation in PFSA-based membranes leads to pinhole formation, as the formation of reactive end-groups lead to increased local rates of degradation further exacerbated by increased fuel crossover at these sites. .

Redesigning and synthesizing PFSAs to achieve enhanced properties is extremely challenging (see 1.2.4), so the focus in the field has shifted to the reduction of radical density in the fuel cell. Rigorous elimination of iron, copper, and other Fenton-active metals reduces radical density, and was another key breakthrough in increasing fuel cell lifetimes. To further reduce radical densities, both organic and inorganic additives are being explored as radical scrubbers in PEMs, with CeO_2 presently the most prevalent additive. Barrier layers may reduce crossover without substantially affecting membrane conductivity, and may allow greater overall conductance of a membrane by mechanically stabilizing thinner films than may be consistently produced by unstabilized polymer, although thinning membranes increase gas crossover in turn.

The accepted *ex-situ* accelerated stress test (AST) to probe the stability of fuel cell membrane/ionomer to radicals ('chemical stability' hereafter) is the Fenton's Reagent Test ('Fenton test' herafter), wherein a membrane is heated in a solution of hydrogen peroxide and iron salts, with the $Fe^{2+}/^{3+}$ redox couple acting as catalyst for radical generation. Typical conditions include 10 ppm Fe^{2+} and 20 wt% H_2O_2 at 80-85 °C, with the solution replaced at set intervals. In a 48 h test on Nafion, a mass loss in excess of 15 wt% was observed, encompassing both main-chain scission resulting in reduced molecular weights and side-chain scission resulting in lower IEC.[42]

The common *in-situ* AST for chemical stability involves operation at increased temperature, low relative humidity (RH), and open-circuit voltage (OCV). High potentials cause a continuous production of $OH^{\cdot}$ radicals at a rate significantly higher than in normal fuel cell operation. These radicals are generated by the same means and in the same locations as in an operating cell. As a result, *in situ* ASTs better represent the chemical degradation that occurs in fuel cells compared to the Fenton test; however, both techniques must be used, ultimately proving complementary in understanding real phenomena in fuel cells, and neither fully describes real long-run tests such as the positive effect of Pt-banding.[43,44]

Mechanical stability is also a requirement for fuel cell membranes, with elasticity (high strain) being favoured over strength (high stress). Beyond the fundamental polymer chemistry, casting solvents and conditions determine mechanical toughness of membranes by dictating the gelation process of the membrane, with a homogeneous gelation being preferable to an inhomogeneous precipitation. PFSAs such as Nafion are known to exhibit hysteresis to an extreme depending on the conditions of film formation: tensile toughness, the area under the stress-strain curve, was shown to vary over 100x depending on solvent and conditions of solution-deposited films, independent of observed crystallinity.[45]

Mechanical degradation interacts with chemical degradation, as radical degradation rapidly leads to the loss of polymeric plasticity and ultimately to mechanical failure,[46] while the formation of thin spots due to mechanical strain may in turn enhance chemical degradation. Strong but brittle membranes are unsuitable for use in fuel cells, as they easily form cracks when compressed into fuel cells or when subjected to RH variations, increasing gas crossover and the resultant *in situ* radical densities substantially, causing a cascade of degradation.

Several mechanisms exist to counteract mechanical degradation of membranes. Membranes can be cross-linked to itself and/or to a reinforcing web for added mechanical toughness of the material. The use of soft gasketing materials can minimize strain on the membrane, greatly increasing lifetimes of materials under humidity cycling.[47] Edge reinforcement can significantly counteract failure along the stress point at the membrane-gasket boundary. Operational conditions may also be chosen to limit physical stress on the membrane, for instance by maintaining a consistent, high humidity including during startup/shutdown cycles.

As chemical and physical stability cannot provide an adequate measure of material lifetime in isolation, developmental work on ASTs seeks to combine both modes of degradation. Generally accepted practice for the reporting of AST data on new materials, additives, or reinforcements requires an internal standard using an unreinforced PFSA of similar membrane thickness (see 2.2.3).

1.2.2. Effect of PEM Properties on Fuel Cell Operation

Beyond considerations of hydrogen crossover and overall fuel cell lifetime, thin, reinforced membranes are preferential for fuel cell operation due to their low resistance, low swelling, and high hydraulic permeation rate.

Membrane and catalyst layer resistances together account for the majority of the efficiency losses in an operating fuel cell.[48] Proton conductivity through the membrane accounts for the losses in the Ohmic region of the polarization curve, and increasing membrane conductivity for a given membrane thickness increases efficiency at a given current density for practical power densities in a working fuel cell, particularly under backpressure (see 2.2.1).

Water content is the second most-considered parameter of a fuel cell membrane. Although interrelated to conductivity – water uptake and the resultant dimensional swelling is necessary for materials to achieve high conductivities – swelling itself reduces the effective proton concentration in a given proton-conducting channel, and thicker membranes exhibit a lower total conductance, however both of these impacts are generally minimal and only notable in the case of materials that can achieve very high water contents such as sPEEK possessing high ion exchange capacities.

More importantly, dimensional swelling causes problems during fuel cell operation. Swelling in the xy direction has long been known to cause problems interfacial and mechanical strain (shear) along the edges of a fuel cell.[49] Swelling in the z direction may cause the catalyst layers to compress and thereby cause water transport issues or may cause membrane material to be intercalated into the catalyst layer, reducing the electrochemically active surface area. However, these effects may be remediated with low initial stack compression or modifiable compression, and the impact further depends on the compressibility of the GDL and the thickness of the catalyst layer. Optimizing operational parameters such as relative humidity, temperature, and backpressure may also be accomplished to counteract swelling in the z direction or problems related to it.[50] As a result, swelling in the xy direction is considered the greater problem and commercial membranes are reinforced with an inactive mesh, typically ePTFE, to direct swelling in the z-direction in addition to adding mechanical stability.

Also related to the conductivity to swelling ratio of membranes, channel connectivity and tortuosity are important parameters of a membrane to consider. Significant insight can be gained *ex situ* – the water uptake can be readily measured in the wet form, while membrane conductivity can be measured in-plane or through-plane 3- or 4-probe EIS. The effectiveness of nanophase segregation and the channel diameters achieved can be investigated by exchanging protons for silver or lead ions and conducting transmission-electron microscopy (TEM) on membranes. Recent work has paired this with a new method of X-ray analysis to separate 'useful' water content engaged in proton conduction from 'useless' water content isolated from conductive pathways.[51] This is promising to identify structures that maximize conductivity through enhancing the proportion of 'useful' water content while minimizing the loss of mechanical strength to the proportion of 'useless' water content.

Conductivity ($mS \cdot cm^{-1}$) is the parameter reported to compare membranes, as the normalization to thickness allows for a single value to describe a given ion-exchange material to a small margin of error despite the wide variety of membrane thicknesses used in applications. However, conductance (mS) is the important term to operational efficiency, resulting in thinner membranes being more efficient to employ in fuel cells. While skin effects caused by crystalline, highly tortuous regions near the surface reduce conductivities as thickness decreases – particularly in PFSAs, under reduced humidities, and in extruded membranes – the overall conductance increases as membranes are made thinner.

Besides conductance, hydraulic permeation is a less commonly considered parameter important to the understanding of membranes *in situ*, as this determines the rate of water permeation through a membrane. An excess of water is produced at the cathode alongside water molecules being transported to that side via electro-osmotic drag, so permeation of this water is necessary to rehydrate the anode side and achieve maximal conductivity, commonly and hereafter called back-diffusion as this occurs in the opposite direction to electro-osmotic drag.

Early commercial fuel cells for light transport such as the Toyota Mirai do not employ external humidifiers in order to reduce stack cost, and rely on reinforced ultra-thin membranes such as GORE-SELECT®. The 5 µm, 0.9 meq·g^{-1} IEC membrane has a reported conductivity of merely 28 mS·cm^{-1}, compared to 100 mS·cm^{-1} for the 60 µm, identical IEC N112, the standard value reported for PFSAs. However, this GORE-SELECT membrane exhibits a 3.3x increase in conductance. Similarly, hydraulic permeances were found to increase with reduced thickness and particularly with increased IEC and the resultant increased water uptake.[49] The net effect of ultra-thin membranes are a significantly faster water equilibration and a greater maximum rate of water transport. These are both vital properties for automotive fuel cells operating at high current densities and with reduced or absent external humidification, counteracting both cathode flooding and anode dehydration from electro-osmotic drag.

1.2.3. Ionomer in the catalyst layer

Incorporating ionomer into a catalyst layer improves the ionic conductivity of the catalyst layer, simultaneously filling nanopores and the smaller mesopores in addition to effecting a small reduction in the total volume of a beginning-of-life (BOL) catalyst layer. Overall, ionic conductivities of catalyst layers are around two orders of magnitude lower in thin ionomer films than in bulk membrane, and generally over an order of magnitude loss even when the ionomer content in the catalyst layer is normalized to bulk ionomer, e.g. 100% rather than 30% of solids; for illustrations of all these points see Chapters 3 & 4 *vide infra*.[52–54]

Processability of a polymer electrolyte as an ionomer refers to the ability of a polymer to be dispersed in low-boiling solvents. Nafion is the standard ionomer in the catalyst layer. It is provided as a dispersion in alcohol or alcohol-water mixtures, with MeOH and IPA being the two most common alcohols used for this purpose. However, the large majority of hydrocarbon ionomer alternatives are solely soluble in high-boiling solvents (e.g. DMF, DMAc, DMSO), and this has been identified as a major barrier to their adoption by industry. Commercial barriers to the use of high-boiling solvents include long drying times and the necessity of solvent recovery, which complicates manufacturing. While these are surmountable barriers, even small quantities of high-boiling solvents are also known to anneal catalyst layers, reducing their internal pore volume in the mesoporous range. However, counter-claims about the positive effects of glycerol, a high-boiling solvent, on the longevity of catalyst layers warrants further investigation, particularly with respect to hydrocarbon ionomer in the catalyst layer (see section 3.5).

1.2.4. Limitations of PFSAs as Membrane/Ionomer

PFSAs are the standard material for PEMFCs; their initial development enabled the field to begin and their adaptation has led to long-lived and efficient fuel cells. However, replacement of PFSAs with fully hydrocarbon alternatives has been a goal of the field since the 1980's, because PFSAs have many innate, insurmountable drawbacks in terms of their development, production, use, and end of life.

Research into new perfluorinated ion-exchange membranes is slow and beset by many chemical and environmental challenges. Precursors are dangerous and innately expensive, and the presence of fluorine introduces substantial complications in terms of reactivity compared to hydrocarbon chemistry. The use of perfluorinated solvents in the production increases the already high energy requirements for the production of these materials. While waste emission has been significantly reduced due to regulation, fluorine-containing waste and the emission of fluoride/hydrofluoric acid and other breakdown products from fuel cell stacks during and after use – especially perfluorooctanoic acid (PFOA), perfluorooctane sulfonic acid (PFOS), and their equally harmful short-chain analogues – are of considerable environmental concern. These compounds are highly toxic and bioaccumulative, as well as challenging to remove using common wastewater treatment systems – today, 15 million Americans drink water above the EPA limit for PFAs of 70 parts per trillion.[55] Finally, fluorinated ionomer adds cost and difficulty to the recycling of precious metal electrocatalyst from used fuel cells; >95% Pt recovery is possible, but results in large quantities of high-GHG, ozone-depleting exhaust or liquid perfluorinated waste. This issue is of significant concern to the mass adoption of fuel cells, given both finite platinum production and strong commitments to reduce PFSA use wherever possible.[29]

Additionally, achieving consistent quality control for polymer production, casting, and integration into catalyst layers has proven extremely difficult. This has only been achieved by large companies after many years of development work. Altogether, research into new PFSAs is pursued by a handful of industry labs globally. Collectively, base material costs, high energy requirements, and difficulties in processing at every step result in perfluorinated sulfonic acids being substantially greater in cost than a comparable hydrocarbon material at any given scale, and while the DOE's cost targets of <\$150/m^2 can readily be achieved by thin PFSAs at volume, only fluorine-free membranes will ever be able to achieve the target of \$25/m^2 for global supply.

Several materials properties of PFSAs do not align with those desired for fuel cell membranes. First, increasing operating temperatures to 120 °C or greater is a goal of the field. Higher temperatures improve reaction kinetics, simplify water management, and mitigate CO catalyst poisoning. The latter point is especially important. Reformate (hydrogen from cracked methane) comprises 95% of the hydrogen gas supply and contains high concentrations of CO as impurities from its production process. Processing this to the required ultra high purity increases its cost significantly, substantially impacting the economics of the nascent hydrogen economy. However, PFSAs are not suitable for fuel cell operation at 120 °C. While the T_g of PFSAs cannot be rigorously defined, long side-chain PFSAs creep substantially above 80 °C, while shorter side-chain PFSAs may increase this threshold by up to 40 °C. Operational temperatures higher than 80 °C coupled with dehydration of the membrane have been strongly implicated in polymeric rearrangement that irreversibly results in lowered conductivities, even in the presence of hydrophilic additives such as TiO_2 or SiO_2.[56–58] Furthermore, RH changes at higher operational temperatures antagonize the effect.[59] Polymeric creep also results in thinning, which increases fuel crossover and thereby decreases membrane lifetime. As a result, 80-90 °C is the *de facto* operational threshold for PFSA-containing MEAs.

Degradation of PFSAs causes a chain of effects within the fuel cell that result in a feedback loop of further degradation ultimately resulting infailure. Hydroxyl radicals have low reactivities within stabilized PFSAs at the beginning of life (BOL). However, degradation causes an increase to the reactivity of PFSAs with the hydroxyl radicals, resulting in failure caused by cracks and pinholes. Among the degradation products of PFSAs are super-acids; for instance, CF_3SO_3H (trifluoromethanesulfonic acid, or triflic acid) has a pKa in water of -12, whereas methansulfonic acid, CH_3SO_3H, has a pKa of -2.6.[60] These products contribute to the significant platinum dissolution at operating potentials >0.6 V as well as likely damage the gas-diffusion layer (GDL).[61,62] A recent ICP-MS experiment detected Pt dissolution at 0.85 V after a mere two hours of operation, with dissolution not limited to either electrode, and exacerbated by high potentials during start-stop operation.[63] Dissolved platinum ions are either washed out of the system or they redeposit within the membrane. Whereas the formation of a full platinum band may increase fuel cell lifetimes by blocking gas crossover,[44] nano-deposits of platinum in the PEM catalyze the creation of hydroxyl radicals and thereby significantly accelerate degradation in the catalyst layer and membrane, particularly on the anode side and in hydrogen-rich regions of the membrane.[64]

1.2.5. Low-Fluorine and Fully Hydrocarbon PEMFCs

Predominantly or fully hydrocarbon chemistry allows for relatively rapid and accessible materials development. A much greater breadth of polymer architectures are more easily accessible; while PFSAs employ side-chain functional groups in pendant- or graft-type polymer architectures as a means of attaining nanophase segregation, other molecular design strategies accomplish the same, including various types of block copolymerization. Hydrocarbons designed for fuel cell use typically have far higher T_gs than PFSAs (i.e. >120 °C, frequently far greater), solving problems related to creep and hot-pressing of PFSA-containing materials in addition to opening up the prospect of efficient, long-lived fuel cell operation at >100 °C.[19,65]

PFSAs and hydrocarbons have significantly different IECs for comparable conducitivities. This is a common barrier to hydrocarbon membranes being understood with respect to their PFSA counterparts. The comparatively heavy fluorine atoms (Z=19 for F vs. Z=1 for H) make the comparison to the functionality of hydrocarbon-based ionomers not straightforward. Nafion at 0.91 $meq \cdot g^{-1}$ IEC (1100 EW) and Aquivion at 1.15 $meq \cdot g^{-1}$ IEC (870 EW) correspond to IECs of 2.71 and 3.40 $meq \cdot g^{-1}$, respectively, if all fluorine atoms are replaced with hydrogens in the IEC calculation (see Appendix B). The comparison is not perfect in terms of functionality of a polymer by volume – Van der Waals radii for carbon, hydrogen, and fluorine are 17, 12, and 15 Å, respectively – but the comparison is substantially more adequate.

If a given family of hydrocarbon materials is of interest, it can be far more readily tuned to a given application, opening up the often called-for but rarely realized possibility of tuning materials properties to the requirements of each distinct location in the fuel cell. In PEMFCs, anode ionomer, anode-side membrane, cathode-side membrane, and cathode ionomer all have different ideal materials requirements. With hydrocarbon materials, it is conceivable that a fuel cell could be created comprising four proton-exchange materials with divergent characteristics to address the needs of these four regions of the fuel cell (e.g. hydrophilicity/hydrophobicity). While many materials candidates contain fluorinated groups, those with the complete absence of fluorination, fully hydrocarbon membranes/ionomer, hold the potential to assist in the mass-adoption of PEMFCs; these allow for highly effective catalyst recovery without the generation of large quantities of liquid fluorinated waste, and the potential for ionomer recycling, and lower to far lower energy input requirements than their fluorine-containing counterparts. Fully hydrocarbon or highly hydrocarbon membranes exhibit significantly lower gas crossovers in addition to reduced OCVs at beginning of life (BOL),[i] both qualities that result in lower radical densities in operating fuel cells, along with a greater versatility for membrane stabilization and other beneficial properties in applications such as DMFCs and MFCs.[66]

---

[i] At an engineering level, low OCVs are considered a positive attribute provided the voltage losses do not extend beyond the kinetic region.

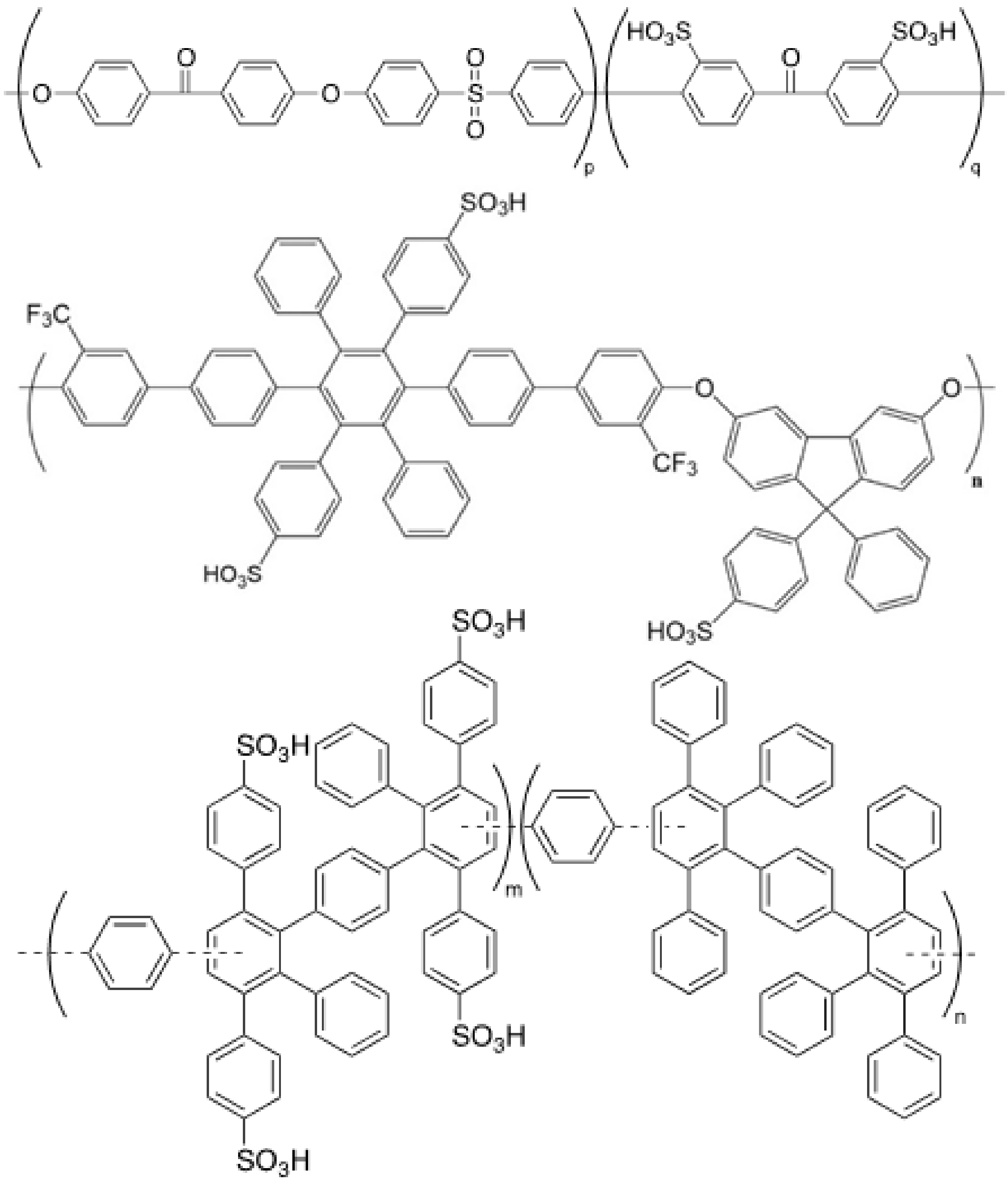

Figure 1.5: **Representative structures of what are herein described as first-, second-, and third-generation hydrocarbon ion-exchange materials designed for fuel cells, namely a.) sulfonated poly(ether ether ketone), sPEEK, a highly linear, low free volume, high ether content polymer represented as a random or block copolymer; b.) sulfonated poly(arylene ether), sP4c (see Chapter 3), containing fewer, electronically protected ether linkages and high free volume; and c.) sulfonated poly(phenylene), sPPP, also represented as a random or block copolymer, comprised entirely of arylene groups, with high free volume, no ether linkages and characterizable, more regular structure due to pre-sulfonation.**

Of the first generation of hydrocarbon materials thought to be able to replace PFSAs, sulfonated poly(ether ether ketone), sPEEK (Fig. 1.5a), was by far the best characterized. Compared to other early hydrocarbon membranes, sPEEK can be prepared with very high IECs before inducing solubility and forms strong, flexible thin films. As a result, sPEEK maintained high proton conductivities at comparatively low relative humidities. However, several issues led to difficulties in its integration into fuel cell systems. At high relative humidities, sPEEK swells excessively. With sPEEK as membrane, excessive swelling both compresses catalyst layers and leads to low durability in start/stop conditions. With sPEEK as ionomer, excessive swelling leads to a lower OCV and greater kinetic losses from electrode poisoning, lower gas permeabilities to active sites due to thicker ionomer coverage of electrocatalyst, and reduced charge carrier concentration, in addition to severe mass transport losses from a reduction in free volume within the catalyst layer. Finally, sPEEK requires dissolution in NMP or other high-boiling solvents, a major barrier to acceptance in commercial systems (see Chapter 3).[11,67–69]

Second-generation hydrocarbons are typified by poly(arylene ether) sulfonic acids; these have T_gs upwards of 180 °C, lower ether contents per repeat unit, and many explorations contain fluorinated units for electronic protection of ether linkages or enhancement of sulfonic acid acidities (see 1.2.4). Unlike sPEEK, these offer promise for lifetimes nearing that of Nafion without major compromises to system efficiencies and the operational window of the system. While mechanical stability is typically far lower than PFSAs and *ex situ* chemical stability tests imply short lifetimes, redesigned systems employing strategies such as soft gaskets and notably even surface cracking have shown potential to extend lifetimes in real conditions beyond the capabilities of PFSAs.[5,70–76]

Third generation hydrocarbons feature the complete elimination of sites most susceptible to chemical attack, in particular ether linkages, from the backbone with a poly(arylene) backbone. As with second-generation materials, explorations have included fluorinated moieties in the backbone or side-chains, or the elimination of fluorination altogether. More advanced systems incorporate structures found to give the desired properties for fuel cell operation in first- and second-generation systems, such as the development of rigid, high internal volume polymer chains and high achievable sulfonation through pre-sulfonation.[77–81]

One substantial difference between perfluorinated and hydrocarbon membranes is the effect of gas permeability. Permeability is considered the product of solubility of a gas in polymer and its diffusivity. Hydrogen permeability results in hydrogen crossover, the majority of gas crossover in a fuel cell, and its reduction is considered to be a significant benefit of hydrocarbon-based membranes. Nitrogen permeability is a lesser source of hydrogen losses in hydrogen-recirculating systems. Oxygen permeability is considered very important to understanding ORR electrocatalysis in a fuel cell and a topic of significant research at present.

1.2.6. Alkaline Anion-Exchange Membranes (AEMs)

Ionomer materials that are stable under alkaline conditions have become significantly of interest to the field since the initial proof-of-concept of alkaline anion-exchange fuel cells (AEMFCs hereafter[ii]) by Fauvarque & coworkers in 2001.[82] In subsequent years, this work was followed by order-of-magnitude increases in membrane conductivity and corresponding current and power densities achievable in AEMFCs.[83] Interest has been further fueled by fundamental research into electrocatalysis in alkaline media suggesting catalysts free of or extremely low in platinum-group metal (PGM) content could meet or exceed the activity and stability of PGM-based catalysts in acidic media.

The majority of present research toward AEMFCs is split between catalyst discovery and membrane development, the latter significantly accelerated through insights gained from the development of hydrocarbon ionomers for acidic media. In the field of AEM development, the major goals in the order of priority are chemical stability – specifically focused on alkaline conditions – and to a lesser degree high hydroxide conductivity and mechanical properties sufficient for integration into electrochemical devices.[84]

Membranes with chemical stability in alkaline solutions sufficient for proof-of-concept work have been developed at the laboratory scale. However, so far none of these materials meet the threshold of stability required for AEMFC commercialization.

[ii] For disambiguation, in the literature AEFMCs may be abbreviated as AMFCs or called alkaline anion-exchange membrane fuel cells, AAEMFCs; solid alkaline fuel cells, SAFCs; or hydroxide-exchange membrane fuel cells, HEMFCs.

Tokuyama A-201 membrane and AS-4 ionomer together serve as a de-facto baseline for all applications requiring alkaline stable AEM. However, these materials are no longer available to the research community. FuMa-Tech FAA-3 membrane represents the only alkaline-resistant anion-exchange membrane and ionomer solution with widespread availability with chemical stability sufficient for prototyping AEMFCs.

However, FAA-3 is only provided in NMP, a high boiling solvent that is a major barrier to industrial use, and apart from that no ionomer is widely available. Further, the only membranes commercially available are crosslinked, preventing the effective development of catalyst layers by conventional methods, and reducing ion conductivities.[85] This belies the fact that ionomer stability is particularly a challenge of the field, more so than membrane stability; the lack of an ionomer was identified as the single greatest barrier to the development of catalysts, MEAs, and systems for AEMFCs at the 2016 DOE AMFC workshop.[86] Compared to studies in acidic media, consideration of the ionomer separately from membrane has been extremely minimal, and no robust standards for the characterization of electrodes presently exist. Modeling is similarly preliminary, and requires pairing with rigorously controlled, fundamental experimental explorations.[87]

Beyond alkaline stability, the most important property for lifetime is hydrolytic stability. The requirement for high λ-values, the number of water molecules per functional group in a polymer, to minimize reactivity between hydroxide and the polymer require the membrane to maintain a full or near-full hydration state during operation. Other properties required for long-lived AEMs are unknown – oxidative stability is known to be important for applications in electrolysis, where the oxidative potential has been shown to rapidly degrade cathode ionomer, and water treatment, which commonly employs chlorine generation or HOCl/NaOCl. However, the requirement for other types of chemical stability for AEMFCs is unknown, in part because no membrane or particularly ionomer has yet been shown to be of sufficient stability in alkaline to observe other modes of degradation *in situ*.

Ex situ conductivities in membranes nearing that of hydroxide ion in pure water (200 $mS \cdot cm^{-1}$) have been achieved using numerous strategies for materials development. Hydroxide conductivity is considered to be three to four times the conductivity of chloride ions. Herring and coworkers have exerted particular effort in relating other anionic conductivities to that of hydroxide.[88] An anomaly has recently been found for bicarbonate transport, suggesting this involves hydroxide.[51]

The use of polymeric molecular design strategies initially employed in PEMs have proven effective for AEMs; for instance block copolymerization resulted in lowered dimensional swelling.[89,90] High toughness, indefinite alkaline stability, and processability as ionomer constitute a significant issue for materials with otherwise promising characteristics, but all these characteristics are necessary in a single material to create consistent and long-lived AEMFCs.

1.3. Catalyst Layers

1.3.1. Catalyst Ink Composition

The solid component of catalyst inks is comprised of supported catalysts and ionomer. The ink solvents are typically water-alcohol mixtures.The ionomer is usually dispersed in alcohols (MeOH, EtOH, IPA) or high-boiling aprotic solvents (DMAc, DMF, NMP, etc). Water is included to wet the highly active electrocatalyst powder, preventing the spontaneous oxidation of catalyst, catalyst support, and/or solvent. The dielectric constant is a measure of solvent polarity, and affects the degree to which a given ionomer is dispersed in the catalyst ink. Moreover, it determines the types of domains that are responsible for this dispersion (i.e. polar or non-polar domains), the type micelles that form of upon ionomer self-association in solution and the rate of sedimentation. Many properties of catalyst layers have been associated with dielectric constant of the initial solution, including catalyst layer porosity and electrocatalyst durability, while no clear consensus has emerged (see 3.5). The presence of high-boiling solvent(s) in the catalyst ink may result in large alterations to the dielectric constant and polymer solubility as a solvent mixture dries, and commonly used high-boiling solvents in catalyst inks may be highly polar, e.g. ethylene glycol, to non-polar, e.g. DMF. Provided the catalyst ink is well-dispersed, the method of application, the rate of solvent mixture evaporation, and/or the substrate employed (e.g. membrane, PTFE sheet, or carbon black/MPL) may have a greater impact on important catalyst layer properties, e.g. mesoporosity, than the dielectric properties of the dispersion medium (see 1.3.2).

The supported catalyst is typically comprised of platinum or platinum-alloy nanoparticles 20-70 wt% relative to the overall weight of the catalyst. Carbon support comprises the remainder (see 1.3.3). As a result, the choice of the electrocatalyst affects the thickness of catalyst layers substantially, with an order-of-magnitude difference between the two extremes: 20 wt% Pt/C corresponds a mere 2.2 vol% metal, while 70 wt% 1:1 PtRu/C is 21.2 vol% metal. Thinner catalyst layers have lower resistance than thicker catalyst layers. Beyond the minimal effect of this reduction in bulk resistance, there are claims that overall catalyst activity in increased, with one possible explanation being that thinner electrodes may reduce the effect of mixed potentials that comprise a portion of the difference between theoretical reversible potential and attainable OCV.[91–93] However, thinner catalyst layers are susceptible to earlier mass-transport losses from water transport.[94] assuming a 60% porosity in the catalyst layer, a fuel cell operating at 1000 mA/cm^2 results in 3.2 µm/s of water generated at the surface of a PEMFC cathode, or double that at an AEMFC anode. These units are a one-dimensional measure of water production in an electrode, independent of active area or catalyst layer thickness, convertible into the volume water that must be expelled into the GDL or back-diffused through the membrane per second for an MEA not to flood (for representative calculations, see Appendix C). In the case of AEMFCs, this is of larger impact than initially thought and the recent trend is towards developing thicker anode catalyst layers in AEMFCs.[95] Finally, higher-loaded catalyst layers are more expensive since they contain more precious metals.

1.3.2. Deposition of Catalyst Ink

The method of catalyst ink deposition exhibits substantial effects on the microstructure and properties of the catalyst layer. The methods can be broadly categorized in order of decreasing solvent residence time per layer: methods analogous to membrane casting that deposit the layer in a single step, e.g. die-casting or knife-over-roll, and subsequent heat treatment; inkjet printing onto a heated substrate, resulting in a small number of deposited layers and moderate solvent residence times; and ultrasonic spray-coating onto a heated substrate, resulting in many deposited layers and short solvent residence times. All of these methods have been employed to create electrodes industrially. Sputtering and other methods involving significant quantities of wasted electrocatalyst have fallen out of favour in the research community, despite their initial promise of high Pt-efficiencies.[96]

Higher deposition rates of solids in the catalyst ink are desired for the formation of large-area electrodes. High deposition rates may be achieved by any of these general methods, as increased substrate temperatures may be employed for rapid evolution of solvent. The number of deposited layers to achieve a given loading varies from one using casting techniques – the most consistent techniques being Mayar bar on the research scale and slot-die on the industrial scale – to tens of layers using picolitre-resolved inkjet printing techniques, to hundreds of layers with spray-coating.[97] While the total drying time for a given electrode may be equal between methods, the average residence time of solvent per layer decreases with the number of layers deposited.

It is notable that casting methods of electrode deposition result in cracked electrodes except in a handful of industrial roll-to-roll systems where solvent composition and drying rates are heavily optimized. Inkjet printing and spray-coating techniques that result in long solvent residence times, i.e. the length of time between ink deposition on a substrate and the evaporation of solvents from that ink to form the resultant dry catalyst layer. Spray coating using ink compositions and substrate heating to result in short residence times does not result in cracked electrodes.[98] Increased residence times are not consistently demonstrated to have an effect on total electrode volume, but a comparison of inkjet printing versus casting demonstrated a 20% gain in ECSA,[97] while a comparison of spray coating techniques demonstrates to have a statistically negative effect on the mass transport region of the polarization curve[98], despite preliminary theoretical work suggesting the contrary.[99] These differences suggest an alteration to the pore distribution in the catalyst layer, with increased mesoporosity associated with increased ECSAs and a reduction in mass transport losses both experimentally and by simulation on reconstructed catalyst layers by FIB/SEM studies.[100–104]

Additionally, annealing of PFSA-based MEAs via hot-pressing post-deposition has been demonstrated to have a significantly negative effect on both reproducibility and potentials achieved in the Ohmic and mass transport region. The effect is commensurate with the time and intensity of the annealing process. This calls into question methods incorporating a high-temperature thermal annealing or ‘baking’ step.[98,105]

The question whether cracked electrodes have a positive or negative effect on CL transport properties and durability remains an actively investigated question, albeit one where evidence increasingly points to the negative, and all three of these methods find application in commercial MEA production. Ultimately, it is beyond doubt that shorter solvent residence times alter the microstructure of resultant catalyst layers more than heating temperature or deposition method.

1.3.3. Supported Catalyst

The major concern in catalyst development is attaining high catalyst activity and high catalyst stability. Peak mass activity occurs around 3 nm particle diameters; however, smaller diameter particles are more susceptible to processes that alter and degrade catalyst layers, including particle transport, re-deposition, and Ostwald ripening.[106] As a result, Pt/C electrocatalysts used industrially employ larger Pt nanoparticles and catalyst supports than would result in the highest possible initial mass activity as a trade-off for increase lifetime. For instance, the representative TKK10e50e electrocatalyst comprises ~7 nm Pt nanoparticles supported on larger ~25 nm particles of graphitized carbon.

Even when carbon support is equal to or less than the mass of the metal electrocatalyst, carbon represents the large volume of the catalyst layer due to its comparatively low density. Carbon particles are typically far larger in diameter as well, thereby determining the overall free space between particles as layers form, the ‘void space,’ ultimately becoming the primary determinant of electrode internal volume. High void space increases total reactant gas and water transport through the electrode, the mass transport of which provide two critical limitations to the achievable activity of a fuel cell device.

However, conductive supports enhance the electronic conductivity of the resultant catalyst layer, particularly after the inclusion of electronically insulating ionomer, and thinner layers result in an overall lower electrical resistance of the catalyst layer. As a result, varying the wt% Pt of the supported catalysts results in substantially different catalyst layer volumes for a given catalyst loading. Thick electrodes (e.g. >10 µm) increase electronic losses as well as ionic losses within the catalyst layer (see 1.3.1). The overall electrode volume also plays a role in cold-start effectiveness.[107–109]

The chemical properties of a catalyst support also affect both the short and long-term operation of a fuel cell, strongly affecting the formation of the triple-phase interface (electrocatalyst, protons or hydroxides within the ionomer, and reactant gas – see Figs. 1.1 & 1.2) and long-term chemical stability of the electrodes, especially at the anode.[106,110] Carbon blacks and graphitized carbon are the two most common, commercially available catalyst supports, and these offer variations in the connected parameters of hydrophobicity/hydrophilicity, conductivity, long-term oxidative stability, and porosity. Porosity is expressed by BET surface area, which can vary from <10 to >2000 m^2/g and strongly affects water sorption and fuel cell activity.[53,100,111] Significant research is presently ongoing towards developing more stable carbon structures or entirely metal-based catalyst supports where catalyst degradation modes can be mitigated by electronically or physically enhanced catalyst-catalyst support interactions, or even physical encapsulation.[112–116]

1.3.4. Nano-Structured and/or Ionomer-Free Catalyst Layers

The reduction of Pt-content and the goal of reducing kinetic losses related to catalyst activation has inspired research into several types of ultra-thin, nano-structured catalyst layers, which may or may not contain ionomer. The real goal of both catalyst development and catalyst layer development is to achieve a high specific power, the power density per unit precious metal rather than reaction rate – $kW \cdot g^{-1}$ with respect to platinum, at an operationally relevant potential, i.e. 0.6-0.8 V. The archetypal example is the nano-structured thin film (NSTF) catalyst layers produced by 3M. These are extremely thin (from 1 µm to below 0.5 µm). While low in electrochemical surface areas comparted to conventional Pt/C electrocatalysts, ~20 vs. ~60 $m^2 \cdot g^{-1}$ Pt, 3M's NSTF maintains >5x the specific activity, which ultimately translates into an improved mass activity with respect to precious metal content. NSTF supports possess a highly porous, anisotropic structure that consists of a nano-forest comprised of lath-shaped, crystalline whiskers formed by annealing crystals of the organic dye perylene red. This structure allows for extremely high mass transport compared to traditional catalyst layers. Creating well-formed, enduring interfaces and resolving the requirement for higher fuel cell humidities that these CLs typically exhibit remain research foci. While typical NSTF CLs contain 3Mion as ionomer, many other thin film type catalyst layers[iii] have been theorized and produced in an attempt to achieve maximal mass activity of the precious metal catalyst or for fundamental studies.[67,117–123]

Theory compellingly suggests ionomer-free ultra-thin films may result in highest possible activities from PGM content in the catalyst layer. The regular structure of these catalyst layers has, in combination with modelling, enabled the probing of fundamental questions of catalyst layer transport properties that were previously very difficult to delineate experimentally with irregularly structured electrodes.[120,124]

1.4. Considerations in MEA Construction

1.4.1. Interfacial and Morphological Effects

As described previously, a membrane-electrode assembly (MEA) is comprised of a membrane, two electrodes, and two gas-diffusion layers, typically with microporous layers. Several methods exist for forming MEAs, depending on the method of forming the GDL-electrode and electrode-membrane interfaces, including gas-diffusion electrodes (GDEs). All of these techniques may be accomplished with or without hot-pressing.

Catalyst-coated membranes (CCMs) refer to the direct deposition of the catalyst ink onto the membrane, with subsequent addition of GDLs. The membrane-electrode interfacial resistance is the largest interfacial resistance in the cell, thus the CCM approach is considered the most effectual in lowering overall resistances.

Decal-transfer of an electrode formed on another substrate may also be used to form CCMs or GDEs. This may be beneficial to consistency and scrap rate versus the GDE approach and prevents potential membrane damage and processing issues caused by the CCM approach, but removes the lower interfacial resistances achieved by either the CCM or GDE approach.

[iii] Thin filmtype CLs are described in many ways, for instance extended thin film catalyst layers, ETFCLs; alternating catalyst layer structure, ACLSs; or ultra-thin catalyst layers UTCLs)

Hot-pressing is generally coupled with the GDE and decal-transfer methods of MEA formation, and occasionally with CCMs. It may improve power densities when catalyst layers are formed with low mesoporosity[125] or using ionomer with innately poor properties and/or quantities unsuitable for the formation of high electrocatalytically active surface areas (see 1.2.3).[126] However, hot-pressing anneals catalyst layer microstructure and reduces ECSA, and even its consistent, regulated use results in increased mass-transport losses; in addition to these losses, this also results in substantially increased variability cell-to-cell, of profound importance to the discovery of structure-property relationships *in situ* operation and thereby the field of materials discovery for fuel cells as a whole.[98] While some compression is necessary in stack loading to balance the loss of oxygen diffusion in the GDL with the improved interfacial resistances between components, simple compressive stress is not accompanied by ECSA loss, and this balance may easily be achieved by rational selection of gasketing.[105] Thus, the CCM approach without hot-pressing is presently considered the state-of-the-art construction, resulting in consistent operational and achievable current and power densities mirroring industrial reference data.

The direct membrane deposition method (DMD) has recently been rediscovered by academia.[127] This involves the creation of a GDE and subsequent deposition of a membrane on top of this, the initial method being highly regulated piezoelectric inkjet printing. This method creates a new membrane-membrane interface and requires the use of a sub-gasket between layers to prevent gas and electrical crossover around the edges (see Fig. 5.1). However, this method also improves both the electrode-MPL and membrane-electrode interfaces, reducing the resistances attributable to these. The net result is a large improvement to achievable power densities, with preliminary results suggesting an additional improvement attributable increased water transport through the membrane. This approach eliminates the need for membrane casting, allows for easily varied membrane thicknesses, and allows for the comparatively facile addition of additives and reinforcements to any or all layers. This general approach was initially attempted by researchers at Gore in the 1990s and ultimately abandoned due to high scrap costs – membrane defects result in catalyst being discarded, unlike in other approaches – but the large gains in the quality control of gas diffusion layers since then alongside large improvements in the understanding of system water management in relation to high-activity electrocatalysis amply warrant further research into this method.

1.4.2. *In Situ* Effects of Reducing Precious Metal Content in PEMFCs

A significant push within solid-state materials chemistry has been the development of low precious metal content, no precious metal content, or no metal content altogether.

Reducing catalyst loading in catalyst layers increases kinetic losses, exacerbated by oxygen transport resistances; the most consistent current explanation for this phenomenon is that increased mass activity contributes to local ionomer solubility, that in turn increases overall film transport resistances,[128–132] more than counteracting increases to ECSA and overall mitigating achievable mass activity.[119] Thinner catalyst layers slightly reduce Ohmic losses due to lower bulk resistance of the CLs but also result in earlier and more severe water transport losses (see Appendix C).

As a result, thicker but high metal content catalyst layers are preferable to achieve high mass activities with respect to PGM content alone, where highly active but more dispersed reaction sites are desirable. The present strategies employed involves alloying platinum with other platinum-group metals (PGMs) to improve catalyst function and/or stability, creating non-PGM alloys such as with cobalt, the present industrial preference, or using either of these two general strategies but forming core-shell or more exotic non-random configurations of alloyed nanoparticles.[120,133–135] Altogether, both catalyst and ionomer design is necessary to address the challenge low Pt loading present.[121]

Another focus of the field has been on doping graphene or carbon nanotubes (CNTs) to create non-PGM catalysts[136–139] or entirely non-metal catalysts[140] to reduce the effect of thickness, but stability data is under-reported and the only known commercialization of this technology is by Ballard Power Systems & Nisshinbo, presently incorporated into low-spec power systems for applications where atmospheres may become heavily contaminated with NOx or SOx, such as in remote detection systems for volcanology.

MEA design has been altered to accommodate lower loadings; thinner membranes allow for greater water back-diffusion and lowered ionic resistance, compensating for the greater activities and concomitant greater water produced as a fraction of CL free volume (see Appendix C). The general measure of turnover per Pt in the catalyst layer as a whole is called Pt-efficiency, and is typically reported in kW/g Pt or occasionally its reciprocal, g Pt/kW; the 2020 DOE target corresponds to 8 kW/g in air. Significant efforts in exotic catalyst layer deposition methods,[141–143] reached 35 kW/g Pt, while application of the ‘direct membrane deposition’ method as developed in chapter 3, which features enhancements to water transport and interfacial resistances, resulted in 88 kW/g Pt using commercial electrocatalyst and a catalyst layer fabrication process already adapted for mass-production.[144]

1.5. Objectives of this Research

Using characterization methods described in Chapter 2, the objectives of this research are to:

1) Explore the interrelation of catalyst layer composition, microstructure, and transport properties for catalyst layers incorporating hydrocarbon ion-exchange membranes as ionomer in the catalyst layer through physical and electrochemical characterization for both PEM- and AEM-based systems. This objective is addressed in Chapters 3 and 4, respectively.

2) Examine the effect of catalyst ink composition on catalyst layer microstructure in the context of the industrial standard method of catalyst layer deposition. Specifically, the effect of high-boiling solvents on the microstructure and on the *in situ* conductivity of spray-coated catalyst layers were investigated for both PEM- and AEM-based systems. This objective is addressed in Chapters 3 and 4, respectively.

3) Investigate a new fuel cell architecture that maximizes water transport and minimizes interfacial resistances to the point where long-lived, high-efficiency (i.e. low fuel and electrical crossover) fuel cells are obtainable. Developing consistent methods suited to mass production is address in Chapter 5.

Chapter 2. Methods

2.1. MEAs *In Situ*

2.1.1. Operating MEAs as Fuel Cells

The standard operational conditions for PEMFCs at the 5 cm^2 research scale are 80 °C and H_2/air, 1.5-2 atm backpressure, and high gas flows. This size is standard for laboratories focused on materials discovery. While high gas flows may result in stoichiometries greater than 20 across the entire polarization curve, this nevertheless mimics optimized, well-manifolded full systems near stoichiometries of 1 – i.e. where reactant gas inflow is equal to its use across the active area, particularly of importance to the hydrogen-reacting anode – as the stoichiometries across the majority of a large surface maintain a ratio much greater than 1. Not all of these conditions are ideal conditions for conducting research on new materials, especially the use of backpressure. Replacing the cathodic air feed with oxygen is a generally accepted substitute for backpressure, allowing operation at relevantly high current densities without the need for whole-system optimization of heat and water flux, alongside faster cell conditioning (see below).

Backpressure increases achievable power densities by improving ORR kinetics due to the higher partial pressure of oxygen at the active site. Backpressure additionally reduces membrane swelling, improving the conductivity of the membrane. Together, this results in reduced kinetic losses and an extended Ohmic region, substantially increasing achievable current densities together with improved efficiency at a given current density and a higher maximum achievable power density. However, backpressure causes water management issues and resultant hysteresis at high RH. Furthermore, any differential will exert added mechanical stress upon the membrane. As a result, zero backpressure makes 100% RH the idealized conditions for all common IECs of PFSAs (0.9-1.1 $meq \cdot g^{-1}$), allowing for highly consistent comparison between cells employing non-PFSAs in the catalyst layer and/or membrane or otherwise altered cell construction, all without the need for extensive optimization of RH and backpressure to achieve a fair comparison to the reference.

Temperature also plays a large role in fuel cell kinetics; while higher temperature reduces theoretical OCV marginally, improvements to ORR kinetics and reductions to the effects of CO poisoning vastly outweigh this consideration (see 1.2.1). However, in PFSA references, several issues result above 80 °C. A PFSA will creep at an operational temperatures above its T_g, causing membrane thinning and a resultant decrease to cell lifetime, among other issues. Second, water management requires increased fine-tuning as the temperature approaches 100 °C under zero backpressure; high relative humidities under these conditions result in water vapour constituting a significant proportion of the atmosphere.

Finally, PEMFCs reach a meta-stable steady-state polarization, a process commonly known as ‘conditioning,’ ‘ significantly faster under an oxygen atmosphere. In the case of reference PFSAs, a PEMFC running under oxygen at zero backpressure will typically obtain current densities and efficiencies equal to or slightly higher than in air under 2 atm, attributable to the higher partial pressure of oxygen obtained under these conditions. However, attaining high current densities without backpressure better probes water management while removing the effect of backpressure on water management. Thus, operation in oxygen at 80 °C provides a fair approximation to industrially relevant conditions with the benefits of added consistency between cells. Operation in air at zero backpressure provides minimum values to attainable current densities and may serve to corroborate differences in structure-property relationships of ionomer in the catalyst layer, particularly related to oxygen permeability.

2.1.2. Gasketing & Compression

Compression in the 100-500 kPa range is the ideal compression of a fuel cell stack, corresponding to a 20-30% compression of a typical commercial GDL. Compression in this range balances the reduction in oxygen diffusion and water transport through the gas diffusion layers with the decreases to the two GDL interfacial resistances that result as stack compression increases.[105] While gasket choice gives a theoretical compression of the gas-diffusion layers, the pressure achieved experimentally may be determined easily by the use of pressure-sensitive film of the appropriate range.

Figure 2.1: **Setup of a fuel cell including: a.) a gasketed MEA before second flow field, current collector, and hardware addition + compression; b.) pressure paper demonstrating sufficient compression of the GDLs (dark lines following flow fields ridges but not connecting); c.) resultant fuel cell in operation on the fuel cell test station.**

Gasketing methods and materials are unimportant for short-duration fuel cell operation so long as these seal adequately and do not flow under the temperature regimes studied. However, gasketing methods and material choices exert a substantial impact on cell lifetimes both at the research scale and in real use. Imperfect sealing results in micro-crack formation near the gas inlets.[145] Importantly to the acceptance of hydrocarbon membranes, recent work has shown the disproportionate impact of soft gasketing and particularly soft GDLs to the lifetimes of hydrocarbon membranes under humidity cycling, the accelerated stability test for the mechanical durability of a membrane; block copolymer sPEEK, a fully hydrocarbon membrane with greater swelling and reduced relevant mechanical properties such as elongation at break than reference PFSAs, exhibited lifetimes on par with reference PFSAs.[47] State-of-the-art methodology is to employ chemically robust, high-temperature self-adhesive gaskets, such as polyimides with silicone adhesives, slightly overlapping the catalyst layer.

2.2. *In situ* characterization of membrane and catalyst layer

For the understanding of new materials, it is vitally important to study new materials *in situ* as the constitutive elements of full fuel cells in half-cell and full-cell setups. *Ex situ* data gives an idea of how materials will perform in relation to an already-known materials set, but the use of ion-exchange materials in electrochemical systems represent a confluence of many factors and parameters that cannot be directly measured *ex situ.* As a result, *in situ* data is necessary to accurately determine the impact of new materials on device lifetime and efficiency. *In situ* work measures properties in an environment substantially more consistent with that intended for them and also allows for many forms of characterization otherwise impossible. Ion-exchange membranes are dynamic in operation and the system 'conditions' with time, so *in situ* methodologies are the only mechanism for studying fully conditioned materials, the properties of which may vary to those determined *ex situ*, in some cases substantially. This is particularly relevant in the case of AEMFCs, where even the most standard characterization methods on a membrane in the hydroxide form are challenging to manage successfully due to carbonate contamination caused by exposure to air, a process effectively irreversible apart from operating the cell *in situ*.

2.2.1. Polarization Curves (IVs) and the Need for Steady-State Data

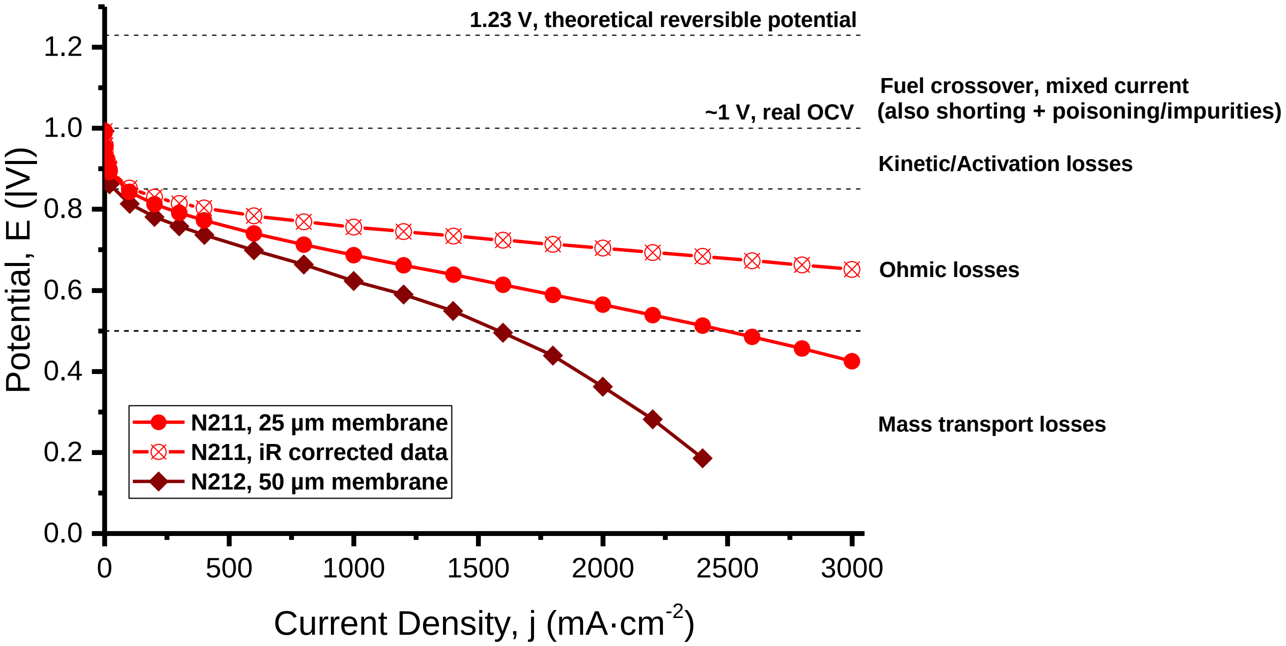

Figure 2.2: **Nafion® 211 and 212-derived polarization curves illustrating (top to bottom); i.) losses between the theoretical reversible potential and effective open-circuit voltage caused primarily by fuel crossover and mixed currents with potential but generally insignificant losses from electrical shorting and catalyst poisoning or impurities; ii.) losses in the kinetic region from catalyst activation; iii.) Ohmic losses attributable to membrane resistance – compare 25 µm N211 and 50 µm N212, the latter with close to double the total membrane resistance as well as N211 and 'corrected' data for Ohmic losses (see 2.2.2); iii) mass transport losses mainly attributable to oxygen starvation exacerbated by cathode flooding and anode dehydration, most noticeable in N212.**

Polarization data may be measured with an operating fuel cell, either by incrementally setting current densities and measuring potential (the preferred method in this work, which better resolves the Ohmic and mass-transport regions and compares points of equivalent reaction rate among a data set) or by incrementally setting potentials and measuring current (potentiodynamic polarization). A minimum of five minutes per point is necessary at current densities from the Ohmic region to equilibrate to water content through the CL, MPL, and GDL, compellingly demonstrated with in operando synchrotron XRD experiments on PEMFCs.[146] While this results in a large increase in time per polarization curve, this is necessary to reach steady state and accurately probe the ability of a given MEA to manage water under the stated conditions.

For AEMFCs, water management is significantly more critical. Twice the number of water molecules are transported per electron generated as in PEMFCs (Equations 1.3 and 1.4); water is a reactant at the cathode, compounding the issue of dehydration by electro-osmotic drag; and the hydration state of membrane and ionomer strongly influence their chemical stability. AEMs are not stable when dry in their hydroxide form, susceptible to hydroxide attack when low λ-values reduce the hydroxide-to-functional group distance and to rapid carbonation.[147] Even given materials with excellent alkaline stability, carbonation would preclude processing MEAs in hydroxide form. Additional complicating factors include the necessity of conversion into the hydroxide form, the significantly greater effects of both cations and anions on the ORR and HOR in alkaline media.[148,149] Conversion of MEAs into hydroxide form after they have been formed leads to integration of MEAs while wet. In situ, this potentially results in an early hydroxide-doped state before steady-state operation may be achieved. In the literature, the length of time holds at a given current density or potential are often short, not clearly reported, or not reported at all. If no steady state results are reported, either through long hold times or repeated IVs on a given MEA, the accurate comparison of AEMFC data between studies is rendered impossible.

2.2.2. Membrane conductivity – Internal resistance (iR) from current-interrupt and iR-corrected IV plots

The combined hardware electrical resistance and polymer electrolyte resistance, known as iR drop, is determined *in situ* by one of two methods, the current-interrupt method or high-frequency resistance. In the current-interrupt method, the circuit is briefly interrupted, on the order of 20-200 µs, the instantaneous measured ΔV (increase) / ΔI (decrease) equals ΔR, equivalent to the high-frequency resistance (HFR) found by EIS – both techniques effectively short polarization but not membrane/ionomer resistance in so doing. The difference between these techniques is that the HFR accurately measures resistance at lower current densities (e.g. mid-kinetic region). The frequency response analyzer (FRA) that finds HFR is also useful for determining *in situ* polarization resistance and other outputs of EIS analysis. As a result, in-line FRA is typically included instead of a current-interrupt system in contemporary fuel cell test equipment.[150]

Additionally, correcting for non-MEA resistances in a fuel cell is necessary to find *in situ* membrane/ionomer conductivity. Hardware and GDL resistance in relevant conditions to fuel cell operation may be found, and thereby offset in analysis, by finding the HFR of a fuel cell setup without the CCM and gasketing to ensure GDL compression equivalent to that in a full setup.

Polarization data occasionally has the measured voltage loss to iR added back in (described as ‘iR corrected’ or ‘iR free’ polarization data) to highlight polarization curves independent of membrane resistance and mass-transport. This approach may be helpful in non-optimized systems, particularly when mass transport resistances start early for one cell versus another due to overall water transport issues at high humidities; i.e. this is an eminently surmountable problem that isn’t particularly of scientific interest. Operational conditions and every component, most importantly the GDL, have been optimized to PFSA membranes. However, corrected polarization curves are frequently misused to minimize the perception of negative impact where membranes more highly resistive than current standards have been employed. This is especially problematic with AEMFCs, where no clear standard material set or performance exists as a baseline at present. As a result, rationale for the inclusion of corrected data must be spelled out clearly in every instance or the overall effect is misleading.

2.2.3. Lifetime – Accelerated Stress Tests (ASTs)

As fuel cells may operate at an acceptable efficiency for an order of magnitude or more longer in ideal conditions than in start/stop operation, accelerated stress tests have been developed and continuously updated to match industrial data for real lifetime tests; the current trend is towards combined a chemical/mechanical degradation test for the membrane, which can be performed on new, automated systems enabled with automatic RH, gas, and even backpressure switching. Combined chemical/mechanical stress tests have less bearing at a materials discovery level, where chemical degradation is a fundamental albeit improvable with additives but mechanical strength may be enhanced using various reinforcement strategies. Thus, these two parameters ought to be tested separately at the early research scale.

However, for membranes designed to scale from the larger research scale (e.g. 25-100 cm^2 and greater), combined testing should be performed. Contemporary fuel cells rely heavily on additives to enhance the chemical and mechanical stability of the membrane and catalyst layers (among other properties such as hydrophilicity), so a combined stability test is intended to allay the optimization of one parameter at the expense of the other. Real *in situ* degradation modes cannot be simulated in ASTs, hence the need for continuous improvement of AST methodology and correlation between ASTs and real use-case data. For instance, platinum banding caused by CL degradation may exert a positive effect by blocking fuel crossover, and some events in real systems such as Cerium migration and freeze-thaw cycles can result in problems, e.g. water-based mass transport losses, that are difficult to simulate in accelerated tests. Cerium-based additives and other radical traps both inorganic and organic have been extremely effective in increasing fuel cell systems lifetimes, including in ASTs, and this has lead to overly long ASTs. As a result, a heavy accelerated stress test (HAST), intended for use on fully reinforced and additive-enhanced systems, has recently been developed.[151–153154]

ASTs for electrocatalyst and electrocatalyst support remain separate. GDL degradation, while industrially important, does not have its own DOE-defined AST. GDL stability is likely too interlinked with the membrane and electrocatalyst/ionomer system (e.g. membrane degradation products or long-term electrode volume) to be effectively separable into a predictive test for absolute lifetime *in situ*.

For materials discovery, several levels of accelerated stress test exist – the first is the Fenton test, an *ex situ* test for membrane chemical stability that primarily represents a test for radical stability – an iron metal catalyst and peroxide are mixed, acting as a peroxy radical generation medium (see 1.2.1 for standard conditions in acid and effect on Nafion). Mass loss versus time acts as a measure of relative stability. In this test, hydrocarbon-based membranes typically fare poorly compared to PFSAs, and as a result very few hydrocarbon membranes and even fewer fully hydrocarbon systems have been subjected to further ASTs. Hydrocarbons have profoundly positive environmental and economic considerations relative to PFSAs (e.g. sPEEK as an exemplar hydrocarbon exhibits a >5x lower cost floor and greater than order of magnitude decrease in energy use compared to Nafion)[155] but higher resistances leading to lower achievable power densities, industrially difficult-to-use processing solvents, and limited lifetimes – particularly a result of brittleness caused by chemical degradation on top of innate chemical properties such as higher crystallinity than Nafion and lower elongation at break – the outlook for the adoption of hydrocarbon membranes in real systems looked poor until very recently. According to recent presentations by researchers at Toray Industries, Inc., hydrocarbon membrane systems do not exhibit platinum banding, unlike PFSA-based systems. This may indicate a protecting effect on electrocatalyst. Also, when inculcated with organic radical scrubbers, Toray's exhibit equal *in situ* lifetimes to Nafion HP (ePTFE reinforced, 20 µm membrane), while maintaining comparable efficiencies.[156,157] Lower gas transport of hydrogen has been reported extensively in the literature, but lower nitrogen crossover results in greater total hydrogen use in real, air-breathing systems where hydrogen is recirculated rather than operated at a stoichiometry of 1. Two new generations of hydrocarbon membranes – containing structural motifs for desirable properties including either protected ether groups or ether-free architectures – are of significant current research interest. While enhanced lifetimes in the Fenton test are limited to the latter category, ASTs performed on both types of systems have progressed from promising to extremely promising as a future PEMFC membrane standard for enhanced system lifetimes and efficiencies.[75,81,158–162]

2.2.4. Gas crossover and shorting – Chronoamperometry (CA) and Linear Sweep Voltammetry (LSV)

Fuel crossover (hydrogen crossover) from anode to cathode results in direct reaction in the cathode catalyst layer. Depolarizing the cathode under nitrogen and applying a potential re-purposes the fuel cell cathode catalyst layer as an anode for the HOR, and the rate of this reaction quantifies the rate of crossover.

The most common method of determining fuel crossover is through chronoamperometry, Figure 2.3, where polarization occurs in 100 mV increments, causing an initial Faradaic reaction tapering to the steady-state HOR. Crossover is typically measured as the steady state current density at 0.5 V, i.e. with the electrode fully activated, in the following work taken experimentally as the average of all points from the initial minimum or last ¼ of points taken at that potential.

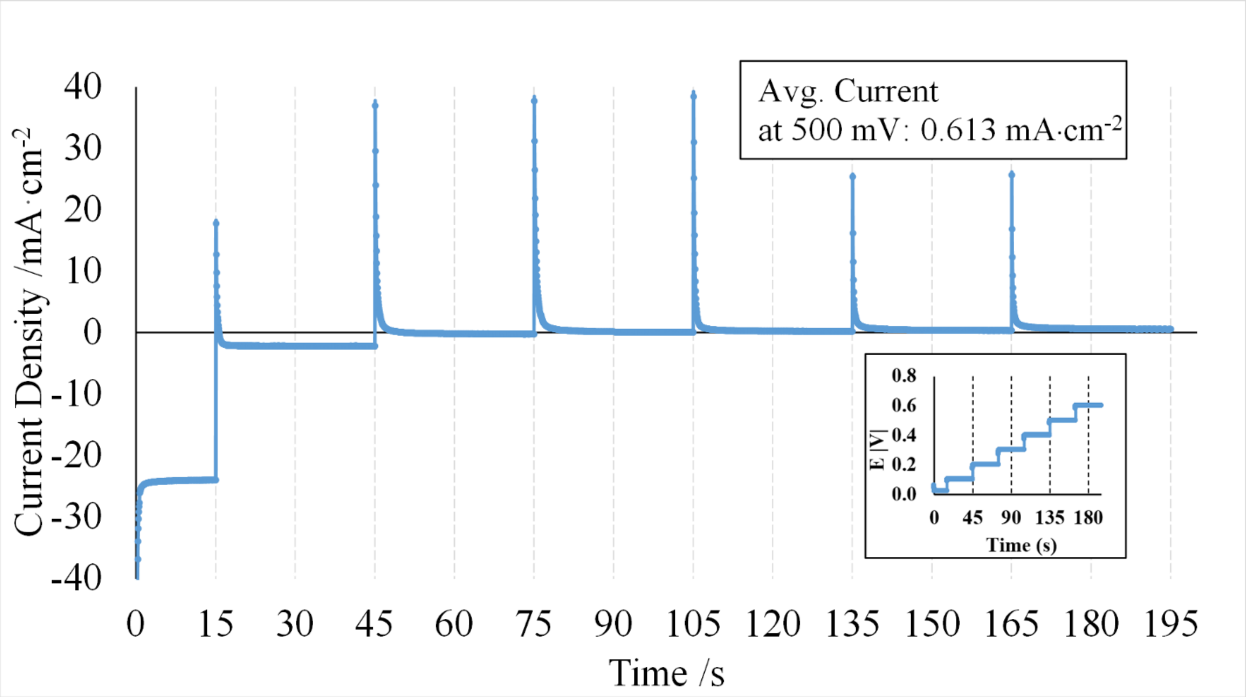

Figure 2.3: **Chronoamperometry diagram showing current density for Faradaic (spikes) and crossover (steady-state) versus time for the potential ramp at 100 mV increments from 0 to 0.6 V as shown (inset).**

The combined chemical/mechanical AST requires the determination of electrical shorting by the application of a potential across the membrane, but few papers beyond those performing this AST perform a check for shorting, and in fact many papers at the materials discovery level skip this portion of the AST. However, it is important to determine whether electrical shorting is a source of voltage losses in a given fuel cell setup. This could be determined as the slope of the averages between the later steps of a CA, but in practice this is far easier and more compellingly determined by linear sweep voltammetry (LSV). LSV does not determine a steady-state crossover value and as a result over-approximates crossover, but does readily determine the presence or absence of electrical shorting, Figure 2.4.

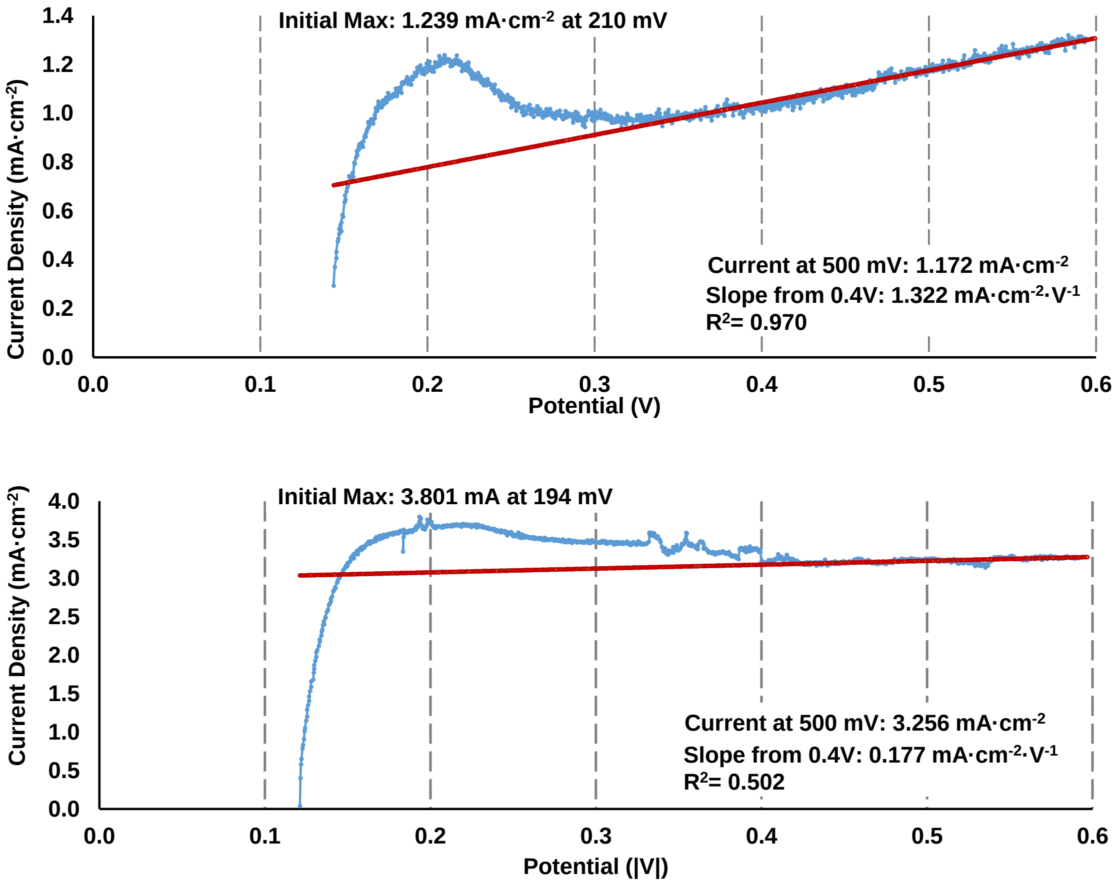

Figure 2.4: **Linear sweep voltammograms, the technique notable for initial hydrogen desorption followed by a current density minimum approximating the steady-state hydrogen crossover, with examples illustrating a.) a low-crossover fuel cell with a minor electrical short (highly linear slope from minimum following V = iR); b.) a moderate-crossover fuel cell free of electrical short.**

2.2.5. Electrocatalytically Active Surface Area (ECSA) and Double Layer Capacitance (C_{DL}) – Cyclic Voltammetry (CV)

In cyclic voltammetry, a nitrogen-depolarized cathode with inert gas flow over the cathode will reversibly reduce and adsorb hydrogen in close to equal quantities. Using established parameters for Pt surface area, ECSA may be calculated from the current passed to generate the hydrogen adsorption and desorption peaks (Fig. 2.5 – see also Chapters 3 & 4). The differences between H_{ads} and H_{des} are small and replicable across multiple cycles, leading to acceptably small error bars in practice. Double-layer capacitance relates to the current difference between the forward and reverse cycles in regions where no Faradaic reaction is occurring (e.g. 0.35 to 0.65 V in acidic conditions).

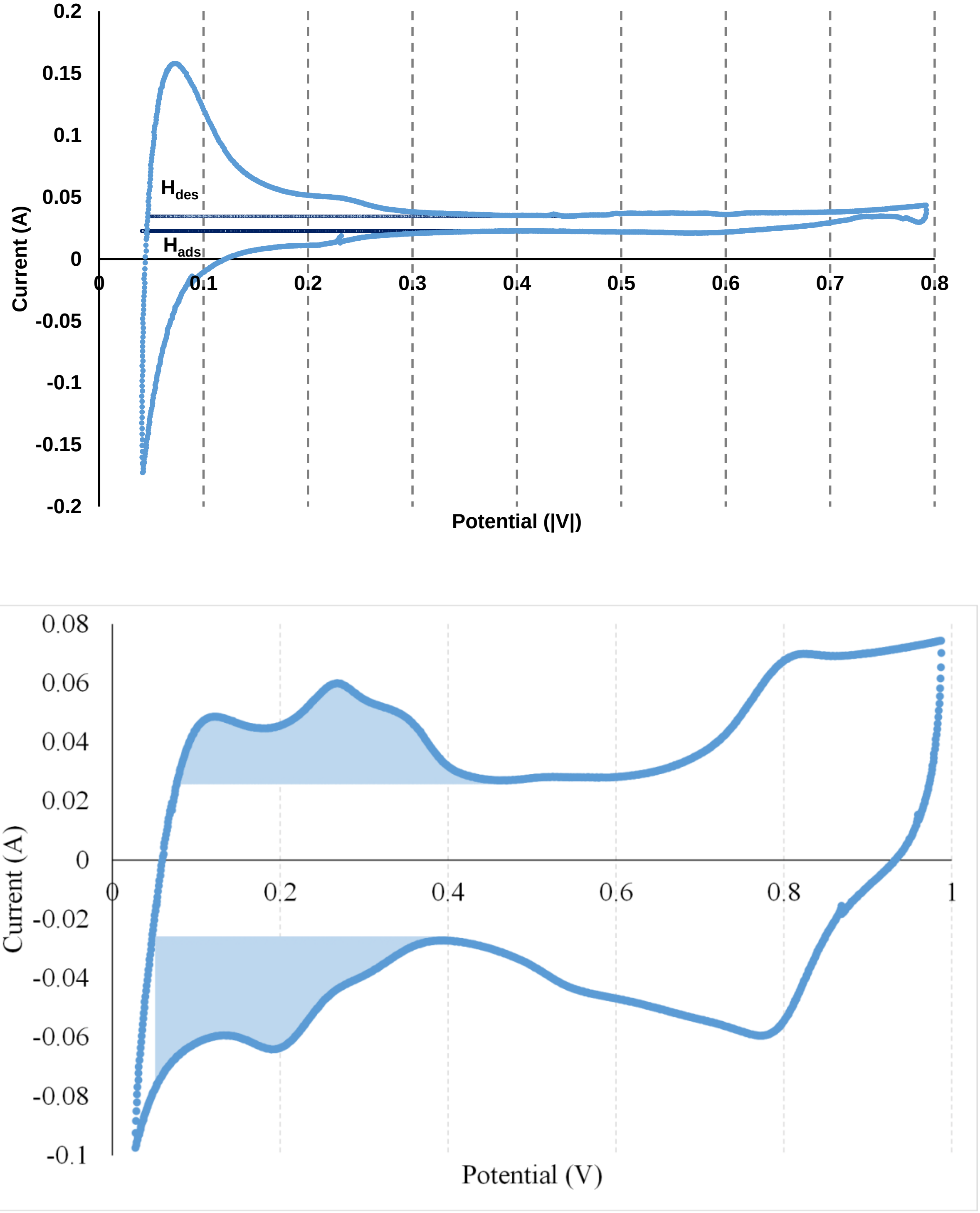

Figure 2.5: Cyclic voltammograms (CVs), current against potential vs. RHE, in a.) acidic and b.) alkaline conditions with H_{ads} and H_{des} as illustrated; double-layer capacitance was considered to relate to half the distance between the minimum potential on the forward wave and maximum potential of the reverse wave in the non-Faradaic region ~0.3-0.6 V.

While *in situ* CVs are certainly the most facile method to determine ECSA, some experiments require a higher degree of accuracy. In particular where there is a desire to quantify catalyst poisoning or the performance of electrocatalyst under non-ideal conditions (e.g. in an environment other than the standard 100% RH, 80 °C), CO displacement has been proposed as a highly consistent method of measuring the adsorbed ions on the Pt surface. Furthermore, CO adsorption doesn't require proton or water transfer to catalytic sites. As a result, it has been shown to be RH-independent experimentally and may be considered the most consistent method of determining ECSA.[163]

Pt nanoparticles in the standard Pt/C employed in these experiments have a nominal diameter of 5 nm reported, giving a theoretical maximum ECSA of 56 $m^2 \cdot g^{-1}$ Pt for spherical nanoparticles (see Appendix C). However, ECSAs are frequently measured in the literature greater than this, and for references in Chapters 2-4, suggesting both high overall surface activities and that the initial conditioning/aging process increases active surface area in the early stages of fuel cell lifetimes.

2.2.6. Proton Conductivity of the Catalyst Layer and Other Transport Resistances – Electrochemical Impedance Spectroscopy (EIS)

A frequency-response analyzer (FRA) may perform electrochemical impedance spectroscopy (EIS) on fuel cell systems in operation or equilibrated under nitrogen. EIS is a powerful technique that if considered simply, can be used to determine cathode activation and mass transport losses in a fuel cell system as well to as validate the Ohmic losses found in *in situ* operation, and with more detailed analysis determine anode activation losses; given a highly stable and well-shielded system, anode activation losses and both anodic and cathodic exchange current densities may be determinable.

The Nyquist plot (Fig. 2.6b) is a plot of the imaginary vs. real components of impedance, with the x-axis representing resistance. This is the standard, most common, and most accessible representation in the study of fuel cells. As the cathode comprises the lead non-membrane resistance in a fuel cell, a Randles circuit is used as an equivalent circuit model for curve fitting (Fig. 2.6a, top), with the constant-phase element (non-ideal capacitor) and resistor together representing CL impedance, and the system resistor representing the sum of membrane, GDL/MPL, flow field, and current pickup resistances as the x-intercept, known as high-frequency resistance, HFR. The low-frequency resistance, LFR, is the x-intercept of a line fit to the low frequency data when equilibrated under nitrogen (in operational conditions, this represents the sum of charge transfer and oxygen transport resistance). The Randles circuit fits the semicircle related to cathode resistance, while more sophisticated models fit a Warburg element to model oxygen diffusion (Fig. 2.6a middle), and even more sophisticated models add elements for contact resistance and anode (Fig. 2.6a bottom).

However, in experimental studies on fuel cells with a focus other than EIS theory or methodology, curve fitting is onerous and difficult to reproduce in multiple analyses of a given measurement, leading to potential large and difficult to quantify errors in determined data. As a result, a simplified method may be employed to determine the charge-carrier conductivity of ionomer in the catalyst layer, the data most of interest with respect to characterizing ionomer in the catalyst layer *in situ*, by considering the horizontal distance, i.e. resistance, between the HFR and LFR intercepts as 1/3rd of the total resistance of the cathode catalyst layer. This ultimately determines the charge-carrier conductivity of the ionomer in the catalyst layer according to accepted theory.[164,165] While this method is simplistic compared to equivalent circuit modelling, it is highly reproducible across a large range of experimental conditions even with a system of limited stability as with AEMFCs (see Table 4.5) and instrumentation with relatively high noise and inductance causing a limited frequency window (e.g. 10-10,000 Hz) as was employed in Chapters 3 & 4, compared to the high stability and highly shielded instrumentation required for membrane impedance (i.e. < 1 Hz to > 10^6 Hz).

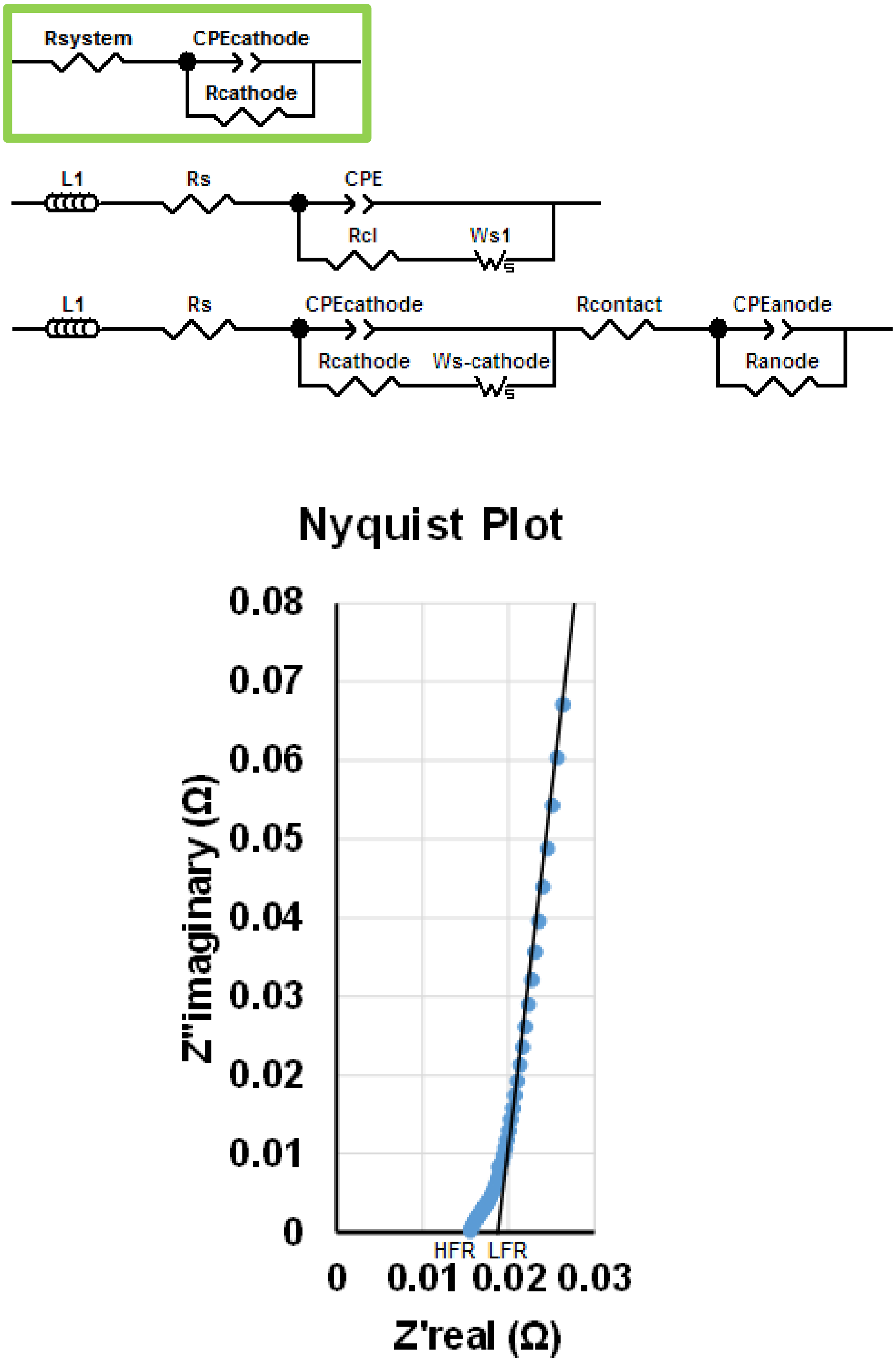

Figure 2.6: a.) Basic equivalent circuit models used for EIS analysis in the literature including i.) simplified Randles Circuit with a constant phase element for a real capacitor; ii.) inclusion of inductance and Warburg impedance elements; iii.) inclusion of contact resistance and simplified anode impedance; b.) Equivalent Nyquist plot derived from EIS data illustrating the high-frequency intercept (HFR, blue) and low-frequency intercept by linear fit of low-frequency data (LFR).

2.3. *Ex situ* characterization of catalyst ink & catalyst layer

2.3.1. Catalyst Ink Composition by DLS, SAXS, & SANS

Ionomer dispersions are complex structures, forming micelles ranging from spherical to lamellar depending on the ionomer-solution interactions. Solvent interactions with the ionomer determine the properties of ionomer films cast out of solution. Solvent mixtures resulting in phase-inversion create asymmetric, porous films, while highly solvating solvent mixtures result in dense, cohesive thin films forming.[166]

A catalyst layer is further complicated by the addition of catalyst nanoparticles further complicates the interaction in the catalyst/ionomer dispersion, or 'catalyst ink,' with ionomer-ionomer and ionomer-supported catalyst interactions occurring simultaneous to supported catalyst-supported catalyst aggregation. Dynamic light scattering (DLS), small-angle X-ray scattering (SAXS), and small-angle neutron scattering (SANS) are increasingly methods of determining these interactions. DLS captures back-scattered lasers and from perturbations in the predicted Brownian motion of a particle-free solution determines average particle sizes as their solvodynamic radii, however accuracy requires greater dilution than generally present in catalyst inks. SAXS (the through-solution version of GISAXS, as described below) and SANS (a better-resolution but experimentally more difficult technique) may determine both particle radii and ionomer cluster size within a catalyst ink. Aggregate size in solution interacts with the catalyst ink deposition method and substrate temperature to determine the catalyst layer microstructure.[100,167,168]

2.3.2. Imaging Catalyst Layers – Optical, SEM, EDX, ICP-MS GISAXS

Several imaging techniques exist for catalyst layers, roughly grouped into two families. The first is feature-based imaging, including confocal optical imaging (e.g. for determining cracking or other macroscopic features), imaging by electron microscopy (SEM), and focused ion beam sectioning and algorithm-based reconstruction (FIB-SEM). The second family is composition-based imaging. Energy dispersive X-ray spectroscopy, EDX, (see Fig. 1.3 for a simple line-based tracking of fluorine, platinum and sulfur in a 5-layer MEA). This technique is based on an added detector to SEM systems that captures back-scattered, non-Auger electrons. Laser-ablation inductively coupled mass spectrometry (LA-ICP-MS) subjects small clusters of atoms ejected by the rastering of a high-energy laser across a surface to analysis in an ICP-MS system. Finally, grazing-incidence small-angle and wide-angle spectroscopy (GISAXS/GIWAXS) provides the most common composition-focused imaging technique for fuel cell ionomer-substrate interactions.[169]

Of these techniques, most are well-documented and result in relatively unequivocal data. For example, optical imaging and SEM gives a non-quantitative but adequate sense of catalyst layer microstructure and macrostructure, respectively, particularly when viewed in three dimensions. EDX mapping is powerful as a reverse-engineering technique and to determine the effects of aging. FIB-SEM and GISAXS are the exception – these techniques potentially lend great insight into the ionomer-catalyst interactions within a fuel cell catalyst layer or the CL-MPL or CL-membrane interactions without, and are both intensely used and intensely scrutinized in contemporary literature.

FIB-SEM sections and reconstructs catalyst layers, turning SEM into a semi-quantitative method and complementing or even potentially replacing porosimetry techniques for the determination of catalyst layer microstructure. The sectioning itself is straightforward, but the difficulty lies in the reconstruction of the catalyst layers themselves. FIB sectioning is a high-energy technique to which soft materials are being subjected to, so the cuts are not necessarily clean, and algorithms are necessary for the statistical reconstruction of the fit between sections. Although SEM is conducted under high vacuum, i.e. with dry ionomer unlike in real fuel cell operation, new techniques may allow the modelling of water saturation and resultant gas permeabilities and mass transport properties of the catalyst layer.[22,59,102,137,170–172]

GISAXS uses soft X-rays from synchrotron facilities and can image the *in situ* operation of fuel cells, which dynamically provides a map of both features and compositions to a <10 nm resolution (~1.5-100 nm for SAXS, ~0.3-5 nm for WAXS), and is capable of probing the morphologies of very thin < 10 nm ionomer films in a catalyst layer, and is an effective technique to image this as a function of relative humidity. The ‘grazing incidence’ is used to minimize the impact of substrate on the resultant data. GISAXS data is very difficult to interpret; a common interpretation of the ‘ionomer peak’ found in this technique is the average spacing between water domains (e.g. proton-conducting channels in a PEMFC) and includes a measure of their orientation, morphological properties, and hydrophobicity, potentially providing a quantitative measure of nano-phase segregation in a given film including the confinement effects of ultra-thin films; as a word of caution, interpretations of GISAXS data and similar have been hotly debated for many years. The most compelling research is correlated with concurrent measurements such as atomic-force microscopy (AFM), transmission electron microscopy (TEM), or ellipsometry, to determine film stress/swelling and/or conductivity, or molecular dynamics simulations.[100,104,132,166,173–176]

2.3.3. Porosity gradient – Mercury Porosimetry vs. Gas Adsorption

Catalyst layers form pores from the nano- to macro-scale. This is known as the porosity gradient, which measured in terms of incremental volume or cumulative pore area vs. pore diameter, and can be found experimentally by Brunauer-Emmet-Teller (BET) porosimetry or mercury porosimetry.[iv] BET porosimetry relies on achieving a high vacuum over a catalyst layer and slowly feeding gas into the system and measuring pressure to a high degree of accuracy. Pores in the CL will fill from small to large, and the amount of adsorbed gas at a given pressure gives a measure of the total internal area of a given pore diameter. Mercury porosimetry relies not on preferential surface formation but on overcoming the repulsion of non-preferential surface formation. As a liquid metal at room temperature, mercury has a high surface energy (more than 6x that of water) and requires increasing pressure to wet smaller-diameter pores; resolving the internal area of < 10 nm diameter pores require greater than 100 bar pressure, so the accuracy to which these high pressures can be read leads to better resolution of the small microporous regime.

Both techniques have a theoretical minimum resolution between 2 and 6 nm, depending on the system (determined by the lowest and highest pressures the system can sustain, respectively), and maximum between 0.3 (BET) and 10 µm (Hg), although in both cases resolution suffers in the low-vacuum measurement regime that resolves the region above 0.1 µm pore diameter. BET instruments are more common but suffer from several additional disadvantages in the determination of catalyst layer porosities, including very long pump-down times, especially for hydrophilic materials, more complicated theory to correlate gas intrusion with surface area, and multiple options for gases (77K N_2 is the standard, but helium or other gases may be employed). The main drawback of mercury

---

[iv] Mercury porosimetry is sometimes called mercury intrusion porosimetry, MIP.

porosimetry is the rarity of the instruments resulting from the safety considerations involving the handling of mercury, incredibly disproportionate for the minimal hazard its use poses. High accuracy in high pressure / low pore diameter regime that resolves the ~15-50 nm pore diameter range is critical to the accurate determination of functional CL microstructure (see also Chapter 4).[110,119,167,177–182]

Chapter 3. Hydrocarbon Proton-Exchange Membrane Catalyst Layers with Alcohol-Soluble, Sulfonated Poly(arylene ether)s

*This chapter apart from the critical discussion has been published as peer-reviewed research.[183]

Strong, A.; Britton, B.; Edwards, D.; Peckham, T. J.; Lee, H.-F.; Huang, W. Y.; Holdcroft, S. J. Electrochem. Soc. 2015, 162 (6), F513–F518.

Individual contributions were:

AS: Experimental lead MEA characterization, initial draft

BB: Experimental second MEA characterization, data analysis, subsequent & final drafts

DE: Assistance in experimental aspects of MEA characterization

TJP: Detailed manuscript review

HFL: Synthetic work, *ex situ* membrane characterization & casting

WYH: Supervision of synthesis work

SH: Overall scientific supervision

3.1. Background

Perfluorosulfonic acid (PFSA) ionomers offer exceptional physical and chemical stability for proton exchange membrane fuel cells (PEMFCs) as well as high proton conductivity,[41] but are expensive, exhibit high gas permeability, and are of limited use at high temperature and low humidity.[5] Hence, attention has focused on the investigation of hydrocarbon-based solid polymer electrolytes for use as PEMs.[184] Compared to PFSA ionomers, there is a vast body of synthetic knowledge for material adaptation and a supply of potentially low-cost chemical inputs available for the synthesis of hydrocarbon-based analogues. However, while significant progress has been made studying hydrocarbon solid polymer electrolytes as membranes,[185] there is comparatively very little understanding of their incorporation as ionomer.[68] Studies on PFSA ionomer-based catalyst layers have revealed the highly complex nature of the interactions between ionomer, Pt, and the carbon support.[100,186] The aggregation of PFSA ionomer in catalyst inks and during the catalyst layer deposition process are believed to dramatically affect proton, gas and water transport through the catalyst layer (CL). A similar impact is expected for catalyst layers containing hydrocarbon-based ionomers. A previous report by Peron *et al.*, for example, demonstrated the influence of sulfonated poly(ether ether ketone) (sPEEK) loading in the CL.[187] In each case, sPEEK-based CLs were found to contain smaller aggregated catalyst particles and smaller pore sizes than their PFSA-based counterparts. In device testing, greater kinetic, Ohmic, and mass transport potential losses were found for all sPEEK-containing electrodes.[188] On the other hand, interfacial resistance between the PEM and CL was found to be lower.[36] Many alternative hydrocarbon ionomers have been studied and, while showing promise, have generally proved inferior in performance to PFSA ionomer-based fuel cells.[189–192]

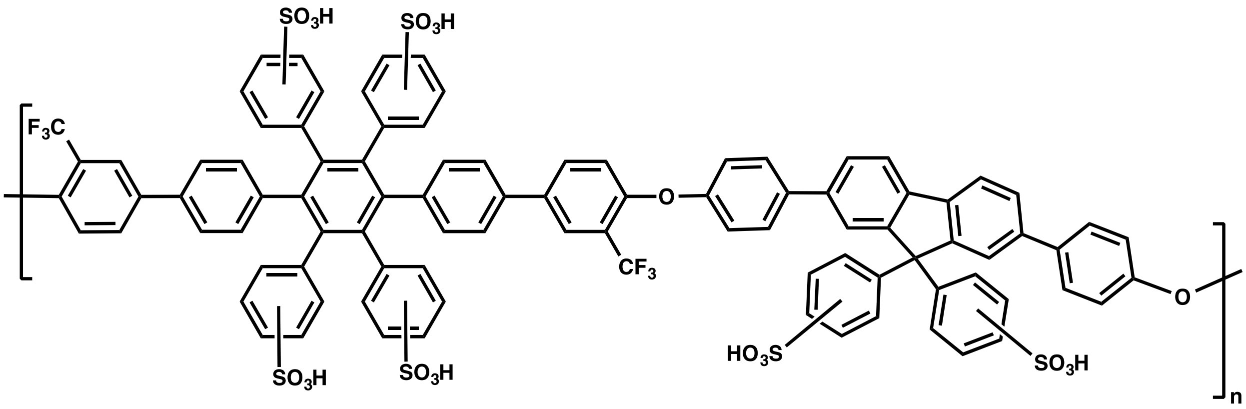

Figure 3.1: Structure of sulfonated P4c, showing potential sites for sulfonation.

In this work, sP4c (Fig. 3.1) is investigated as an ionomer in cathode catalyst layers. Membrane properties are also investigated to determine properties relevant to this study such as IEC, proton conductivity, and water sorption. sP4c is based on a backbone structure that offers numerous monomer permutations while offering desirable physical properties such as high thermal, mechanical, and chemical stability.[193] The number of accessible aryl sites for sulfonation provides a means by which the ion exchange capacity (IEC) can be tailored.[193,194] The presence of $-CF_3$ groups increases the stability of the polymer stability due to their positioning at and electronic protection of ether sites typically susceptible to radical degradation pathways.[195–197] The abundance of orthogonal aryl rings in this type of structure leads to a larger than usual polymer free volume[198] coupled to high internal pressure / cohesive energy density, which allows for water sorption without excessive swelling.[199,200] The presence of the fluorenyl moiety has been shown to induce phase separation and to promote proton conductivity while also restricting excessive swelling. [159,198,201–204] sP4c is of particularly interest because it is soluble in low boiling point, protic solvents (e.g., methanol, ethanol) that are commonly used for PSFA ionomer-based catalyst inks. This contrasts with typical hydrocarbon ionomers that are soluble only in high-boiling, aprotic solvents, such as N,N-dimethylformamide (DMF).[159,203–206] Improved ionomer solubility in the catalyst ink alters ionomer aggregate morphology and reduces domain size; this has recently been suggested to improve long-term CL durability.[205,206] The avoidance of high-boiling, aprotic solvents during catalyst layer deposition is viewed as a necessary requirement in fuel cell manufacture.[100,207,208] This work describes the first instance of incorporating sP4c into water/alcohol catalyst inks to form hydrocarbon PEMFC electrodes.

3.2. Experimental

3.2.1. Synthesis & Characterization

The synthesis and characterization of sP4c, membrane fabrication and membrane characterization performed by Dr. Hsu-Feng Lee are described in detail in the resulting publication.[183]

IEC	2.21 meq g^{-1}
Water uptake	61%
Water content (λ)	15
Proton conductivity (80 °C, 95% RH)	72 mS cm^{-1}

Table 3.1: Summary of sP4c membrane properties.

3.2.2. Catalyst Preparation

Catalyst inks (1% solids by weight, 1:1 v/v water/methanol) were prepared from commercial Pt/C (TKK TEC10E50E, 46.4 wt% Pt) and a dispersion of the ionomer (5.1

wt% ionomer in 1:1 v/v H_2O/MeOH). To the Pt/C, the necessary volume of water was added and stirred until the solids were thoroughly wetted. Methanol was added slowly and the resulting ink stirred for 15 minutes. To this dispersion, the ionomer solution was added drop-wise and the ink stirred for another 10 minutes before probe sonication for 30 minutes. Dynamic light scattering was performed on all catalyst inks produced to determine particle size distributions. All electrodes were applied to Nafion 211 membranes via spray coating, for which the deposition was 0.4 mg Pt/cm^2 over an area of 5 cm^2. Baseline cathodes with Nafion® were fabricated with 30 wt% Nafion D520, while cathodes with sP4c were prepared with 20, 30, and 40 wt% ionomer (IEC = 2.21 meq g^{-1}), denoted hereafter as sP4c-20, -30, and -40.

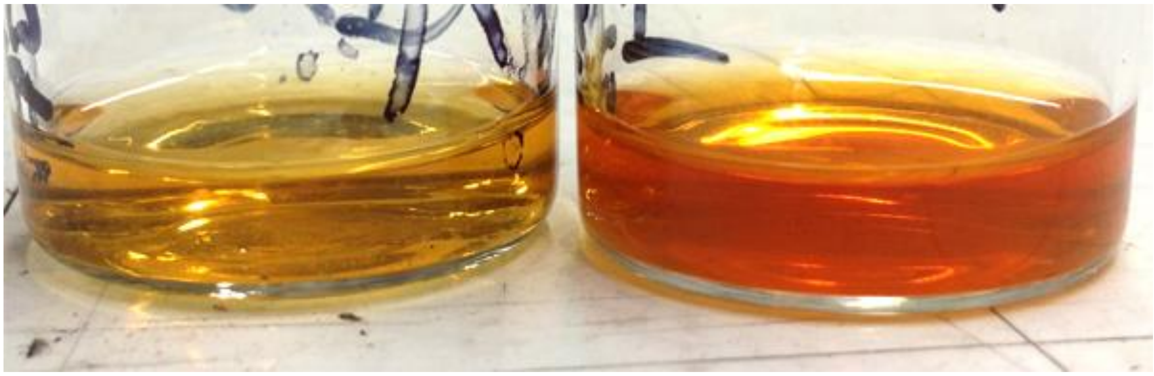

Figure 3.2: Solutions of sP4c(2.21) 5 wt% in MeOH for use in sP4c-20 (left) and sP4c-40 (right) electrodes.

3.2.3. Fuel Cell Operation & MEA Electrochemical Characterization

Cells were conditioned at 80°C and 100% RH with inlet gas flows of 0.5 slpm/1.0 slpm H_2/O_2 at the anode and cathode, respectively. MEAs containing Nafion D520 ionomer in the catalyst layers (CLs) were conditioned for 24 h, while those containing sP4c in the cathode CL required longer to equilibrate and were conditioned 36 h. Cells were held at a constant potential of 0.5 V for conditioning, then equilibrated to OCV before subsequent measurements. Polarization curves were measured from OCV to a shutoff potential of 0.3 V over 200 mA steps, measuring 5 min/point, with inlet gas flows of 0.5 slpm/1.0 slpm H_2/O_2 at the anode and cathode, respectively. Resolution of the kinetic region was achieved through potential sweep polarization curves with 0.025 V steps at 2 min/point. Cyclic voltammograms were measured at a temperature of 80 °C and 100% RH, with inlet gas flows of 0.25 slpm/0.5 slpm H_2/N_2 at the anode and cathode, respectively. Conditions were held until a stable potential of less than 0.15 V was attained, whereupon the gas flow at the cathode was set to zero. After holding at an initial potential of 0.4 V vs. RHE for 45 s, scans were cycled between potentials of 0.04 V and 0.90 V vs. RHE at 50 mV s^{-1}, 1 mV/pt. With inlet gas flows of 0.25 slpm/0.5 slpm H_2/N_2 at the anode and cathode, respectively, a Solartron 1287A FRA was used for EIS analysis. Holding the DC potential at 0.45 V vs. RHE, and with an AC voltage amplitude of 10 mV, frequency scans were performed from 20 kHz to 100 mHz. Protonic resistance through the CL was calculated using procedures detailed in earlier work by the Holdcroft group[53,209] and tortuosity was calculated using theory discussed by Havranek and Wippermann.[210]

3.3. Results and Discussion

3.3.1. Synthesis and Characterization of sP4c

Synthesis and characterization data for the series of sP4c(x) (where x = ion-exchange capacity, IEC) were as detailed above. The polymers were synthesized using standard literature routes to poly(arylene ether)s and sulfonated using solutions of chlorosulfonic acid to provide a range of acid-containing polymers with different IEC values. As observed from TEM imaging, the copolymers exhibit nanophase-separated structures analogous to those found for Nafion®.[211,212] The decision to use sP4c(2.21) as the ionomer in the CL was based on a combination of its solubility in low boiling point protic solvents (in this case, methanol) and its insolubility in hot water. These properties were related to a higher achievable molecular weight than the sP4c synthesized with an IEC of 1.89. sP4c(2.21) achieves a high proton conductivity (0.072 $S\cdot cm^{-1}$) at a relatively moderate water content (λ = 15 mol H_2O mol^{-1} $-SO_3H$), the latter important to prevent excessive swelling of the ionomer within the CL, which could potentially lead to mass transport losses at high current density during FC operation. NOTE: as only sP4c(2.21) was used in the subsequent studies detailed below, for simplicity it is hereafter referred to as sP4c.

3.3.2. Polymer Electrolyte Loading

Polarization curves at 80°C/100% RH under ambient pressure are shown in Fig. 3.3. For all sP4c-containing CLs analyzed, sP4c-20, sP4c-30, and sP4c-40, polarization (IV) performance is found to be lower than that of the baseline PFSA ionomer CLs, with the performances of sP4c-based CLs decreasing with corresponding increases in electrolyte loading. Large activation overpotentials are observed from EIS analyses for cells using cathodes based on sP4c, indicative of poor oxygen reduction kinetics. The poorer electrochemical kinetics of the sP4c-based CLs at low currents may be attributable to altered wetting of the Pt catalyst by the ionomer, poorer proton transport through the CL, or reduced oxygen transport through ionomer films.[187] Specific attribution of these losses may be probed by other *in-situ* and *ex-situ* methods.[213,214] The superior performance of the 20 wt% CL vs. those at 30% and 40% ionomer loadings is rationalized based on their relative porosities (*vide infra*). These findings indicate that a hydrocarbon CL of the same proton conductivity and void fraction as a PFSA CL would exhibit a slightly diminished relative FC performance.

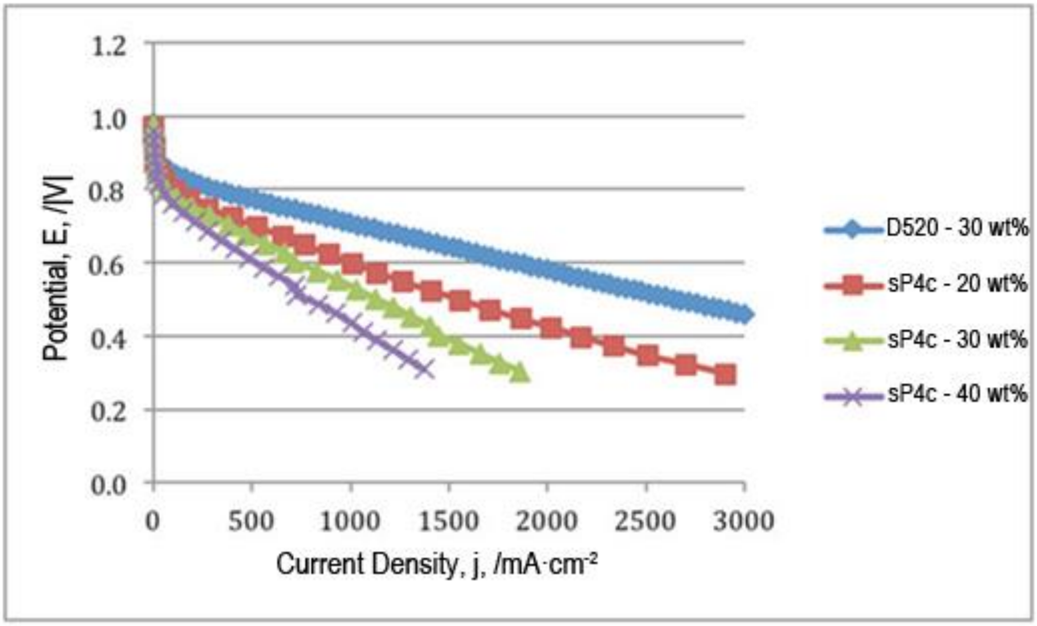
1.2
1.0
0.8
0.6
0.4
0.2
0.0
Potential, E, /[V]
0
500
1000
1500
2000
2500
3000
Current Density, j, /mA·cm⁻²
D520 - 30 wt%
sP4c - 20 wt%
sP4c - 30 wt%
sP4c - 40 wt%

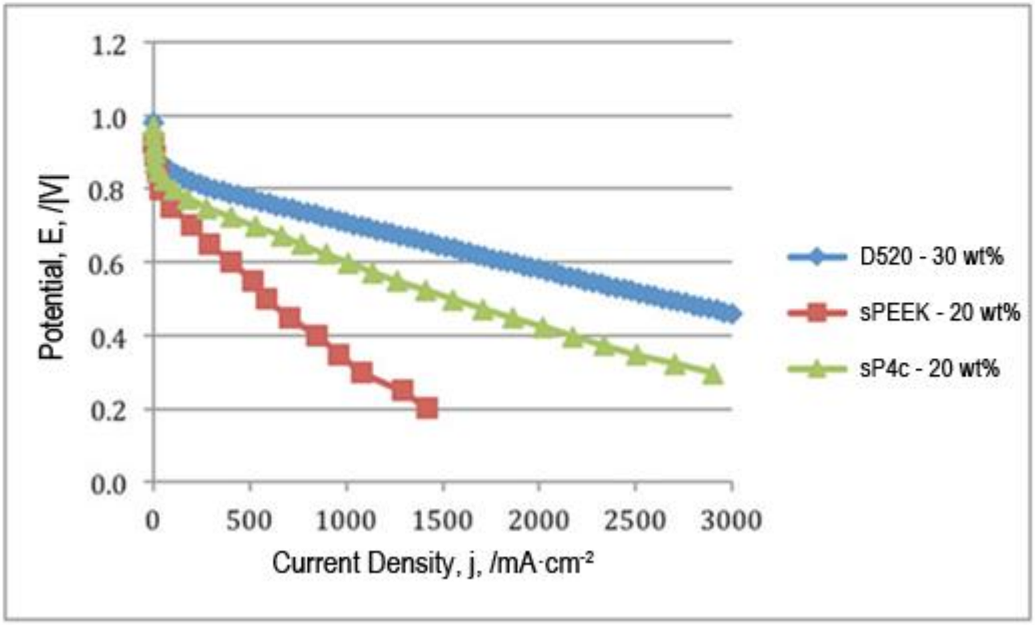
1.2
1.0
0.8
0.6
0.4
0.2
0.0
Potential, E, /[V]
0
500
1000
1500
2000
2500
3000
Current Density, j, /mA·cm⁻²
D520 - 30 wt%
sPEEK - 20 wt%
sP4c - 20 wt%

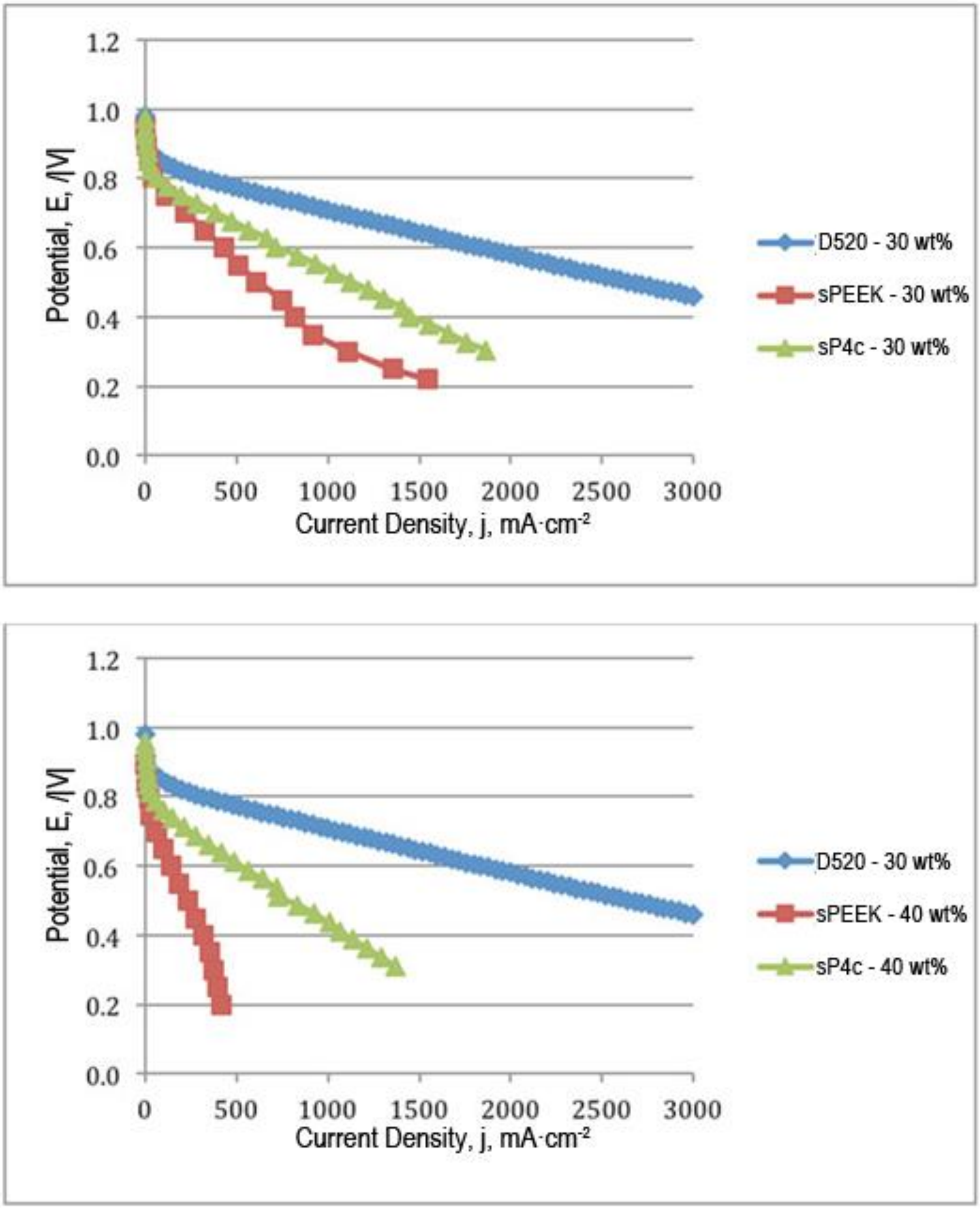

Figure 3.3: Polarization data comparing a D520-30 reference cathode with a) sP4c-20, sP4c-30, & sP4c-40 cathodes; b) sP4c-20 & sPEEK-20 cathodes c) sP4c-30 & sPEEK-30 cathodes; and d) sP4c-40 & sPEEK-40 cathodes, all with Nafion D520 anodes, on Nafion 211 membrane, all electrodes 0.4 mg Pt cm^{-2} loading. Operating conditions: 1.0 SLPM O_2, 0.5 SLPM H_2, 80°C, 100% RH.

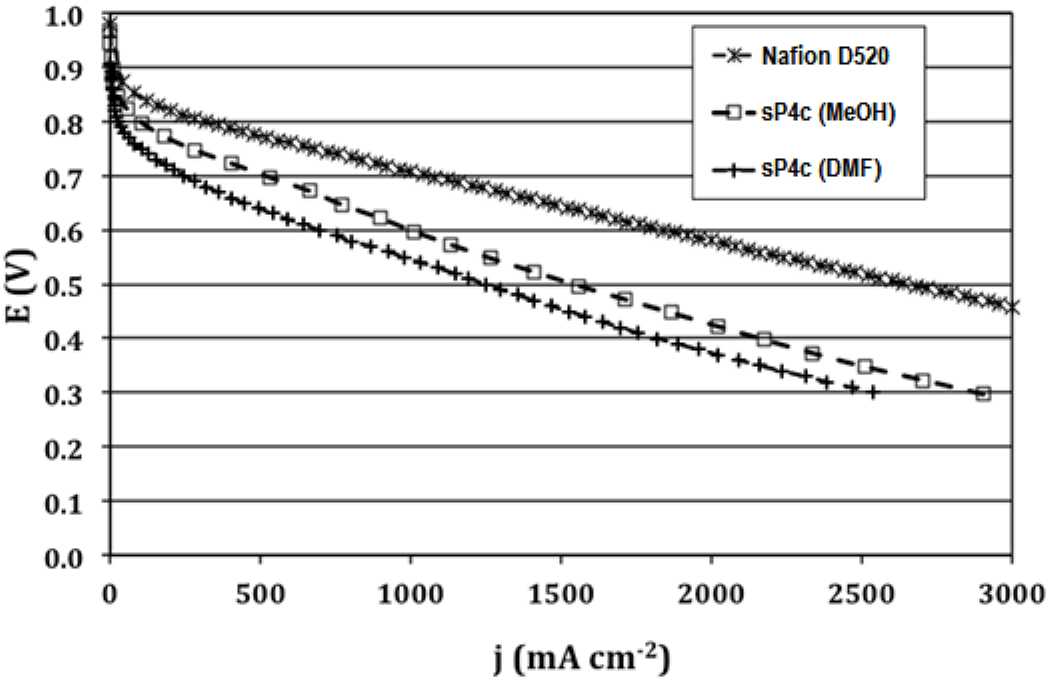

Figure 3.4: Fuel cell polarization curves for electrodes fabricated using standard methanol/water catalyst inks and those incorporating 0.4% DMF in catalyst ink (80°C, 100% RH, 0.5/1.0 slpm H_2/O_2). Membranes were Nafion 211 and a Pt loading of 0.4 mg cm^{-2} was common to all electrodes. All anodes and the cathode of the Nafion reference were 30 wt% Nafion D520 ionomer; cathodes of sP4c(MeOH) and sP4c(DMF) were 20 wt% sP4c.

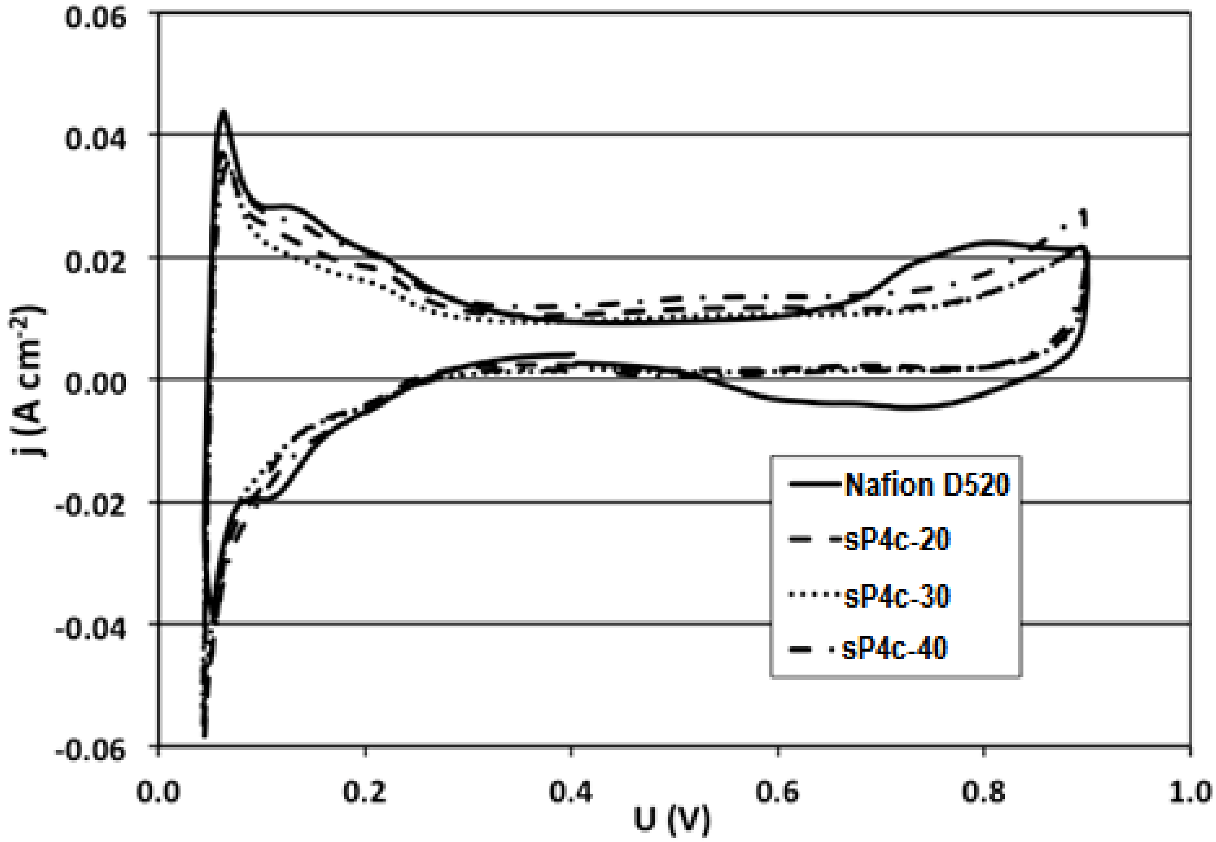

Figure 3.5: Cyclic voltammograms of electrodes for ink ionomer content study. sP4c-20, sP4c-30, sP4c-40, and D520-30 reference cathodes all incorporated D520-30 anodes and were deposited on Nafion 211 membrane, with all electrodes possessing a 0.4 mg Pt cm^{-2} loading; operating conditions were 80 °C/ 100% RH. 0.5 slpm H_2 / 0 slpm N_2, 50 mV/s scan rate.

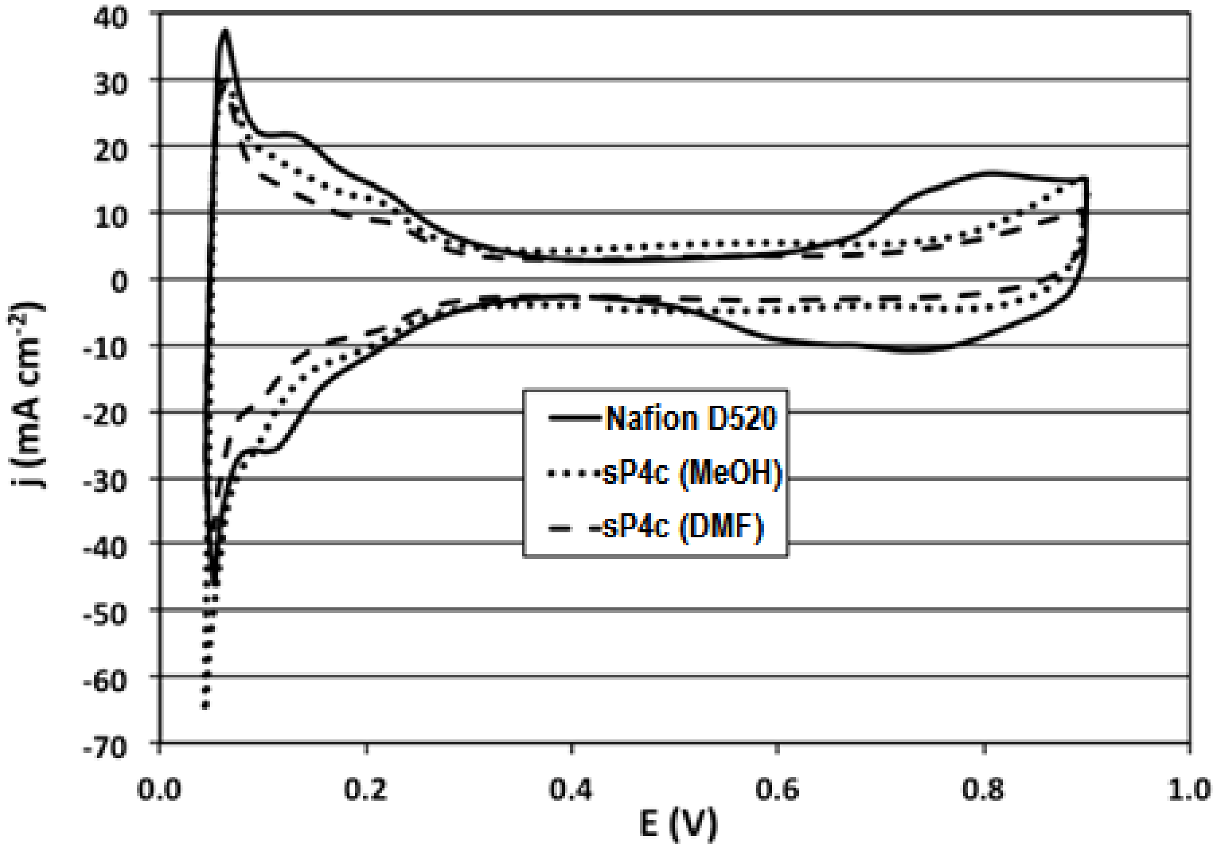

Figure 3.6: **Incorporation of DMF into catalyst inks resulted in an overall decrease in ECSA and C_{dl}.**

Cathode Ionomer	Ink Particle Size[a] (nm)	Cathode Thickness[b] (μm)	ECSA[c] (m^2 g^{-1})	Rp[d] (Ω cm^2)	σ_{H+}[e] (mS cm^{-1})	σ_{H+}[f] (mS cm^{-1})	% of bulk[g]	n[h]
D520	401	9.89	77 ± 2	0.086	11.6	60.4	40.2	1.1
sP4c-20	407	8.53	52 ± 1	0.359	2.4	10.9	15.2	2.4
sP4c-30	413	8.60	48 ± 3	0.090	9.5	25.8	35.8	1.9
sP4c-40	543	9.10	52 ± 1	0.355	2.6	4.7	6.5	7.2

[a] determined by light scattering
[b] determined by SEM
[c] determined from hydrogen adsorption charges of cyclic voltammograms
[d] cathodic proton resistance
[e] proton conductivity
[f] proton conductivity (normalized to ionomer volume in CL)
[g] % of normalized CL proton conductivity vs. bulk membrane proton conductivity
[h] tortuosity factor

Table 3.2: **Electrochemical surface area and proton conductivity for electrodes as related to ionomer content.**

Sample	Cathode Ionomer	Ionomer Loading[a]	Ionomer Dispersion[b]	Dispersion Composition[c]	Ink Particle Size (nm)[d]
D520	Nafion® D520	30	VOCs:H_2O:Ionomer	50:45:5	401
sP4c (MeOH)	sP4c	20	MeOH:Ionomer	95:5	407
sP4c (DMF)	sP4c	20	MeOH:DMF:Ionomer	85:10:5	409

[a] wt% loading of ionomer in dispersion
[b] solvent used for ink; MeOH for 1 or in the case of Nafion® D520, the dispersion contains primarily isopropanol but also other low bp alcohols
[c] composition of solvent (%wt)
[d] determined by light scattering

Table 3.3: Composition and properties of catalyst inks for DMF additive study.

Sample	HF Slope (unitless)	LF Slope (unitless)	R_p (Ω)	σ ($S\cdot cm^{-1}$)	$V_{ionomer,dry}$ % of V_{CL}	σ ($S\cdot cm^{-1}$), V normalized	tortuosity, n (unitless)
D520	1.599	11.976	0.086	0.0116	19.2%	0.0604	1.1
sP4c-20 (MeOH)	0.977	10.628	0.359	0.0024	21.8%	0.0109	2.4
sP4c-30	1.564	12.394	0.090	0.0095	37.0%	0.0258	1.9
sP4c-40	1.294	9.601	0.355	0.0026	54.4%	0.0047	7.2
sP4c-20 (DMF)	0.996	10.001	0.961	0.0013	44.8%	0.0041	3.6

Table 3.4: Proton conductivity data parameters from calculations. Slope taken from Nyquist plots of EIS data, Fig. 3.7 below.

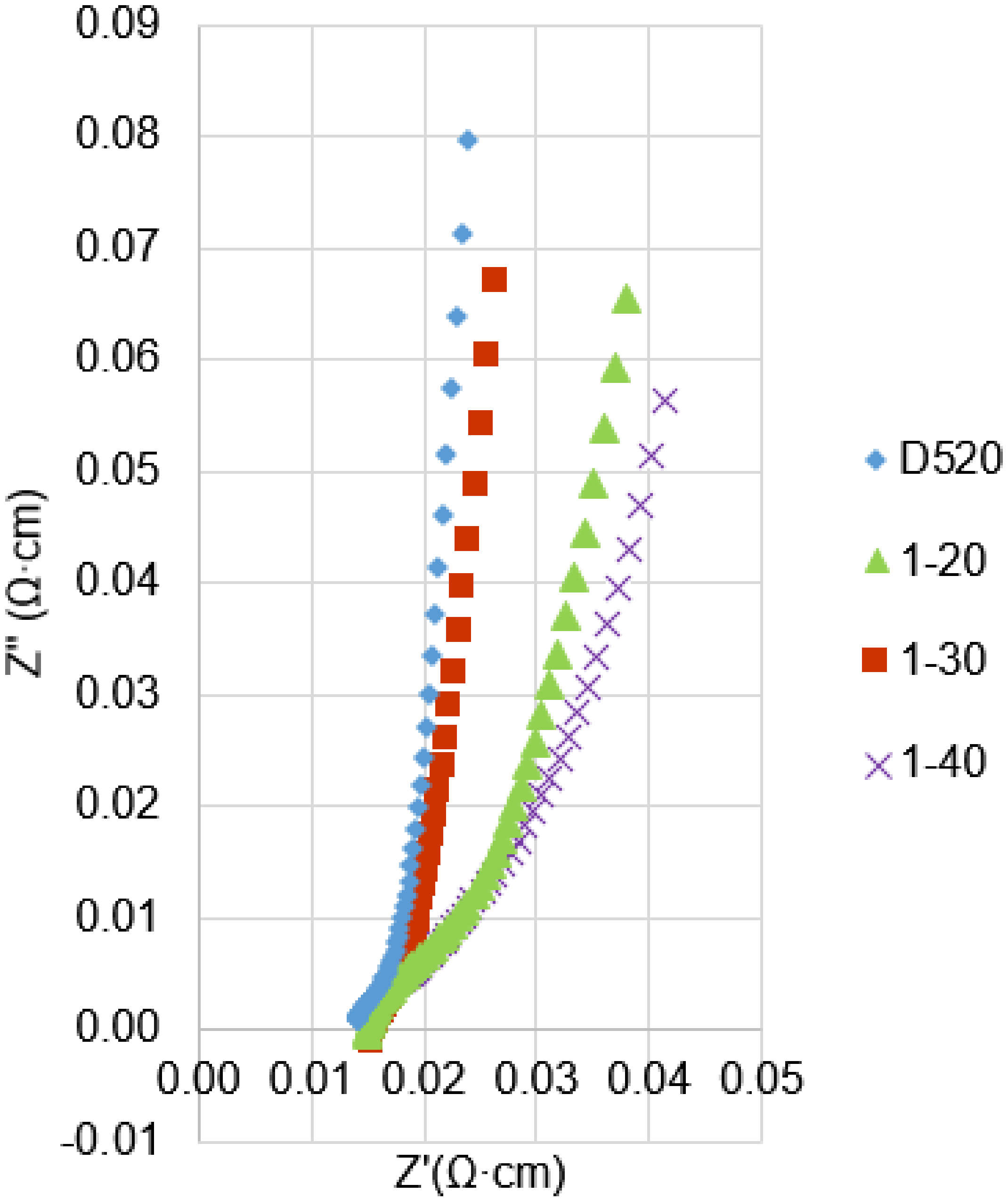

Figure 3.7: **Nyquist plot of EIS data, truncated to the relevant frequency range, 10-5000 Hz.**

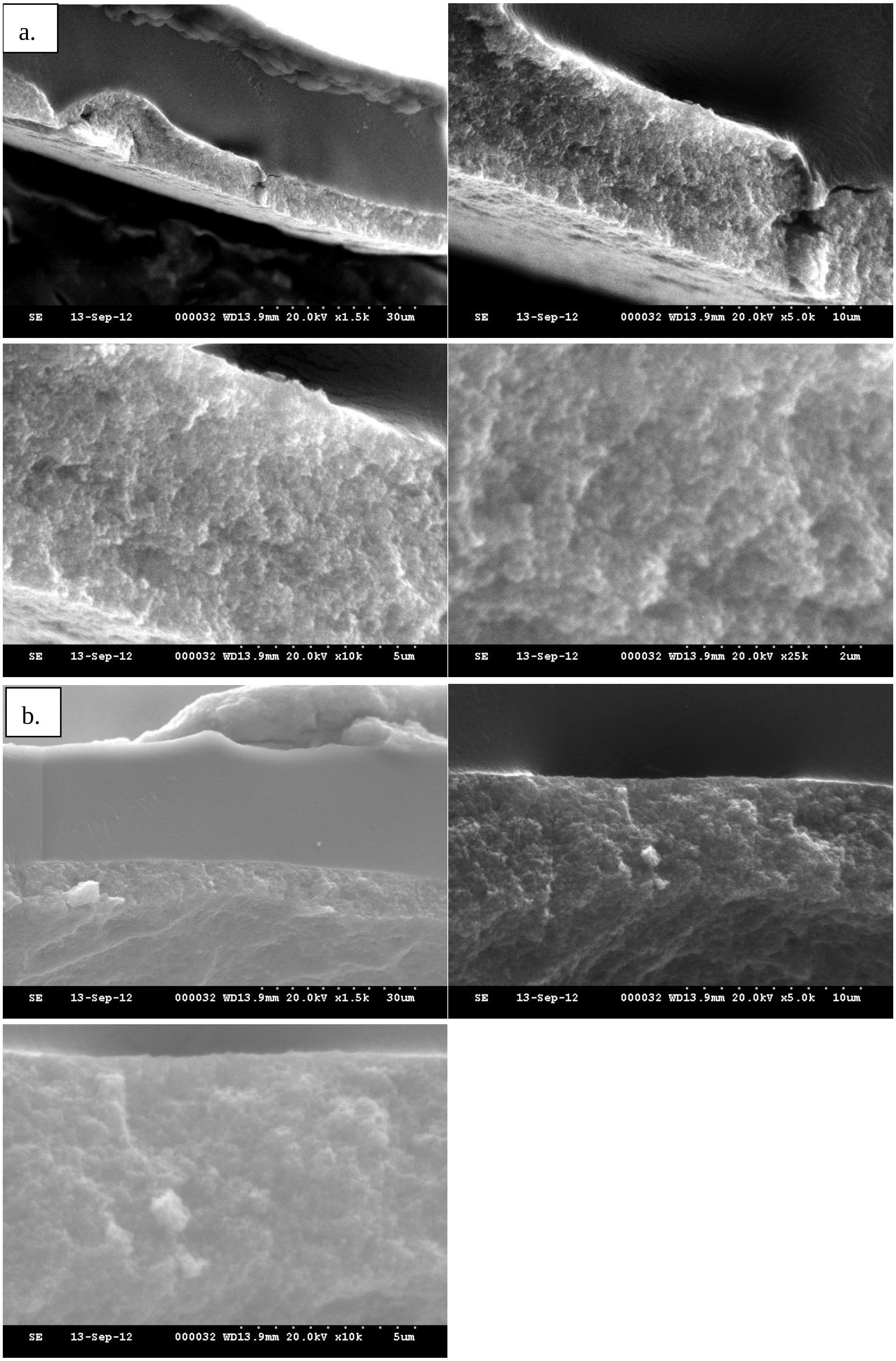
a.
SE 13-Sep-12 000032 WD13.9mm 20.0kV x1.5k 30um
SE 13-Sep-12 000032 WD13.9mm 20.0kV x5.0k 10um
SE 13-Sep-12 000032 WD13.9mm 20.0kV x10k 5um
SE 13-Sep-12 000032 WD13.9mm 20.0kV x25k 2um
b.
SE 13-Sep-12 000032 WD13.9mm 20.0kV x1.5k 30um
SE 13-Sep-12 000032 WD13.9mm 20.0kV x5.0k 10um
SE 13-Sep-12 000032 WD13.9mm 20.0kV x10k 5um

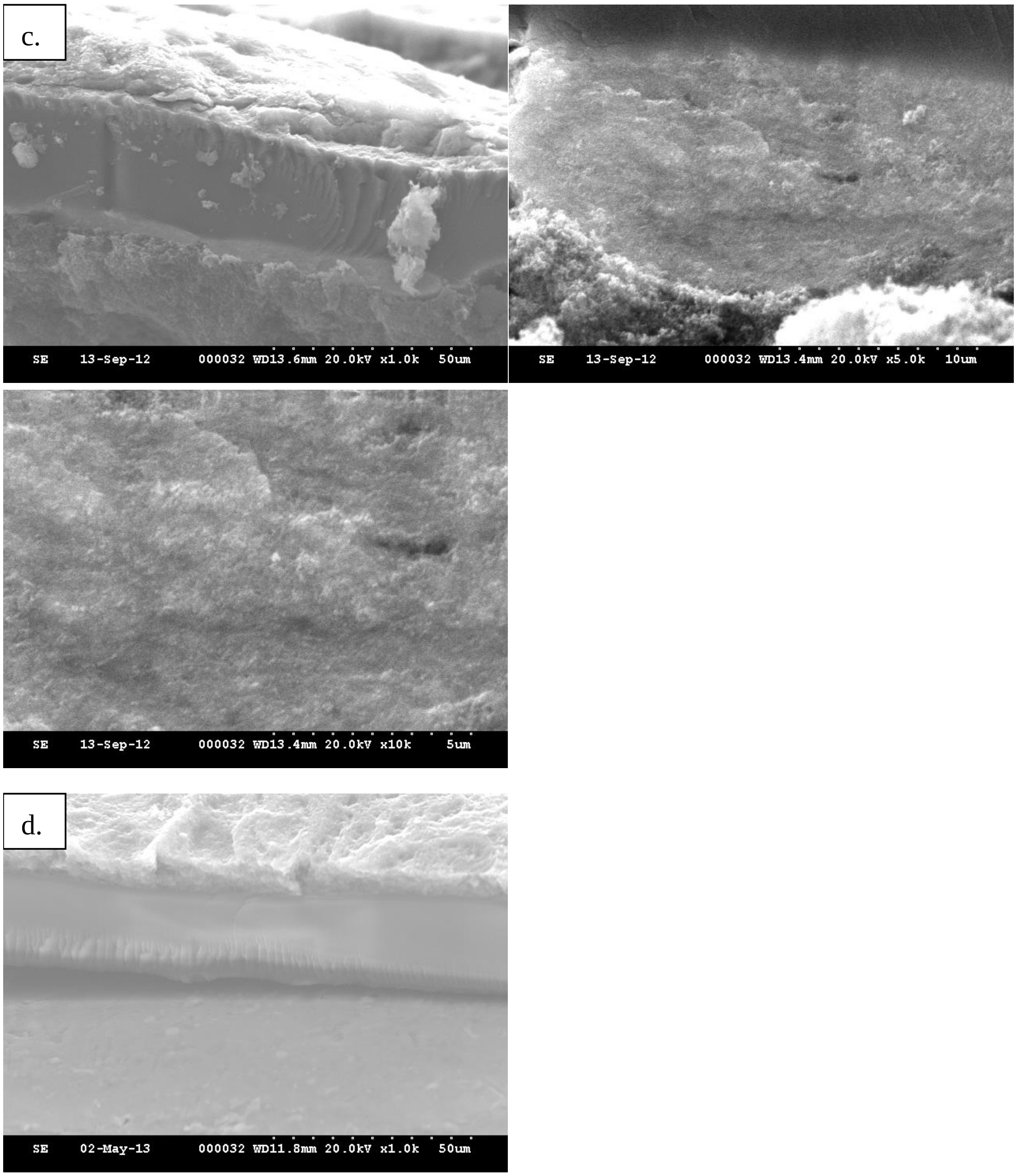

Figure 3.8: Cross-sectional SEMs of a.) sP4c-20 (MeOH), b.) sP4c-30, c.) sP4c-40 and d.) sP4c-20 (DMF), with zoom on cathode. Multiple sites were measured at 5-25 kx zoom to determine average CL thicknesses.

Electrochemical surface areas (ECSAs) of cathode catalyst layers were calculated from the hydrogen adsorption peak of cyclic voltammograms shown in Figs. 3.5 & 3.6. Consistent with literature reports of hydrocarbon ionomers,[68,207] the ECSA of CLs is observed to be lower for cathodes containing hydrocarbon ionomer. While measurements on PFSA ionomer-based CLs were found to agree with previous reports,[178] the ECSA of each MEA incorporating sP4c as the cathode ionomer was found to be approximately two thirds of PFSA ionomer value. The available area of Pt was found to be consistent for all sP4c samples, with averaged values of 52 ± 1, 48 ± 3, and 52 ± 1 m^2 g^{-1} for loadings of 20, 30, and 40 wt% of sP4c respectively, compared to the PFSA-based CL value of 77 ± 2 m^2 g^{-1}. However, the ECSA values are greater than for those previously reported for sPEEK-containing CLs.[209] Catalyst double layer capacitances were 167 ± 1, 156 ± 4 and 210 ± 1 mF cm^{-2} for 20, 30 and 40 wt% loadings of sP4c, respectively, whereas the corresponding PFSA ionomer CL was 121 ± 9 mF cm^{-2}. As double layer capacitance is generally observed to increase as a result of ionomer coverage of the catalyst, this appears to be consistent with the observed loss of accessible Pt sites for lower ionomer content-containing sP4c-based CLs.

The diminished ECSA of sP4c-based electrodes is indicative of lower Pt use, often considered to be a result of insufficient wetting of Pt particles. In general, a balance exists between poor catalyst wetting for low ionomer loadings and catalyst layer flooding for higher loadings; however, the consistent ECSA of the sP4c-containing cathodes examined suggests that an electrolyte loading of 20 wt% is sufficient to wet the catalyst. Beyond this threshold no additional Pt sites are activated by further incorporation of more ionomer; but rather, cell performance is diminished as a result of electrical isolation of the catalyst support and diminished pore volume.

Proton resistance of the cathode catalyst layer, R_p, decreases with ionomer loading from sP4c-20 to sP4c-30, and increases in sP4c-40. However, R_p is not normalized to CL thickness or ionomer content, and as a result is imperfect as a relative measure. To address these issues, proton conductivities were found, which account for individual CL thickness. Further, to address differences in ionomer volume in each CL, these were then volume-normalized using the densities of Nafion® and sP4c (1.95 and 1.16 g cm^{-3}, respectively). The resulting proton conductivities of the catalyst layer are 10.9, 25.8, and 4.7 mS cm^{-1} for loadings of 20, 30, and 40 wt%, respectively (Table 3.4). The PFSA-based CL exhibits a proton conductivity of 60.4 mS cm^{-1}. Comparison of the normalized proton conductivities to bulk values (150 and 72 mS cm^{-1} for Nafion® 211 and sP4c, respectively) shows an increase in proton conductivity from sP4c-20 to sP4c-30, indicating that increased ionomer creates greater connectivity between ionic pathways, consistent with literature. sP4c-30 has a similar proton conductivity loss in the CL versus bulk, 64%, as the D520 reference, 60%, an excellent result for hydrocarbon CLs, consistent with good coverage in the mesoporous regime of the CL and successful micro-phase separation therein. A significant decrease in conductivity was observed in sP4c-40, a result that appears inconsistent with increasing ionomer content but is consistent with prior *in situ* study of very high wt% CLs and the ability of low void volume CLs to function.[207] At high loadings, an increased fraction of ionomer may inhabit microporous regions wherein the ionomer layer is too thin to phase-separate adequately, preventing the formation of ion-conducting channels, and more enclosed or dead-end channels result. However, increased ionomer coupled with densification of the CL clearly indicates the low proton conductivity of sP4c-40 is a result of the ionomer's inability to fully hydrate. Calculated void fractions imply a negative void space were the ionomer to become fully hydrated in the 1-40 cathode (Fig. 3.9), clearly not the case for a CL that does not exhibit severe and immediate mass-transport losses *in situ* (Fig. 3.3a&d). Instead, the fairly rigid catalyst/support structure in the CL limited the ability of the ionomer to swell and fully hydrate, allowing the cathode to function *in situ* but at a decreased proton conductivity. By these comparisons, it is clear all results for sP4c-40 including polarization data effectively represent the cathode operating at a reduced relative humidity.

Void fractions of catalyst layers were calculated to consider mass transport limitations with respect to ionomer loading. Using SEM analyses of CL thicknesses, volumes were estimated for each sample and the void fraction calculated using the densities of each component and Equation 3.1.

$$V_{void} = 1 - V_C - V_{Pt} - V_{electrolyte} \tag{3.1}$$

Void fractions of fully hydrated CLs are also considered, with water uptakes of 23 and 61 wt% for PFSA and sP4c, respectively. It is shown in Fig. 3.9 that the resultant volume fractions of an electrode containing 20 wt% sP4c most closely resemble those of a standard, optimized PFSA-based CL, and that the total pore volume of a hydrated CL with the assumption of full hydration decreases to zero when the ionomer loading is increased from 20 to 40 wt%. This is in agreement with other studies of non-PFSA CLs in which electrodes are observed to densify as ionomer loading increase. As a result of densification of the CL, electrode porosity is lost and mass transport resistances increase at high current densities.

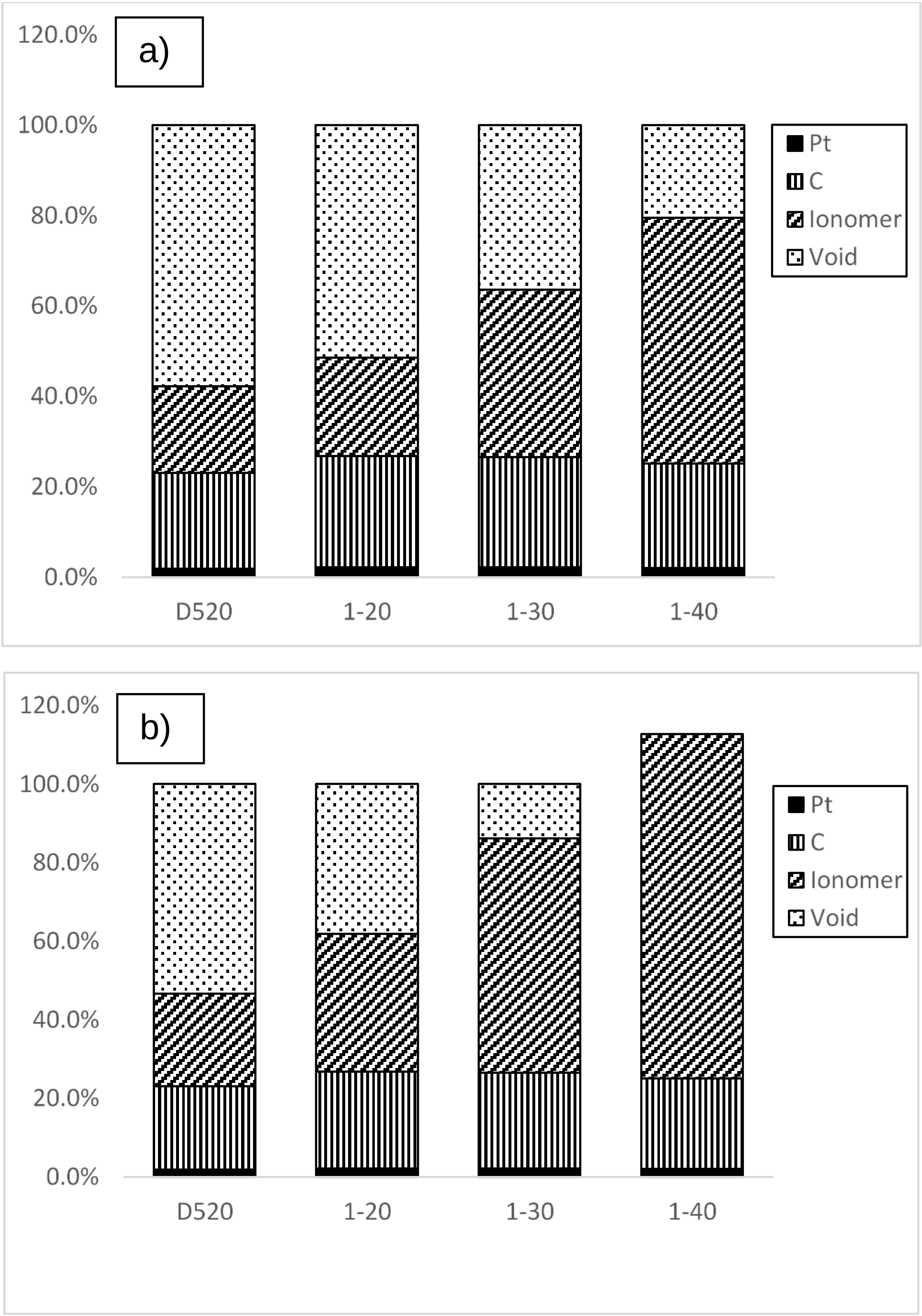

Figure 3.9: **Calculated electrode compositions in a) anhydrous; b) hydrated states for sP4c-based electrodes at 20, 30 and 40 wt% ionomer.**

wt% ionomer	Ink Particle Size (nm)	Cathode Thickness (µm)	V_{CL} (mm^3)	% V_{Pt}	% V_C	% $V_{ionomer}$ Dry	% $V_{ionomer}$ Hydrated	% V_{void} Dry	Water Uptake	% V_{void} Hydrated
D520-30	401	9.89	4.95	1.89	21.2	19.2	23.6	57.7	23	53.3
sP4c-20	407	8.53	4.27	2.19	24.6	21.8	35.1	51.4	61	38.1
sP4c-30	413	8.6	4.3	2.17	24.4	37	59.6	36.4	61	13.8
sP4c-40	543	9.1	4.55	2.05	23.1	54.4	87.6	20.4	61	-12.8
sP4c(DMF)	409	6.1	3.05	3.1	34.9	30.9	49.7	31.2	61	12.3

Table 3.5: Full data for electrode composition calculations using Eq. 2.1 (see Fig. 3.9 above)

The particle size of the catalyst ink was observed to increase with sP4c(2.21) loading, with 20 and 30 wt% sP4c-containing inks being of similar particle size to Nafion®-based inks. The cathode thickness was found to increase with particle size as a result of its influence on packing density upon spray-coating, in agreement with studies of PFSA ionomer-based CLs.[179] Variations in cathode thickness also lead to differences in the proportionalities of wt% ionomer and vol% ionomer in Tables 3.4 & 3.5. This observation however deviates from the general trend for CLs using hydrocarbon ionomers, for which electrode densification leads to a decrease in thickness as ionomer loading is increased. This deviation is rationalized as being due to the nature of the solvent system, as the fabrication of sP4c-containing electrodes reported here is free of the high-boiling solvents typically employed to dissolve hydrocarbon ionomers for catalyst ink formation. Although sP4c is insoluble in water, a solution of this ionomer dissolved in 50:50 water:methanol, appearing homogeneous and stable (Figure 3.2). The solubility of sP4c in methanol is likely a result of the polymer rigidity and high free volume allowing greater access to small solvent molecules between chains in polymer aggregates; greater accessibility to the hydrophilic regions in aggregated polymer chains enables polar, protic solvents better to disaggregate and disperse these polymer chains. This provides several advantages for fabrication: CLs may be fabricated with similar deposition procedures used for PFSA ionomer-based inks, allowing for direct comparisons: fuel cells can be prepared by spray coating membranes rather than gas diffusion layers, eliminating the need for hot-pressing; the removal of high-boiling solvents from the fabrication process allows for higher ECSAs and porosity; and alcohols are easier to handle and safer to use in large-scale processes.

A uniform distribution of sP4c is supported by the consistently high ECSA of the electrodes and relatively constant C_{dl}, indicating that contact between ionomer and Pt does not change significantly even as the cathode sP4c ionomer loading is doubled from 20 to 40 wt%. This suggests that the effectiveness of sP4c-containing electrodes to conduct ions, in the context of fuel cell operation, increases as void space fills with ionomer able to achieve full hydration, but beyond a certain threshold effectively adds to the cell resistance by decreasing porosity and simultaneously increasing mass transport limitations. This process significantly accelerates once the ionomer cannot reach full hydration, whereupon proton conductivity begins to decrease significantly. sPEEK ionomer cathodes, formed from high-boiling solvent inks, exhibit a sharp increase in ECSA and proton conductivity with increased loadings, thought to be due to high ionomer loadings being required to create an effective ionomer percolation network.[187] However, with high loadings of sPEEK comes an increase in kinetic and mass transport losses resulting in a significant diminution of fuel cell performance due to poor gas transport through the CL, paralleling the results achieved with sP4c in this study. The nature of the ink solvent therefore plays a key role in the properties of a catalyst. Introduction of high-boiling solvents such as DMSO, DMAc, and NMP into catalyst inks not only affects the porosity and ECSA through the evaporation rate of the ink, but also results in the formation of domains in which the ionomer is preferentially soluble, leading to densification of the material.[68]

3.3.3. Low vs. high boiling point solvent inks

The solubility of sP4c in both low- and high-boiling solvent inks allows for a direct comparison of the role of the solvent ink. The ink compositions listed in Table 3.3 were investigated for catalyst layer fabrication.

Polarization data at 80°C and 100% RH under ambient pressure H_2/O_2 are shown in Figs. 3.3 & 3.4. Activation losses of the sP4c(MeOH) cells were found be greater than that of Nafion-based electrodes. Performance of the sP4c-DMF cell was found to decrease relative to its MeOH counterparts, the potential at 2.0 A cm^{-2} representing a loss of 0.53

V. Electrodes based on sP4c show higher cell resistance than the Nafion® D520 reference, but this decreased when DMF was omitted from the ink solvents.

The ECSA of cathodes containing sP4c ionomer were calculated to be 52 $m^2 \cdot g^{-1}$ for the sP4c(MeOH) electrode, and 44 $m^2 \cdot g^{-1}$ for sP4c(DMF) electrodes, corresponding to an increase of 18% for the MeOH-based electrode. The double layer capacitance for the sP4c(MeOH) electrode was found to be similar to that of PFSA CLs. The ionic resistance of the catalyst layer is found to be lower for CLs prepared from MeOH, resulting in an increase in catalyst proton conductivity (Table 3.4). Cathodic proton conductivity was calculated to be 10.9 mS cm^{-1} for the sP4c(MeOH) electrode, and 4.1 $mS \cdot cm^{-1}$ for the sP4c(DMF) electrode.

For sP4c, the DMF-based electrode was 20.4% thinner than its MeOH-based counterpart. SEM analyses found the CL thickness to be 8.53 µm for the sP4c(MeOH) and 6.02 µm for the sP4c(DMF) electrodes. Calculations of total electrode pore volumes indicates a loss of porosity when fabricating with DMF (Fig. 3.9), consistent with literature reports of catalyst densification.[215]

While DMF accounted for merely 0.38 wt% of the catalyst ink, pronounced solvent effects were apparent even with such small amounts. The use of DMF in electrode fabrication resulted in reduction of catalyst ECSA, porosity, proton conductivity, and markedly increased kinetic losses resulting in an overall decrease to fuel cell performance. Solvent effects therefore cannot be considered negligible and may pose a serious hurdle in the development of high-performance hydrocarbon ionomers – a class of materials not typically processable without the use of high-boiling polar aprotic solvents.

3.4. Conclusion

Sulfonated copolymer sP4c (IEC = 2.21 meq g^{-1}) was studied for potential application as a PEMFC ionomer. The performance of catalyst layers fabricated using sP4c was found to be highest for ionomer loadings of 20 wt%, with decreasing polarization performance for increased loadings. The ECSA of catalyst layers was found to be consistent, implying that ionomer-catalyst interactions are not improved by further introduction of sP4c and that the ionomer is well distributed throughout. As ionic pathways are thought to be well-developed even at a loading of 20 wt%, further incorporation of ionomer, though it increases proton conductivity to a point, decreases the pore volume and hinders mass transport, ultimately limiting catalyst layer performance.

CLs fabricated from catalyst inks devoid of high boiling point, polar, aprotic solvent displayed improved fuel cell performance. The introduction of DMF into the catalyst ink, even in very small quantities, led to a dramatic effect on the catalyst layer structure, including an overall decrease in ECSA, proton conductivity, porosity, catalyst thickness, and attainable power density. The solvent system employed during fabrication of CLs containing hydrocarbon ionomers plays a critical role in the cell performance and future work should be devoted to designing hydrocarbon ionomers that can be dissolved in low boiling point solvents.

3.5. Critical Discussion

The observation that a miniscule 0.38 wt% DMF in the catalyst layer ink had such a considerable impact in the kinetic region (see Fig. 3.4) was a remarkable result, especially since the methodology employed was spray-deposition onto a heated substrate, by far the fastest-drying method of catalyst layer deposition. Also very consistently throughout the literature, maintaining a high void space in catalyst layers, in particular through low-swelling volume % ionomer in the hydrated form, is the critical parameter for catalyst layers with excellent transport properties, i.e. highly functional catalyst layers. Previous work by the Holdcroft group (e.g. Peron *et al*) has compellingly demonstrated that the formation of high mesoporosity CLs (i.e. void space in the 20-100 nm pore diameter range) free as possible from ionomer incursion due to ionomer swelling and/or high volume % is critical for mass transport allowing for high-activity catalytic sites.

An important outlier remains various groups connected to Los Alamos National Labs, which have long studied effect of glycerol addition to solvents as a means of increasing ionomer hydrophilicity and swelling,[216] studied its effects on PFSA ionomers in solution,[205] on bulk-cast PFSAs,[45] ionomer in PFSA catalyst layers,[217] and claimed more durable electrodes result despite lower initial efficiencies.[218] To date, this work has been confined to PFSAs and these impacts may not translate to already higher-swelling and more hydrophilic hydrocarbon ionomers, or in fully hydrocarbon systems with milder degradation species potentially offering increased electrode lifetimes.

The entire topic of the *ex situ* study of ultra-thin ionomer films emerged and expanded rapidly soon after the completion of this work, and remains a very important avenue of research in this field. The prevailing theory posits that the oxygen permeance of the ionomer thin film formed on the Pt/C agglomerate determines the mass transport characteristics of a system by becoming the lead oxygen transport resistance at high current densities or, more of interest to the field, high catalyst activities. The corollary to this theory is that this oxygen transport resistance forms a barrier to increasing electrocatalyst activities, and thereby reducing effective platinum content without efficiency penalties, in ionomer-bearing catalyst layers. Recent work has demonstrated that more homogeneously distributed ionomer may reduce these mass transport losses,[219] while other data (in this case from the same group) suggests the accessibility of electrocatalyst on the electrocatalyst support is the main limitation on the attainable activity of an electocatalytic site,[220] a conclusion reached in similar work some time ago.[53] The definitive answers presently sought will dictate future ionomer development, electrode compositions, and MEA constructions.

Chapter 4. Anion-Exchange Membrane Catalyst Layers – The Control and Effect of Pore Size Distribution in AEMFC Catalyst Layers

*This chapter apart from the critical discussion has been published as peer-reviewed research.[221]

Britton, B.; Holdcroft, S. *J. Electrochem. Soc.* **2016**, *163* (5), F353–F358.

Individual contributions were:

BB: Experimental work, data analysis, & manuscript

SH: Scientific supervision

4.1. Background

O_2/H_2 polymer electrolyte fuel cells rely on the electrochemical oxygen reduction reaction (ORR) and the hydrogen oxidation reaction (HOR). In proton-exchange membrane fuel cells (PEMFC), the reactions occur in an highly acidic environment and occur with the greatest activity on Pt electrocatalayst.[222] An alkaline environment opens the possibility of using stable and highly active non-noble catalysts,[222–224] but hydroxide-exchange membrane fuel cells (AEMFC) are less well-developed and the hydroxide ion diffuses more slowly than protons.[12] Nonetheless, comparable membrane conductivities have been shown.[225] Moreover, compared to liquid-based alkaline fuel cells, AEMFCs may confer a higher power density, may have the capacity to function with impurities in the fuel, and have the potential to operate in CO_2-containing air,[223] especially under high current load.[226] Additionally, as most AEM materials are fully hydrocarbon, they may display a lower fuel crossover compared to perfluorosulfonate-based ionomers.

A barrier to the development of AEMFC technology concerns the poor chemical stability and low ion conductivity of the hydroxide-conducting polymer under typical fuel cell conditions. The same issue applies even more to the ionomer in the catalyst layer, which experiences rapid variations in its hydration. In a typical anion-exchange ionomer, both the polymer backbone and functional groups are subject to hydroxide attack, e.g., via β-Hoffman elimination or direct nucleophilic displacement of the functional groups.[227,228]

Cleavage of the polymer backbone primarily affects the mechanical properties of the membrane, while loss of functional groups disproportionately reduces hydroxide transport. However, recent work has shed light on the promising molecular design principles for the enhancement of anion-conducting membrane materials.[31,229,230] The adoption of steric and electronic protection of cationic groups, in addition to membrane reinforcements, are beginning to address the primary pathways of membrane degradation.[227,231–235] Membranes possessing very high ion conductivity have recently been designed.[236] However, these strategies are very infrequently combined and characterized *in situ*.[237] Moreover, stabilized, doped, or grafted membrane materials are not amenable to serve as a soluble ionomer for use in the preparation of catalyst inks. Presently, only two commercial products (FuMA-Tech FAA-3 and Tokuyama AS-4) are available for the purpose of forming catalyst layers for AEMFCs, which has greatly hindered the study and advancement of catalyst coated membranes for AEMFCs.[84]

Developments in alkaline-based catalyst and ionomer materials are also hindered by difficulties in electrochemical characterization, including the collection of meaningful polarization data. For instance, consistent fuel cell data are much more difficult to achieve than PEMFCs because of a greater sensitivity to both dehydration and flooding. Both effects occur in different regions of the same polarization curve, and the addition of backpressure may significantly alter this behaviour.[95,238] Given the highly sensitive and parameter-heavy nature of characterizing materials as MEAs *in situ*, the lack of rigorous *ex situ* characterization hinders discernment and comparison of emerging anion-exchange materials.[95] Electrochemical characterization of materials is also hampered by the added complexities of an alkaline environment, including a high sensitivity to impurity ions both adsorbed and in the Helmholtz-layer around active catalyst sites,[28,239] significantly higher polarization losses at the anode,[240] and instability of the vast majority of AEMs under conditions relevant to fuel cell function. Standardized best practices for the study and characterization of new AEM materials are only beginning to address these issues.[241]

The development of high-performance catalyst layers (CLs) for anion-exchange membrane fuel cells (AEMFC) is of particular relevance due to the disproportionate *in situ* losses that can be attributed to it. The formation of salt-like precipitates in the CL (the primary mode of degradation in AFC CLs), can be mitigated by *ex-situ* conditioning in AEMFCs,[242,243] but incomplete hydration throughout the electrodes during operation renders the ionomer vulnerable to the aforementioned chemical degradation pathways. In addition, the lower conductivity of hydroxide-containing ionomers means that researchers are relying on higher ion-exchange capacity materials: but this is a strategy with diminished returns given the excessive degrees of swelling often observed.[244]

The formation of catalyst layers using catalyst inks formed from low-dielectric, low-boiling solvents has been reported to affect catalyst layer morphology in CCMs investigated for AEMFCs.[182] These observations parallel findings for CCMs prepared for PEMFCs.[100] Whereas the effect of using high-boiling point solvents has been shown to cause significant performance losses in PEMFCs,[183] it has not been reported for AEMFCs. This is likely because hydroxide-based ionomers are currently only soluble in high-boiling solvents, with a few recent exceptions.[206] Additionally, whereas the investigation of techniques for fabricating membrane-electrode-assemblies for PEMFCs have been thoroughly reported, e.g., spray-coating, decal transfer, ink jet printing, hot-pressing, etc., and solvent effects have been shown to increase relevant regions of the pore size distribution of PEMFC catalyst layers, and thus fuel cell performances,[245] a similar strategy has not yet been reported for AEMFCs.

This study sought to gain better insight into alterations to catalyst layer structure and function that are caused by high-boiling solvents, particularly to the mesoporous regime, 20-100 nm pore diameters. High mesoporosity is critical for optimally balanced kinetic and mass transport parameters, enabling high-performance fuel cell operation. To achieve this, the ultrasonic spray-coating technique previously employed to create well-formed PEMFC CLs was adapted to AEMFCs, enabling the investigation of the effect of high-boiling solvents in catalyst layer formation. Specifically the resultant CCMs were characterized *in situ*, i.e. in operational AEMFCs, and *ex situ* using porosimetry and scanning electron microscopy. These results were contextualized with relevant electrochemical data, as in previous PEMFC studies by the Holdcroft group.[53,187] No true benchmark for AEMFC function has yet been established, but FAA-3 represents one of the few high-performance anion-exchange ionomers and unreinforced membranes commercially available, and is the subject to the most extensive parametric studies to date.[246] Consequently, these materials were chosen to undertake studies of structure-property relationships of catalyst layers.

4.2. Experimental

Catalyst inks were prepared containing a minimal percentage of high-boiling solvent in the following manner: MeOH/THF in a 1:1 wt/wt ratio was added to carbon supported platinum catalyst (TKK TEC10E50E, 44.6 wt% Pt on graphitized C) and stirred. Ionomer solution (FAA-3-Br, Fumion®, FuMA-Tech Inc., 10 wt% in NMP, b.p. 202 °C) was added dropwise. The resulting ink was stirred for 1 h and sonicated at low power for 1 h. The final ink composition was 48.1 wt% MeOH, 48.7 wt% THF, 2.2 wt% NMP, and 1.0 wt% solids. The solids were comprised of 75 wt% Pt/C and 25 wt% FAA-3-Br ionomer. A 1:1 wt/wt mixture of MeOH:THF possesses a dielectric constant (relative permittivity, ε_r) of 21 and an azeotropic boiling point of 62-64 °C,[247,248] while a 1:1 wt/wt mixure of MeOH:H_2O (typically used for PEMFC catalyst inks) has a dielectric constant of 57 and a zeotropic boiling point of 87 °C. [249,250]

AEMs used in this work were unreinforced FAA-3-Br, Fumapem® (FuMA-Tech Inc.) having a thickness of 20 µm in the dry form. AEMs were spray-coated with the catalyst ink on a heated vacuum table (Sono-Tek ExactaCoat SC®) to form cathode/anode catalyst loadings of 0.5/0.4 mg $\mathrm{Pt \cdot cm^{-2}}$. For the purpose of this work, catalyst layers were deposited using high head speeds (100 $\mathrm{mm \cdot s^{-1}}$) and low catalyst ink flow (0.25 $\mathrm{mL \cdot min^{-1}}$), forming the CLs in 200-250 layers, a significantly higher number of deposition layers than desirable for industrial-scale CL fabrication processes. Substrate temperatures were 50, 80, 120, or 150 °C. The time required to deposit an individual layer was 3 seconds, with the time between successive depositions of layer being controlled at either 5 or 30 seconds. CCMs were ordered **1**-**5** according to substrate temperature, and by time between successive depositions of layers (Table 4.2).

CCMs prepared using FAA-3-Br were equilibrated in 1M KOH overnight and briefly immersed in ultra-pure Millipore® water prior to mounting in the fuel cell hardware.[246] Exchange of FAA-3-Br to hydroxide form under these conditions was confirmed by weighing dried FAA-3 membrane before and after exchange (Table 4.1). Mounting in situ included a gas diffusion layer (GDL) (Sigracet® GDL 24BC, SGL Carbon SE) and gasketing (Teflon of thickness required give 20-30% GDL compression). Torque was applied to 2.26 N·m (20 in·lbs). Successful gasketing and GDL-electrode connectivity was determined by pressure-sensitive film (Prescale LLLW, Fujifilm). The fuel cell was connected to a Teledyne Medusa 50W test station (Scribner Inc.).

All CCMs were conditioned in situ under 0.5/0.25 slpm O_2/H_2 at 60 °C, 100% RH. Initial current density for conditioning was found by setting a 0.5 V potential. The current was stepped at 20 mA·cm^{-2}/step, 1 minute/step, to a potential 0.2V (this was method adapted from a previously published procedure).[246] After conditioning, the gas flow was increased to 1.0/0.5 slpm O_2/H_2. The open circuit voltage (OCV) was determined for 5 min, 10 s/pt. Multiple polarization curves were determined at 50 mA·cm^{-2} steps, 15 s/point or equivalent rates using smaller steps, e.g., to resolve the kinetic region. iR data was collected concurrently using the current-interrupt method. iR data from 500 mA/cm^2 to the high current density was averaged, corrected for cell resistance, and converted to membrane conductivity according to standard methods.[127] Multiple polarization curves were performed over 3-4 hours following conditioning, or until progressive performance losses were observed.

Additional electrochemical characterization was performed using a combined potentiostat and impedance/gain phase analyzer (VersaSTAT 4, PAR). AEMFCs were equilibrated under 0.25/0.5 slpm H_2/N_2 until stable, potentials < 0.15 V were achieved. Under these conditions, electrochemical impedance spectroscopy (EIS) was performed by applying a 0.45 V bias and 10 mV AC potential (10^6-0.1 Hz). Chronoamperometry (CA) was performed by increasing the bias from 0.0 to 0.6 V in 0.1 V steps at 30-second intervals. The average current density after current stabilization at 0.5 V was used to determine the fuel crossover current (mA·cm^{-2}). Gas flows were then altered to 0.25/0 slpm H_2/N_2 and cyclic voltammetry (CV) performed: ECSA was determined by the integration of the hydrogen desorption peak of all overlapping CVs, corrected for electrical crossover. The double-layer capacitance (C_{dl}) was found from the lowest difference between currents of equal potential ~0.4 V, uncorrected for fuel crossover, with all confidence intervals representing sample standard deviations.

CCMs were freeze-fractured in liquid N_2 to determine the membrane and catalyst layer thicknesses by SEM (Aspex Explorer). Each cathode thickness was taken as an average of six measurements across an entire cross-section. The electrode morphology was examined by SEM (FEI Dual-Beam 235). Mercury intrusion porosimetry was performed (Micromeritics Autopore IV 9500), with pressures at intervals 1-30,000 psi, on single 25 cm^2 electrodes spray-coated onto FAA-3 membranes to loadings of 0.5 mg Pt·cm^{-2} under identical conditions to each series. After correction for the electrode weight, both total internal porosity and pore distribution (between 10,000 to 6 nm pore diameter) were calculated. The swelling and water uptake of the hydroxide-form FAA-3 membrane were experimentally determined as an average of three samples exchanged from the bromide form into the hydroxide form by immersion in 1M KOH at room temperature for 24 hours, followed by heating to 60 °C for 1 hour. Masses and dimensions were measured immediately upon removal from solution and after drying in a 120 °C oven for 15 minutes.

4.3. *Results & Discussion*

4.3.1. Ex Situ Characterization of Catalyst Layers

Catalyst layers were formed on membranes by spray-coating multiple layers of the catalyst ink with the ionomer being in the bromide form. All CCMs appeared to dry instantaneously upon deposition. Deposition of the catalyst layer produced visibly well-formed, wrinkle-free CCMs, with no physical differences observed between CCMs formed in 1-hour (**2**, **3**, & **5**) and those formed in 4-hours (**1** & **4**) (Tables 4.2 & 4.3). The initial membrane thickness was 20.0 µm in all instances. Membrane thickness increased to 23 ± 1 µm upon exchange to the hydroxide form. The water uptake of the hydroxide-form was 133 ± 3% (Table 4.1). Dimensional swelling was found to be 17 ± 1% (Table 4.1).

Macroscale SEM images of the CCMs (Fig. 4.1, top row) revealed large feature sizes for cathode CLs in CCMs **1**, **2**, **3**, and **5**. Significantly smaller feature sizes were determined for **4**. On the mesoporous scale (Fig. 4.1, middle row), only CCM **2** displayed a significant absence of porosity (i.e. very few mesopores were observed relative to other CCMs), while no significant differences in porosity were observed in the nanoporous regime (Fig. 4.1, bottom row). Cathode thicknesses and calculated void fractions in the dry and fully hydrated states are reported (Table 4.3, see Fig. 4.2).

The porosity of the CLs were determined as differential intrusion and cumulative pore area (Fig. 4.3). The total internal porosities and total pore areas were found for CCMs **1-5** (Table 4.3). Considering only the mesoporous (20-100 nm) regime, the internal porosities and cumulative pore areas were found (Table 4.3, Fig. 4.4).

4.3.2. In Situ, O_2/H_2 FC Operation

CCMs fully conditioned *in situ* in 1-2 hours. Polarization data were determined for all CCMs and are shown in Fig. 4.5a-c. The data were found to be highly reproducible over multiple polarization curves after conditioning was completed. *In situ* membrane conductivities, determined by averaged Ohmic-region iR data from polarization curves (Eq. 4) and confirmed by EIS HFR, were estimated to be 15.3 ± 0.1, 21.3 ± 0.3, 22.9 ± 0.1, 28.8 ± 0.5, and 27.8 ± 0.5 mS·cm^{-1} for CCMs (Fig. 4.6), which is consistent with the reported hydroxide-form conductivity of 50 mS·cm^{-1} (Table 4.1). OCVs, kinetic-region and Ohmic regime voltages at 20 and 500 mA·cm^{-2}, respectively, and resultant maximum power densities are all reported (Table 4.3). Enhancements in AEMFC performance appear to correlate to the temperature of the substrate used to prepare the CCM prepared over a period of 1-hour, i.e. CCMs **2**, **3**, and **5** (Fig 4.5a) and for CCMs prepared over a 4-hour period, i.e. CCMs **1** and **4** (Fig. 4.5b). CCM preparation time had a greater effect than substrate temperature, comparing 4-hour CCM **4** and 1-hour CCM **3**, both prepared at 120 °C (Fig. 4.5c).

Conductivity for 20 µm hydroxide-form FAA-3 (mS/cm)*	50	
Reported water uptake 25 °C (%)	156	
Reported dimensional swelling 25 °C (%)	24-26	
Observed water uptake 60 °C (%)	133 ± 3	
Observed dimensional swelling 60 °C (%)	17 ± 1	
Form	Br^-	OH^-
IEC (meq·g^{-1})	2.4	2.8
Mass % Anion of Polymer (%)	19.2	4.1
Theoretical Mass Loss (%)	15.1	
Observed Mass Loss (%)**	19.9 ± 0.6	

*FAA-3 technical specifications, FuMA-Tech GmbH

**Average of 3 dried membrane samples exchanged from Br^- to OH^- form

Table 4.1: IEC, conductivity, water uptake, & swelling for FAA-3 at 25 & 60 °C.

CCM	Substrate Temperature (°C)	Wait Time[a] (s)	Cathode Deposition Time (min)	Anode Deposition Time (min)	Total time (h)
1	50	30	138	110	4.1
2	80	5	33	27	1.0
3	120	5	33	27	1.0
4	120	30	138	110	4.1
5	150	5	33	27	1.0

[a] Wait time between depositions of successive layers of catalyst ink. Each layer required approximately 3 seconds to deposit.

Table 4.2: Spray-coater substrate temperatures & deposition rates for all CCMs.

CCM	**1**	**2**	**3**	**4**	**5**
Thickness (µm)	7.6 ± 1.0	7.4 ± 0.6	11.1 ± 1.0	11.8 ± 0.5	11.5 ± 0.6
Void Fraction, Dry (%)	37	24	58	69	56
Void Fraction, Wet (%)	0	0	25	44	21
Total Internal Porosity ($cm^3 \cdot g^{-1}$)	0.687	0.674	0.795	0.767	0.976
Porosity 20-100 µm ($cm^3 \cdot g^{-1}$)	0.096	0.037	0.168	0.282	0.216
Total Pore Area ($m^2 \cdot g^{-1}$)	95.3	97.7	88.0	77.8	134.4
Pore Area 20-100 µm ($m^2 \cdot g^{-1}$)	8.8	4.3	14.7	21.6	17.1
OCV (V)	1.064	1.040	1.026	1.012	1.050
Potential at 20 $mA \cdot cm^{-2}$ (V)	0.924	0.952	0.921	0.900	0.945
Potential at 500 $mA \cdot cm^{-2}$ (V)	0.527	0.42	0.555	0.615	0.599
Max. Power Density ($mW \cdot cm^{-2}$)	276	224	313	428	326

Table 4.3: Catalyst thickness determined by SEM, void fraction by calculation (see Fig. 4.2), porosity and pore areas by mercury porosimetry, and *in situ* performances extracted from polarization data (see Fig. 4.5).

CCM	ECSA (m^2/g Pt)	Gravimetric Capacitance (mF/g Pt)	C_{dl} (mF/cm^2 Pt)	Fuel crossover current (mA/cm^2)
1	26.9±0.9	219	0.59	0.3
2	31.2±0.6	352	1.10	2.9
3	34.4±0.1	417	1.44	0.5
4	27.4±0.1	235	0.64	1.3
5	30.2±0.2	392	1.18	0.6

Table 4.4: Electrochemical data: ESCA and C_{dl} extracted from CV analysis, fuel crossover and short circuit from CA analysis, all but C_{dl} confirmed by LSV.

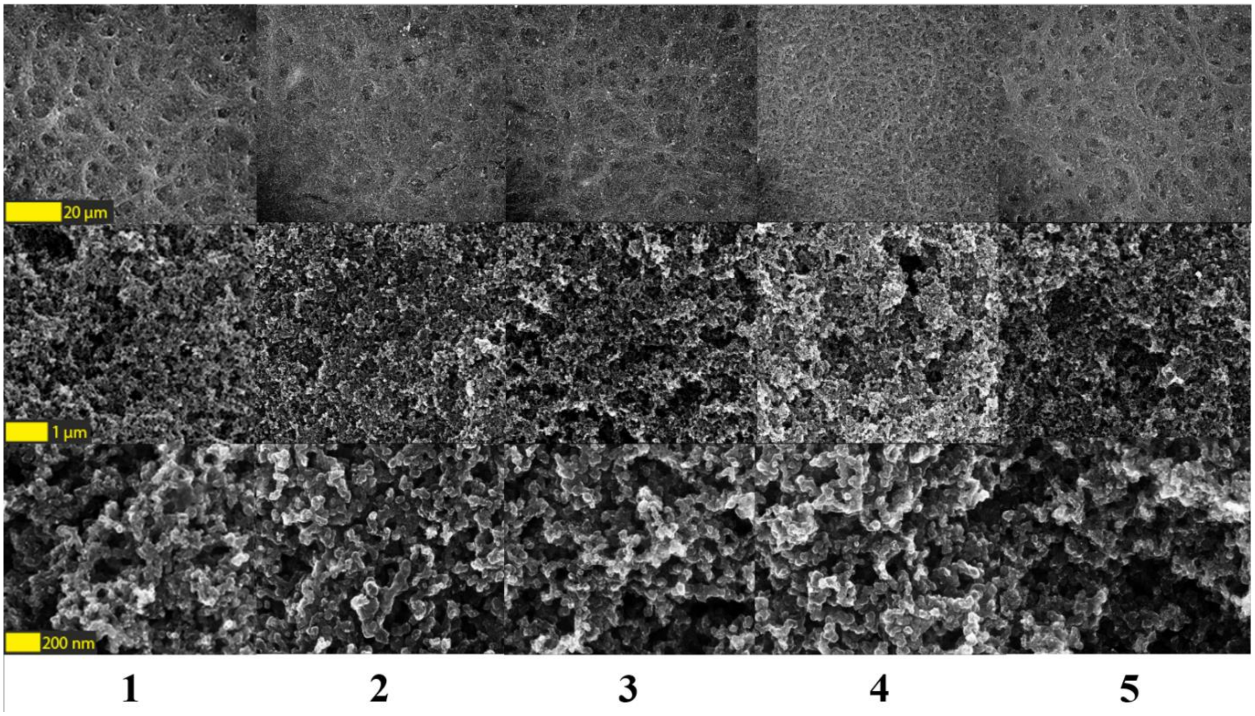

Figure 4.1: SEM images of cathode CLs for CCMs 1-5. Top, Middle and Bottom rows represent enlargements of 1.6 kx, 25 kx, and 100 kx. Scale bars are 20 µm, 1 µm, and 200 nm, respectively. See Table 4.1 for a description of the deposition protocol.

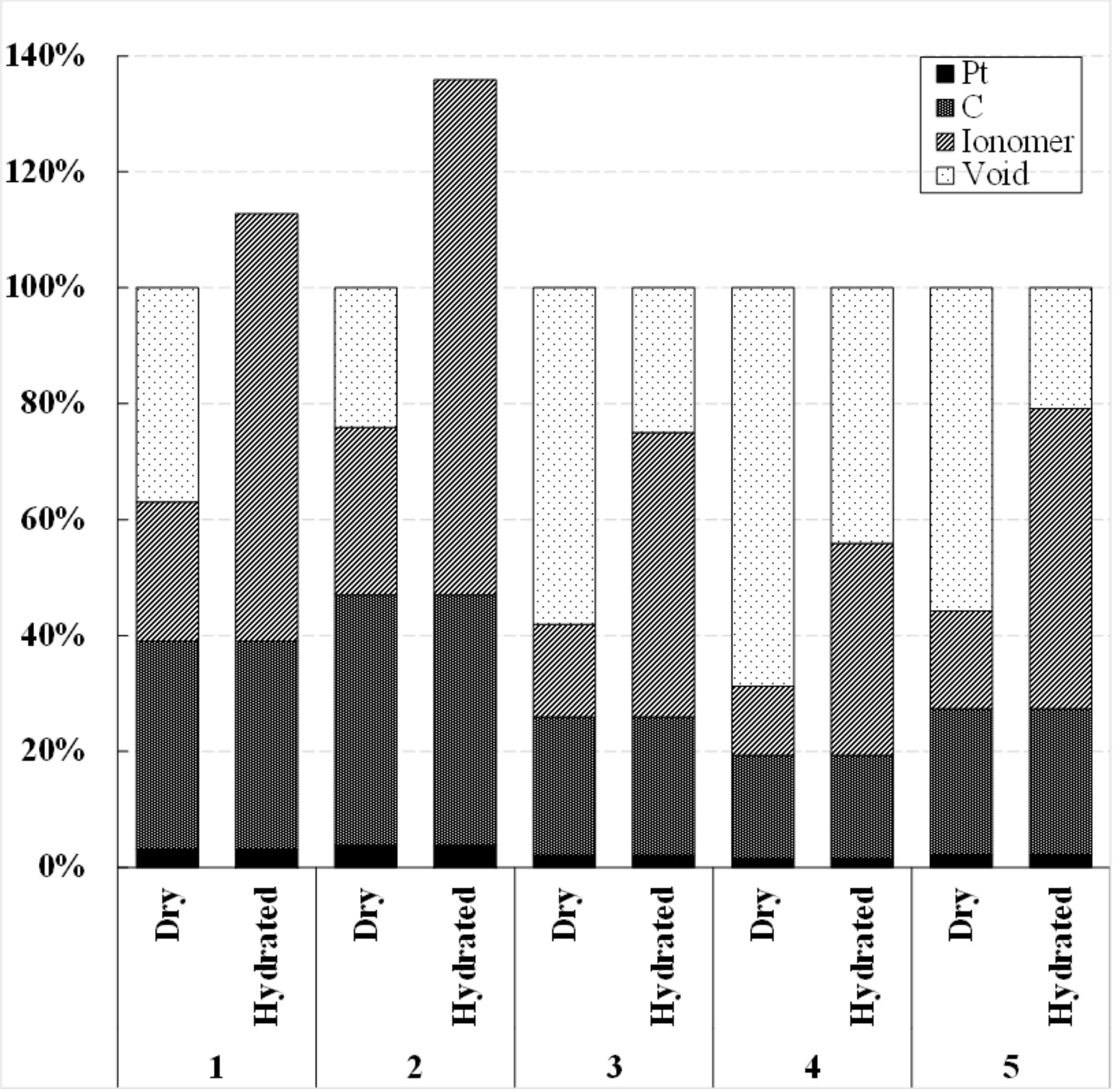

Figure 4.2: Electrode compositions as fractions of total volume for CCMs 1-5 in the dry and hydrated states, based on cathode thicknesses, electrode composition, and FAA-3 ionomer hydroxide-form swelling at 60 °C.

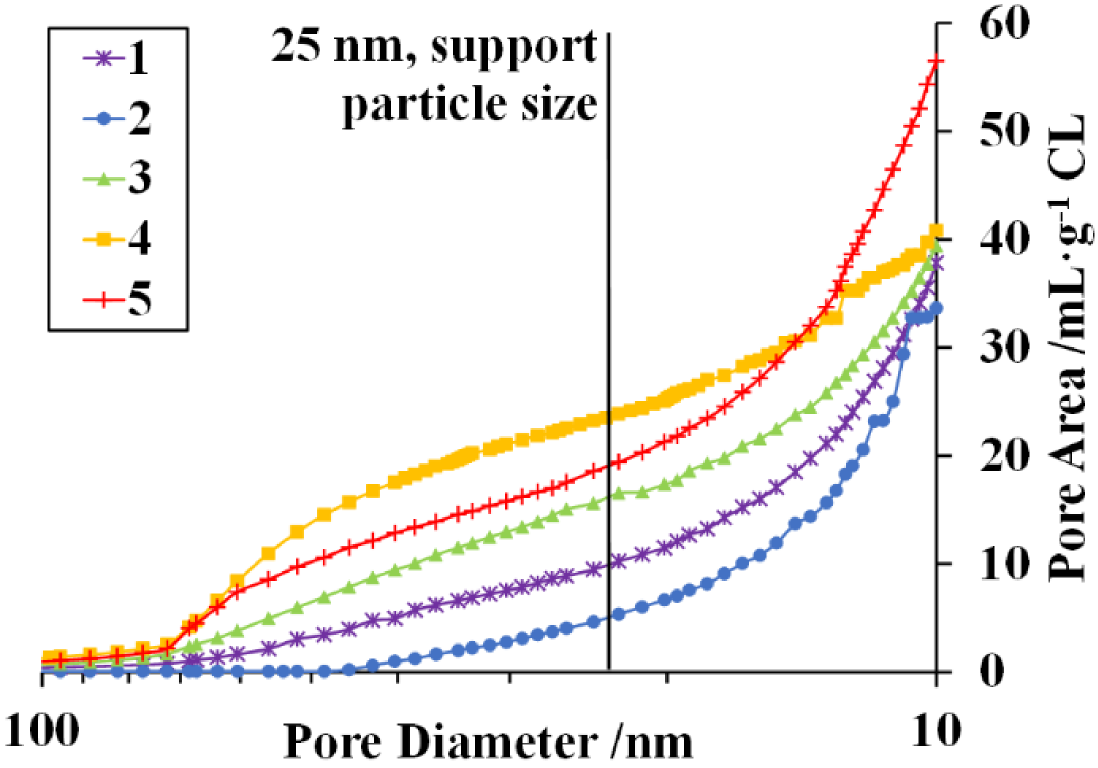

Figure 4.3: Cumulative pore area by mercury porosimetry from the mesoporous to the nanoporous regimes for CCMs 1-5.

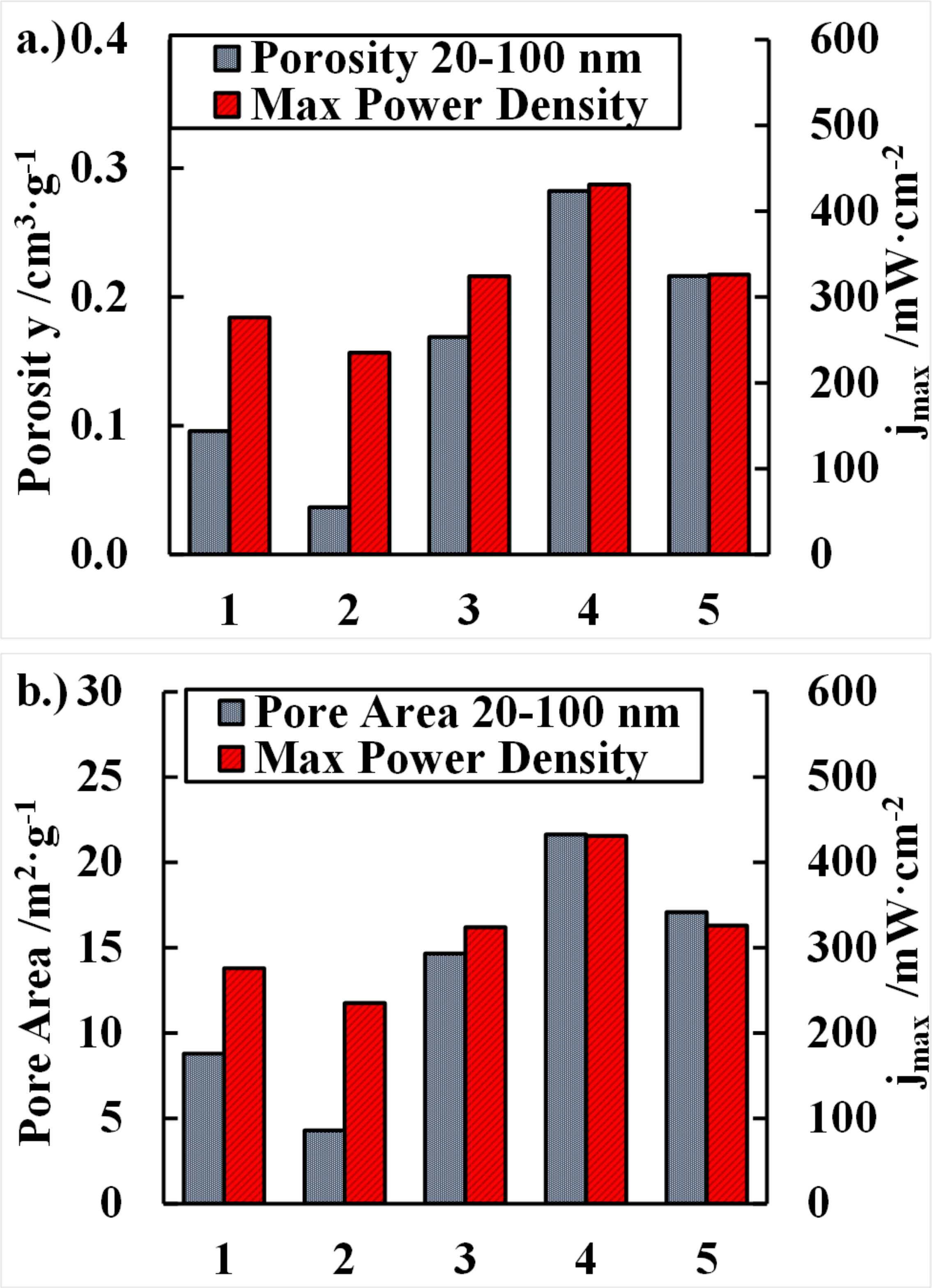

Figure 4.4: Power densities measured from polarization data (Fig 4.5) compared with: (a) mesoporous internal volume, (b) mesoporous pore area.

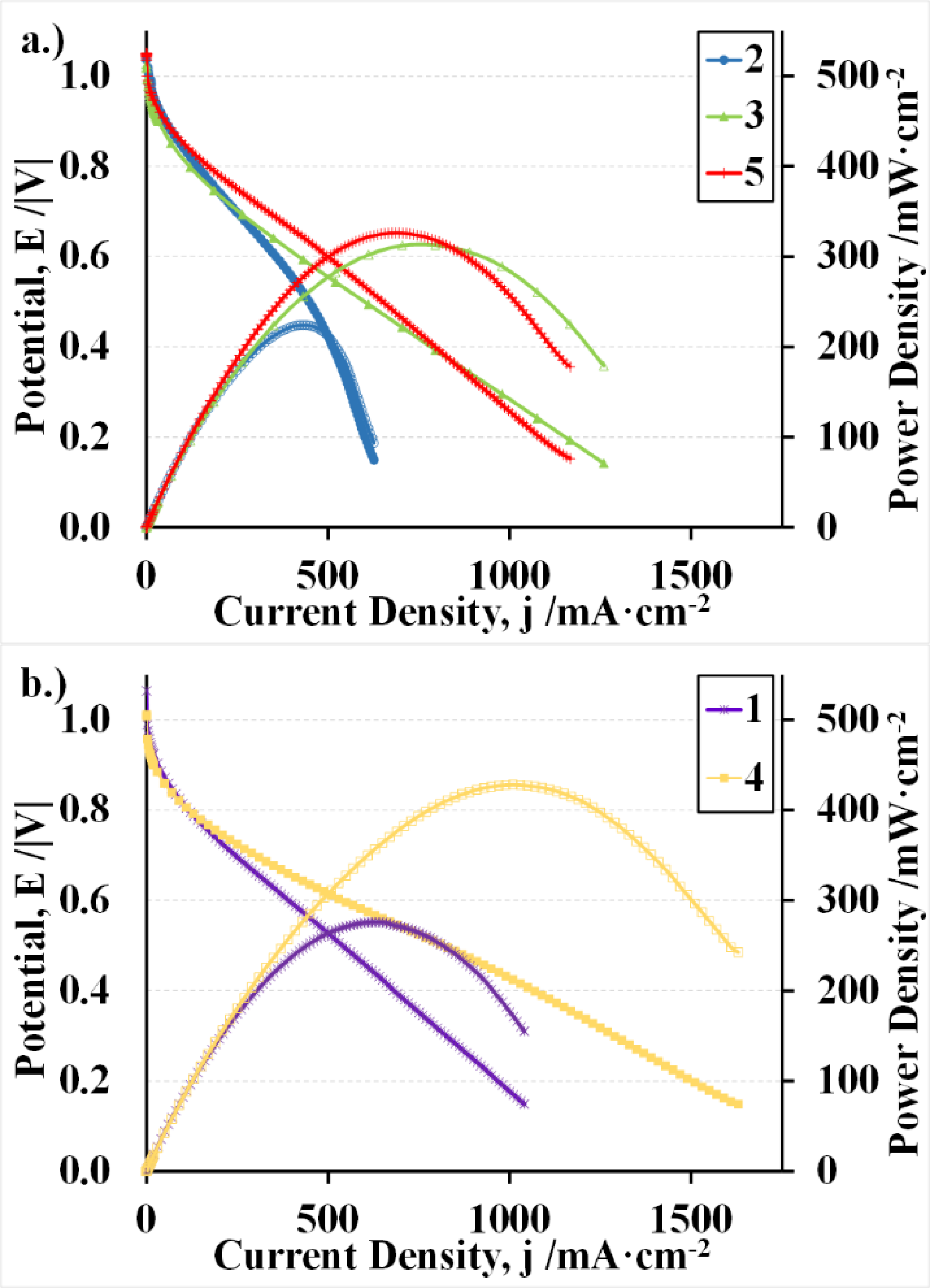
a.)
Potential, E /|V|
1.0
0.8
0.6
0.4
0.2
0.0
0
500
1000
1500
Current Density, j /mA·cm-2
Power Density /mW·cm-2
500
400
300
200
100
0
2
3
5
b.)
Potential, E /|V|
1.0
0.8
0.6
0.4
0.2
0.0
0
500
1000
1500
Current Density, j /mA·cm-2
Power Density /mW·cm-2
500
400
300
200
100
0
1
4

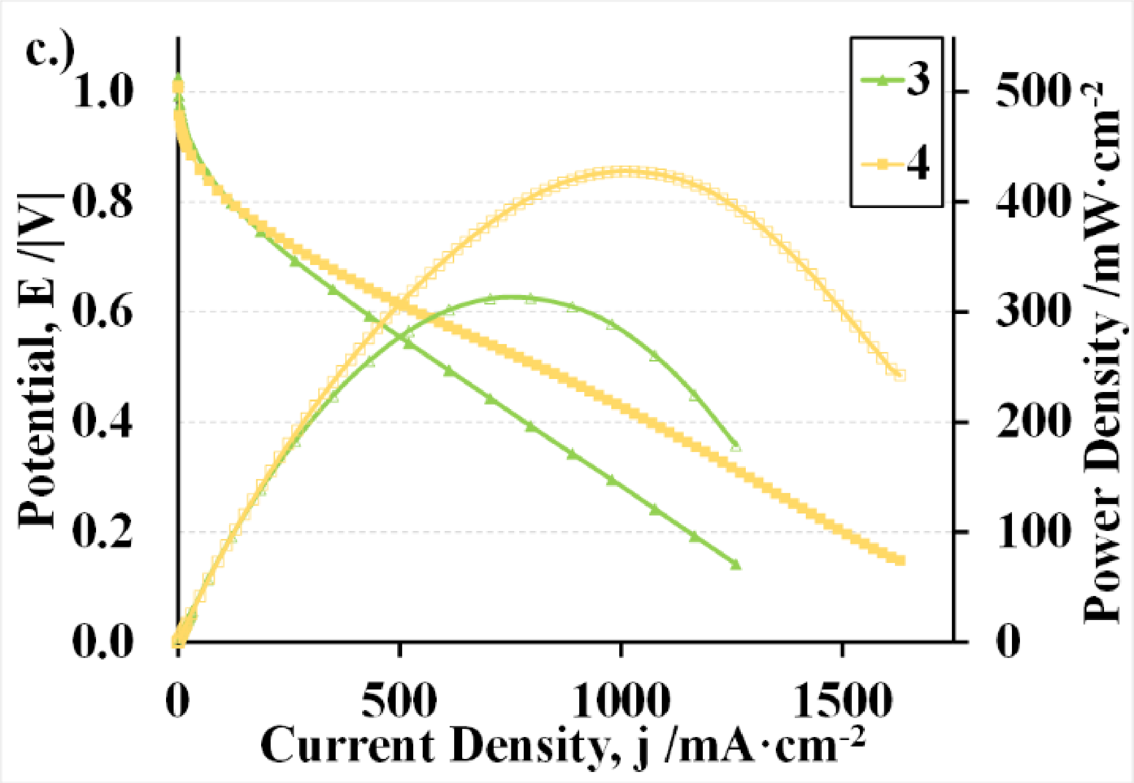

Figure 4.5: **Beginning-of-life, polarization and power density data for various AEMFCs prepared with different cathode catalyst layer deposition protocols. (a) Effect of increasing substrate temperature during 1-hour spray-coating protocol: 80 °C (CCM 2), 120 °C (CCM 3), 150 °C (CCM 5) with power densities 224, 313, and 326 mW·cm^{-2}, respectively. (b) Effect of increasing substrate temperature during 4-hour spray-coating protocol: 50 °C (CCM 1), 120 °C (CCM 4), achieving 276 and 428 mW·cm^{-2}, respectively. (c.) Effect of increasing the time of spray-coating protocol using constant substrate temperature (120 °C): 1-hour (CCM 3), 4-hour (CCM 4), with power densities 313 and 428 mW·cm^{-2}, respectively. Fuel cell operating conditions: 60 °C, 0.5/1.0 slpm H_2/O_2, and zero backpressure; all data confirmed via multiple repeated polarization curves.**

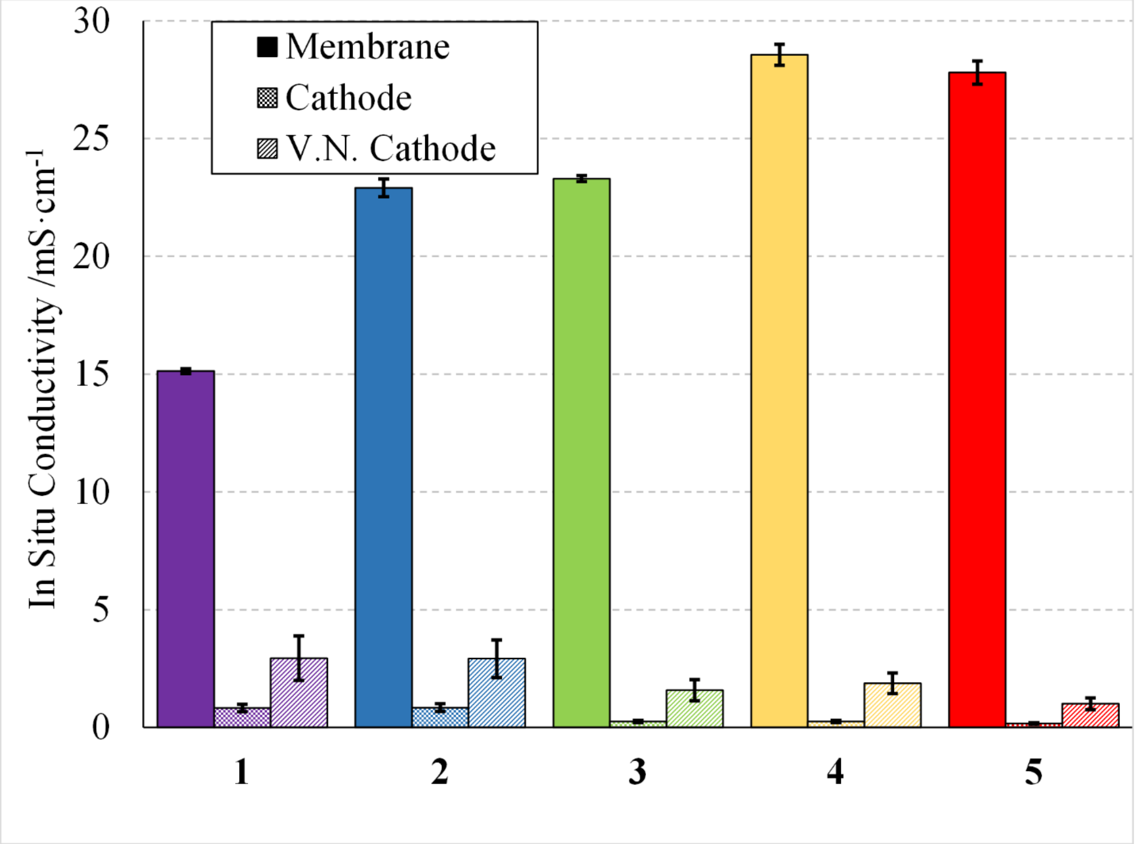

Figure 4.6: ***In situ*** **fuel cell membrane conductivity values calculated from area-normalized resistance (iR data)[127] at 500 mA·cm^{-2} (left bar);** ***in situ*** **cathode ionomer conductivity obtained by EIS: absolute conductivity (centre bar) and normalized to 100% ionomer by volume (right bar). Error bars represent the average ± sample standard deviation for all data.**

4.3.3. Electrochemistry

Gas crossover current densities of 0.3, 2.9, 0.5, 1.3, and 0.6 mA·cm^{-2} were determined from chronoamperometry data, specifically the steady-state current density at 0.5 V applied potential, for CCMs **1-5** (see Table 4.4). Values were determined post-operation, i.e. after the onset of performance losses, after equilibration to low potentials under H_2/N_2 gas flows. Linear-sweep voltammetry revealed the presence of small electrical shorts for all AEMFCs, indicating that the fuel crossovers determined by chronoamperometry were larger than the actual value. When corrected for electrical shorts, gas crossover currents were low, which is not unexpected for hydrocarbon CCMs. From CV data, the estimated electrochemically active surface areas (ECSAs) for CCMs **1-5** are reported in Table 4.4, and are similar for all cells and independent of CL pore size.

The double-layer capacitances (C_{dl}) of CCMs **1** and **4** (219 and 235 mF·$g^{-1}{}_{Pt}$, respectively) were half that of CCMs **2**, **3**, and **5** (352, 417, and 392 mF·$g^{-1}{}_{Pt}$, respectively); Table 4.4), noting that **1** and **4** were prepared over a longer time period (Table 4.1). In polymer electrolyte electrodes, C_{dl} is typically considered to vary directly with carbon surface area, these data suggest an alteration to ionomer morphology in **1** and **4**.

Ionomer conductivities, determined by EIS, were 0.83 ± 0.16, 0.84 ± 0.16, 0.25 ± 0.05, 0.25 ± 0.05, and 0.17 ± 0.03 mS·cm^{-1} for **1-5** (Fig. 4.6). When normalized to 100% of cathode CL volume from calculated vol% composition determined from SEM measurement and material densities, conductivities were 2.9 ± 0.9, 2.9 ± 0.8, 1.6 ± 0.3, 1.9 ± 0.2, and 1.0 ± 0.2 mS·cm^{-1} for **1-5** (Fig. 4.6). All electrodes had equal masses of ionomer, therefore thinner cathodes **1** & **2** contained a relatively greater ionomer content to **3-5** (Fig. 4.2). Accordingly, CCMs **1** & **2** showed expected higher absolute and volume-normalized ionomer conductivities.[183] However, the volume-normalized ionomer conductivity of CCM **5** was unexpectedly lower than that for CCMs **3** and **4**, despite near-equal cathode thicknesses (Table 4.3). The ionomer conductivity of CCM **4,** 0.25 mS·cm^{-1} was found to be consistent with the value of 0.27 ± 0.05 mS·cm^{-1} which was determined to be consistent across a range of EIS biases/potentials (Table 4.5). This confirms the EIS parameters used in this study were appropriate for the determination of ionomer conductivity.

DC Potential	AC Potential	σ_{OH^-}	V.N. σ_{OH^-}
250	10	0.31	2.26
300	10	0.40	2.92
350	10	0.19	1.41
450	**10**	**0.25**	**1.88**
500	10	0.25	1.88
550	10	0.25	1.83
600	10	0.34	2.54
650	10	0.31	2.29
750	10	0.30	2.23
850	10	0.29	2.12
950	10	0.32	2.33
1050	10	0.32	2.37
450	5	0.20	1.45
450	15	0.22	1.63
450	20	0.23	1.67
450	30	0.19	1.41
450	50	0.21	1.54
450	70	0.29	2.17
450	100	0.23	1.69
Average of data:		0.27±0.05	1.9±0.4

Table 4.5: Results of EIS study on CCM 4, with reporting absolute hydroxide conductivity and conductivity as volume-normalized to 100% volume for comparison to membrane data. Standard conditions used on other CCMs in this study in bold. Averages ± population standard deviation are provided analysis as per prior work.[183]

4.3.4. AEMFC Polarization Data

Conditioning of AEMFC at potentials between 0.5 and 0.2 V represents a significant difference to conditioning PEMFCs, because continuous operation at high currents/low potentials may lead to flooding in PEMFCs.[246] High gas flow rates (1.0/0.5 slpm O_2/H_2) are typical for beginning-of-life fuel cell analyses as they provide an initial indication of AEMFC performance by eliminating hysteresis from flooding in the mass-transport region. However, even operating an AEMFC at 95-100% RH, high gas flow rates may lead to dehydration of the membrane/ ionomer, as revealed by iR.

The rate for acquiring data points to construct polarization curves was chosen to provide the most adequate comparison of data, independent of temporal water management issues.[251] The power densities observed for AEMFCs are among the highest current and power densities reported in literature for AEMFCs under these conditions (i.e. 60 °C, zero backpressure, Pt/C as both anode and cathode electrocatalyst at standard loadings).The highest value, 428 mW·cm^{-2} (for CCM **4**) represents a significant increase in AEMFC power densities achieved using FuMA-Tech FAA-3. The best value reported previously was 223 mW·cm^{-2}.[84,246,252,253]

4.3.5. Catalyst Layers

THF and MeOH were chosen as solvents for the catalyst inks to minimize the dielectric constant. This has been shown to create colloidal dispersions of catalyst solids and increase the average pore size in electrodes.[182,100] The dielectric constant achieved (21) was substantially lower than a standard water/MeOH mixture (57),. The thinnest cathode CLs obtained using substrate temperatures of 50 and 80 °C (7.6 and 7.5 μm in CCMs **1** & **2**, corresponding to total internal porosities of 0.688 and 0.674 cm^3·g^{-1}, respectively, were significantly more porous than CLs described in a previously reported study on the microstructure of spray-coated AEMFC CLs, which used comparable commercial materials (0.143 cm^3·g^{-1} for the equivalent 25 wt% AS-4 ionomer to 0.589 cm^3·g^{-1} for pure Pt/C catalyst). The thicker electrodes in CCMs **3**, **4**, and **5**, prepared using substrate temperatures of 120, 120, and 150 °C (11.1, 11.8, and 11.5 μm, corresponding to 0.795, 0.767, and 0.976 cm^3/g Pt, respectively), displayed thicknesses on par with optimized Nafion® and high-performance hydrocarbon electrodes for PEMFCs (12.4 and 10.7 μm, respectively, accounting for loading – see Fig. 4.2). Although catalyst ink was observed to evaporate near-instantaneously in each of CCMs **1**-**5**, this observation suggests that a high instantaneous rate of evaporation, caused here by very low ink flows and substrate temperatures greater than the boiling point of the bulk of the solvent, significantly increases the porosity of the catalyst layers. Further, noting no substantial differences in CL thickness between CCM **3** deposited over 1-hour and CCM **4** deposited over 4-hours, CL thickness appears to be independent of the degree to which high-boiling solvent was driven from the CL.

Despite good improvement over literature values, cathode CLs of CCMs **1** and **2** were still incapable of operating with fully hydrated ionomer according to the calculations of void space available, due to the cathode CL having zero void space at full ionomer hydration.[182] The greater volumes of the cathode CLs in CCMs **3**, **4**, and **5** would allow the ionomer to operate fully hydrated (see Fig. 4.2).[183] Full hydration has consistently proven necessary for the stability of AEMFC membrane/ionomer, so this result suggests enhancements in CLs design will lead to more chemically stable catalyst layers in addition to other benefits, such as improved mass transport. Understanding and delineating the impact of high internal pore volume – void space not occupied by catalyst, catalyst support, or ionomer in a hydrated state – and mesoporosity – pore volume between electronically connected catalyst support particles specifically in the range of 15-100 nm – on the mass transport and stability of AEMFC CLs is vital to electrode engineering to create efficient and stable systems.

Additionally, full hydration and back-diffusion of water is vital to maintain a high level of hydroxide conductivity and chemical stability of the membrane/ionomer.[238,254] It is observed that better-formed porosity gradients in CLs allow the membrane to operate in an effectively higher hydrated state, increasing membrane conductivity (Fig. 4.6). This mitigates the dehydrative effects of high gas flows discussed above. The highest membrane conductivity measured under the test conditions described, 28.8 $mS\cdot cm^{-1}$, obtained for CCM **4**, is consistent with the reported ex situ, value for fully hydrated hydroxide-conducting membrane (50 $mS\cdot cm^{-1}$), which is indicative of facile water transport between electrodes.

However, the substantial differences in polarization data between CCMs **3**, **4**, and **5** warranted a more thorough investigation of catalyst layer microstructure, and is presented as follows: the porosity in the mesoporous regime, 20-100 nm, was observed to vary substantially between CCMs, as can be clearly visualized in the cumulative pore areas (Fig. 4.3) and internal volumes (Fig. 4.4a) in this region. This data provides a better indicator of electrode quality than the total internal volume or pore area (Table 4.3). Mesoporosity better determines mass-transport through the catalyst layer than total porosity, because total porosity includes nanoporosity, and nanopores are largely blocked with ionomer during fuel cell operation and thereby of minimal impact to mass-transport.

The presence of even low amounts of NMP (e.g., 2.2 wt%) in the catalyst ink is believed to cause a reduction in mesoporosity by its effect of solvent annealing. Well-formed microstructure subsequently alters electrode conditioning, reducing cathode annealing in-situ (Fig. 4.1).

The double-layer capacitance (C_{dl}), a measure of the interfacial area between wetted ionomer-catalyst or wetted ionomer-catalyst support , increases with ionomer content and increases proportionally to ECSA in typical CLs.[255] However, C_{dl} found for the

CCMs deposited over 4-hour (CCMs **1** and **4**) were half of CCMs deposited over 1-hour (CCMs **2**, **3**, and **5)** (see Table 4.4). This data suggests an alteration to ionomer morphology in the 4-hour CCMs, **1** and **4**, caused by long periods of time where the electrode sat at high temperature between the deposition of ultra-thin layers. The temperature of CL formation in all cases is well below the T_g of the polymer (185 °C), suggesting this is due to a solvent effect. Since low-boiling solvents including water evaporate near-instantaneously in all of CCMs **1**-**5**, the cause of the differences in microstructure between 1-hour and 4-hour CCMs is believed to be low rate of evaporation of the high-boiling solvent, NMP, from the CL. The differences in C_{dl} also suggest a possible alteration in catalyst-ionomer surface area without proportionate loss of catalytic surface area, this could potentially be due to a difference in morphology.

Studies of catalyst ink structure during the solvent evaporation process, backed by SANS data, suggest a phase inversion that reduces catalyst-ionomer interface.[256] Studies suggest a thin layer of ionomer coats catalyst/support particles and partially peels off during drying. Phase inversion occurs as the hydrophilic groups of the ionomer re-orient from the water-containing solvent to other hydrophilic surfaces, e.g. catalyst/support. The polar NMP potentially disrupts this process by wetting the ionomer and prevents fully effective phase inversion, possibly increasing the ionomer-catalyst/support interfacial area without generating more active area. A more effective reduction in the quantity of high-boiling solvent in the CL during formation allows for a more complete phase inversion of the ionomer in the drying process.

The improvements in kinetic polarization data for CCM **5** suggest an increased hydroxide ion concentration at active sites, which may be related to the substantially increased nanoporosity (Fig. 4.3) increasing catalyst wettability; however, this may also result in additional mass transport losses.[257] The increase in nanoporosity may have been caused by the very rapid loss of low-boiling solvent at 150 °C.

CCMs **1**-**4** all displayed very similar total porosity (Table 4.3), but substantially different mesoporosities (Figs. 4.3 & 4.4). In particular, **4** displayed improved mesoporosity to **3**, both fabricated at the same temperature, 120 °C, but no substantial difference in nanoporosity was observed. The only difference between these was the degree to which the presence of high-boiling solvent was reduced.

One remaining question from this study is whether low-mesoporosity CCMs operate as stably as higher-mesoporosity CCMs. Calculations where fully hydrated ionomer would result in more than 100% of the actual CL volume being filled have been similarly calculated for cathodes containing hydrocarbon proton-exchange ionomers after annealing caused by high-boiling solvent in the catalyst ink.[183] The logical conclusion is that the ionomer in the CL operates at an effectively reduced hydration state under these circumstances, problematic for AEMs that significantly decrease in chemical stability at lowered water contents. Therefore, it is likely that low mesoporosity likely prevents any stable anion-exchange ionomers *in situ* and contributes to AEMFC instability, which highlights the need to understand each porosity regime in electrode studies.

High-resolution SEM, a standard qualitative analysis of catalyst layer formation, was used to gain understanding of morphology of CLs before and after fuel cell operation. The macroporous scale (Fig. 4.1, top row) probes the pores between aggregates.[257] This revealed smaller feature sizes in CCM **4**, corresponding to improved electrode conditioning and overall water management. This suggests that the morphology of the catalyst layer is changing during conditioning. CCM **2** appeared to have very few mesopores relative to the other CCMs, but was the only CCM for which significant annealing was observed. Otherwise, despite resolving the image of individual catalyst nanoparticles to a scale of ~10 nm, no conclusive differences in CLs were observed at the meso- and nano-scale. This again highlights the importance of gaining porosity data in order to understand electrode compositions in the various size domains.

In summary, AEMFC CL microstructures can be rationally controlled to a significant degree by way of factors other than catalyst ink composition, i.e. by controlling the method, time, and substrate temperature of CL deposition, which may lead to substantial gains in fuel cell performance and stability. Further studies structure-properties relationships of anion-exchange ionomers will serve to extend the lifetime of AEM electrodes.

4.4. Conclusions

Reducing the presence of high-boiling solvent in catalyst inks during electrode formation is shown to substantially improve the Ohmic and mass-transport regimes for FAA-3-based AEMFCs, with maximum power densities increasing from 276 to 428 mW·cm^{-2}, under zero gas backpressure. These improvements can be directly correlated to an increase in mesoporosity of the catalyst layer (CL). Increasing the nanoporosity of the CL was found to have a positive impact on kinetic-region performance but induced additional mass-transport losses under higher current loads. CLs possessing the highest mesoporous area led to the highest AEMFC power densities, significantly larger than previous report values for FAA-3 under similar conditions. This study highlights the need to develop anion-exchange ionomers that are soluble in low-boiling solvents in order to further enhance AEMFC fuel cell electrochemistry and a greater need to develop *ex situ* characterization methods, e.g., conductivity, dimensional swelling, and temperature stability under conditions relevant to fuel cell operation, in order to more accurately evaluate emerging anion-exchange membranes and ionomers.

4.5. Critical Discussion

While this work was undertaken some time ago and achievable power densities have increased drastically, this work still represents the highest power densities achieved with FAA-3 in the literature and remains among the very few works to have separately examined AEMFC catalyst layer morphologies experimentally. The conclusion that achieving high mesoporosity as a potential means of directly enhancing mass transport, predominately of water out of the anode for enhanced potentials at higher current densities and water into the cathode for enhanced reaction kinetics, has been borne out directly by more detailed studies concluding increased void volumes were confirmed to be related to potential gains at high pressures.[258] Enhancements to achievable power densities resulted from several studies into electrode hydrophobicity, GDL composition and interactions that concluded anode flooding was the major mass transport limitation to AEMFC systems. This was recently thoroughly addressed by an alternative method of forming electrodes recently pioneered by Mustain, Varcoe, & coworkers. Instead of forming a catalyst ink to mix ionomer and electrocatalyst, their method mixes these in the solid-state, grinding up insoluble membrane as a catalyst agglomerate ionomer-like coating, forming highly heterogeneous, very high void-space membranes. Such electrodes have demonstrated an ability to enhance achievable mass transport significantly and set record power densities in both oxygen and CO_2-free air without backpressure.[259] While better understanding the catalyst layer morphology, ionomer-catalyst interactions, hydrophobicity/hydrophilic effects will be a difficult challenge, investigating this radical new approach to catalyst layer formation is now significantly of interest to the field, with the open question being whether these electrodes can be made long-lived and reproducible. If stability and longevity are achievable, this method may dominate AEMFC anodes if not whole-cell constructions for some time. Even if this proves not to be the case, it makes a strong case that nanostructured thin-films, potentially ionomer free, offer great potential for large enhancements to AEFMC performance. Any normally formed CCM will require ionomer, GDL, overall electrode composition, and membrane all tuned for ultra-high water transport from the anode.

With respect to traditionally formed CLs, ionomer stabilization has been minimally addressed by academia; this has been shown to be highly impactful to AEMFC lifetimes for some time[242] and are a logical extension of any work on catalyst layer ionomer stability. However, applications of this strategy have been few and improvements on this method in the past decade have been slow and incremental.[260]

A number of other important developments have begun to address concerns raised in this chapter. A new membrane test method for determining hydroxide conductivity free of carbonates is proving to be consistent and effective in correcting the disparity between *in situ* and *ex situ* conductivity measurements.[261,262] Advanced imaging is resulting in a greatly enhanced understanding of the effects of carbonation and an improved theoretical understanding of water transport as it relates to *in situ* AEMFC stability, particularly pertinent to ionomer in the cathode catalyst layer.[55,263] Translation of the theoretically enhanced ORR kinetics in AEMFCs into measurable efficiencies higher than PEFMCs is being been achieved alongside rapid enhancements to both ORR and HOR catalysts in alkaline environments.[264] Promising advances in PGM-free alkaline membrane water electrolysis are also being achieved with equivalent efficiencies to PEM-based systems, with the promise of significantly reducing the cost of high-purity hydrogen.[265] Together, these advancements are addressing all major challenges set for the field in the 2014 key review[84] and the 2016 AMFC workshop.[86]

The one major challenge of the 2016 DOE AMFC workshop that remains largely unaddressed in the field is standardizing *in situ* methodology. In that category, the only widely adopted sub-recommendations were the requests that researchers measure polarization data according to specific current densities rather than potentials to set a constant reaction rate (i.e. collect amperometric vs. potentiometric polarization data) and that systems not exceed 100% RH humidification. The first better resolves the Ohmic region, which is a complex and not fully understood region in AEMFC operation, in stark contrast to PEMFCs. The second recognizes that active condensation of water into a system isn't achievable beyond the small research scale and doesn't aid the development of stable systems for real-world conditions. While it is unlikely conditioning procedures can be fully standardized due to practical considerations, e.g. titrating the carbonate out of hydroxide and full hydroxide exchange of membrane and ionomer may need to be employed occasionally but neither are likely to be necessary for most studies, reporting of data certainly can be standardized. The workshop recommendation was to 'report everything.' While this has improved somewhat, of particular note in the literature are the still near-ubiquitous short time-scales for polarization curves. Best practices for PEMFCs are 5 $\text{min}\cdot\text{pt}^{-1}$, as this is well beyond the threshold for water equilibration to occur at a given current density. By contrast, typical hold times in AEMFC polarization data are less than 10% of that, and furthermore hold times are typically not reported clearly in time per point but as a rate of current density or potential change per unit time (e.g. $\text{mV}\cdot\text{s}^{-1}$). Steady-state values (e.g. current hold) are rarely reported. Moving towards longer polarization time-scales and accurately reporting long-run data is critically important to advancing the development of AEMFCs.

Chapter 5. Reducing Interfacial Resistances in Fuel Cells – a Completely Spray-Coated Membrane-Electode Assembly

*This chapter apart from the critical discussion has been published as peer-reviewed research.[266]

Klingele, M.; Britton, B.; Breitwieser, M.; Vierrath, S.; Zengerle, R.; Holdcroft, S.; Thiele, S. *Electrochem. commun.* **2016**.

Individual contributions were:

MK: MEA characterization, manuscript lead & analysis

BB: Method design & experimental, MEA characterization, analysis

MB: MEA characterization & analysis

SV: Experimental assistance

RZ: Supervision (Germany – IMTEK, Freiburg)

SH: Scientific supervision (Canada – SFU Chemistry & 4D Labs, Burnaby)

ST: Scientific supervision (Germany – IMTEK Porous Media Group, Freiburg)

5.1. Background

Membrane electrode assemblies (MEAs) in proton exchange membrane fuel cells (PEMFCs) are responsible for 35 – 45 % of the costs of a fuel cell stack.[267] Most related research is focused on cost-reduction of the oxygen reduction catalyst,[268–271] or cost-reduction of the proton exchange membrane,[272–274] and little fundamental research has focused on alternative MEA manufacturing routes as a means of cost-reduction.[127,144] Two established manufacturing strategies exist for building MEAs: either a pre-cast polymer electrolyte thin film is coated with catalyst layers by spray-coating or decal techniques to form a catalyst coated membrane (CCM), which is then stacked between gas diffusion media, or gas diffusion electrodes (GDEs) are stacked with a PEM foil in between.[275] Both approaches require a free-standing membrane foil, limiting membrane thickness and causing high production costs from the foil processing of the polymer electrolyte. In industrial applications, CCM fuel cells are predominantly employed, due to their relatively better adhesion of catalyst layer and membrane, resulting in higher achievable power densities and mechanical durability.[267]

Recently, a new approach to MEA fabrication was presented in which thin layers of polymer electrolyte dispersion were inkjet-printed directly onto two GDEs.[127,144] This solution-cast polymer electrolyte layers provided a complete substitute for the membrane foil when the two GDE-polymer electrolyte half-cells were sandwiched together. This new construction promised a high potential for cost savings by eliminating the foil processing step. Additionally, it was shown that without the need for free-standing membrane, much thinner membranes can be formed without the risk of gas crossover (as shown by accelerated mechanical and chemical stress cycling[85]). Superior maximum power densities were achieved by the membrane-foil-free MEAs compared to conventional CCM references. However, inkjet-printing as a membrane deposition technique is slow, thus unsuitable for industrial-scale MEA manufacturing. As a result, membrane deposition by spray-coating was investigated as a fast, facile technique for MEA manufacturing, already proven viable on the industrial scale. By spray-coating, manufacturing times for a 5 cm² MEA can be reduced from 10 – 20 minutes to below 60 seconds. Additionally, since catalyst layers are already spray-coated in many industry-scale MEA production lines, spray-coating of the membrane does not require any additional tooling for MEA production. Hence, membrane spray-coating allows for complete MEA production by a single device.

Altogether, an MEA production route was demonstrated where catalyst layers and membrane layers are consecutively spray-coated onto a carbon-fiber gas diffusion layer with applied microporous layer as substrate. To form a fuel cell, anode and cathode half-cells are assembled with the membrane layers facing each other. A cross-section of the resultant DMD fuel cell is shown in 4.1b.

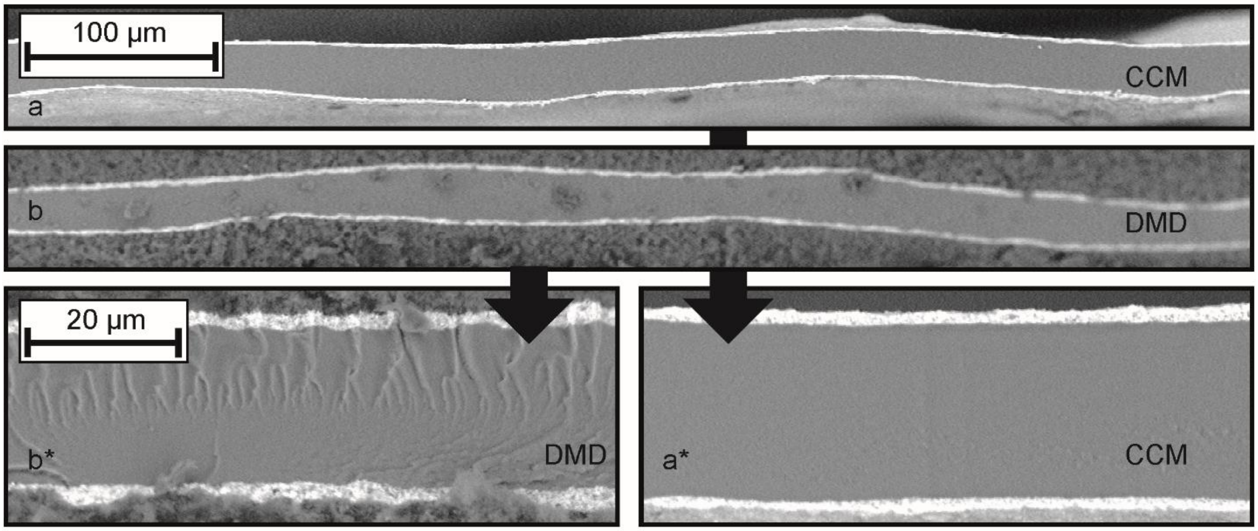

Figure 5.1: Cryo-fractured cross-sections of the spray-coated DMD fuel cell (b) and the reference Nafion NR211 CCM (a). The rough surface of the DMD cross-sections is an artifact from the sectioning procedure, which occurs when GDL fibers are still attached while fracturing.

A PEMFC constructed by the DMD method was shown to exhibit reduced Ohmic and mass-transport losses, thereby outperforming a state-of-the-art Nafion NR211-based CCM reference in terms of cell power and cell resistance, although in both samples the membrane layers are equivalent in terms of membrane thickness (ca. 25 µm); catalyst layer material, loading, and fabrication method; and gas diffusion media.

5.2. Experimental

A 4 cm² PEMFC was manufactured by consecutively spray-coating catalyst layers and ionomer layers directly onto the microporous layer (MPL) of gas-diffusion layers (GDLs). To form a fuel cell, the resultant anode and cathode half-cells were assembled with the membrane layers facing each other, with a subgasket used to prevent gas crossover through the edges of the electrodes.[85] As a GDL-MPL substrate, SGL Sigracet 24BC was used. For the spray-coating of the catalyst layer and membrane layer, a commercially available table-top spray-coater (Sono-Tek Exacta-Coat SC) was used.

The catalyst-ink preparation comprised 1 wt.% solids in 3:1 MeOH:H_2O, the solids 30 wt.% Nafion ionomer (based on Nafion D520) and 70 wt.% Pt/C (46.4 wt.% Pt, TKK TEC10E50E). A catalyst layer with a Pt loading of 0.1 mg Pt·cm^{-2} (corresponding to 2 – 3 µm CL thickness) was spray-coated onto the GDL-MPL to form a GDE. This resulted in a symmetric loading of each 0.1 mg Pt·cm^{-2} on anode and cathode side. No penetration of catalyst particles into the MPL by spray-coating was found, as can be observed from the sharp separation of Pt-C particles from MPL particles in Figure 5.1b.

For the membrane coating, commercially available Nafion D520 dispersion was used. The ink was stirred for several hours to prevent polymer agglomerates. To create a spray-coated membrane layer with a total thickness of ca. 25 µm, 12.5 µm Nafion was sprayed onto each anode and cathode half-cell, corresponding to 2.55 mg Nafion·cm^{-2} on each electrode.

The fuel cell characterization was performed on a fuel cell test station (Scribner Associates Inc.) with a 5 cm² fuel cell fixture with serpentine flow channels. Galvanostatic polarization data was recorded with pure H_2 (0.25 slpm) and O_2 (0.5 slpm) feed, at 80 °C cell temperature and 92 % relative humidity (RH) at atmospheric pressure (100 % RH was avoided to prevent the cell from flooding). Data was recorded at increments of 10 mA/cm^2 from OCV to 200 mA·cm^{-2} with hold times of 1 min·pt^{-1} to resolve the kinetic polarization, followed by increments of 200 mA·cm^{-2} from 200-3000 mA·cm^{-2} with hold times of 5 min·pt^{-1} to ensure the measurement of steady-state fuel cell characteristics. Electrochemical impedance spectroscopy was conducted throughout the whole range of current densities with 0.25 slpm H_2 and 0.5 slpm O_2 gas flow at 80 °C and 100 % RH with a frequency range of 0.1 Hz to 10 kHz. To gain insight into catalyst layer proton conductivty, the cell was equilibrated to a steady low potential < 0.15 V under 0.25/0.25 slpm H_2/N_2 and impedance spectroscopy was conducted at 80 °C cell temperature and 30 % RH in a frequency range of 0.1 Hz to 10 kHz. Linear sweep voltammetry (LSV) was conducted under 0.2/0.05 slpm H_2/N_2, 100 % RH at a rate of 1 mV·s^{-1} from OCV to 600 mV.

A reference Nafion NR211 CCM-type MEA with equal membrane thickness, catalyst layer composition, and gas diffusion media was used for comparison. The CCM was tested under the same conditions as the completely spray-coated MEA.

5.3. Results & Discussion

Gas crossover, especially hydrogen crossover from anode to cathode side, limits cell lifetime and lessens cell performance.[108,276] Hence, it is particularly important for commercial fuel cells to exhibit as little gas cross-over as possible. Hydrogen crossover can be determined *in situ* by LSV. Typical values for a fully hydrated Nafion NR211 membrane are in the range of 1-2 mA·cm^{-2}.[41] Figure 5.2a shows the LSVs of the spray-coated DMD and the CCM fuel cell.

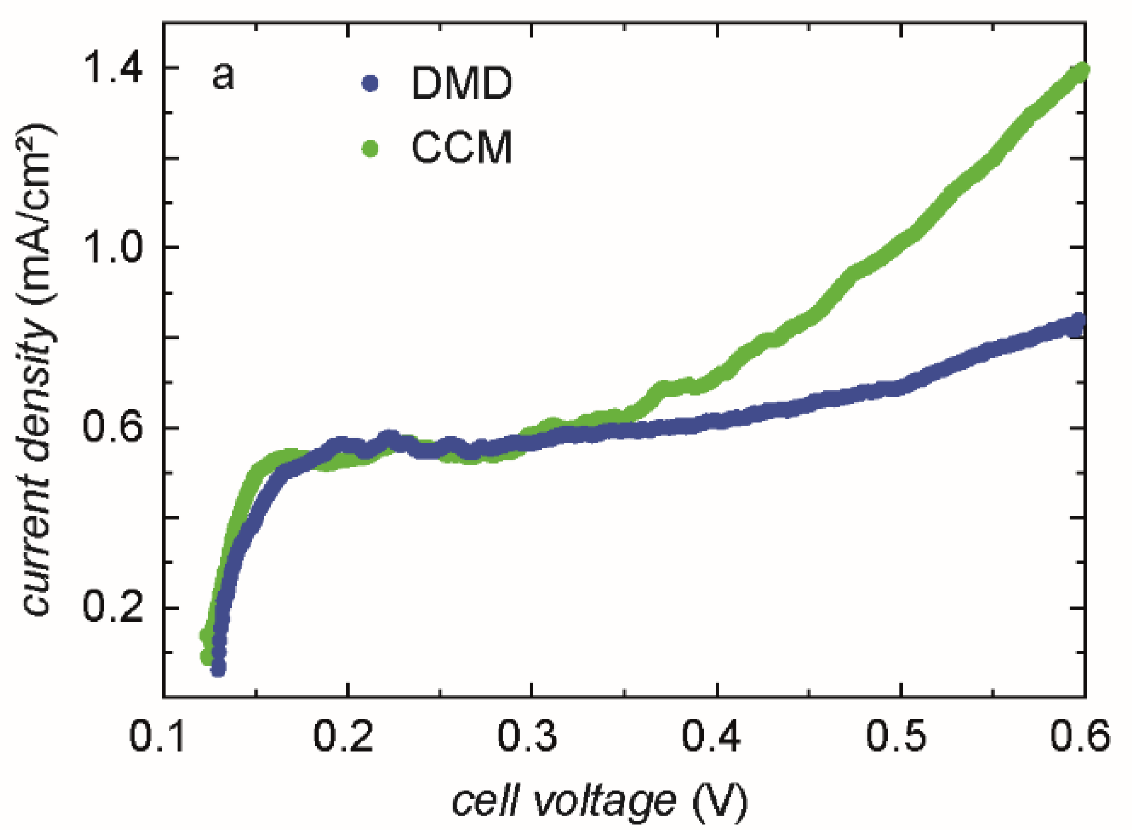

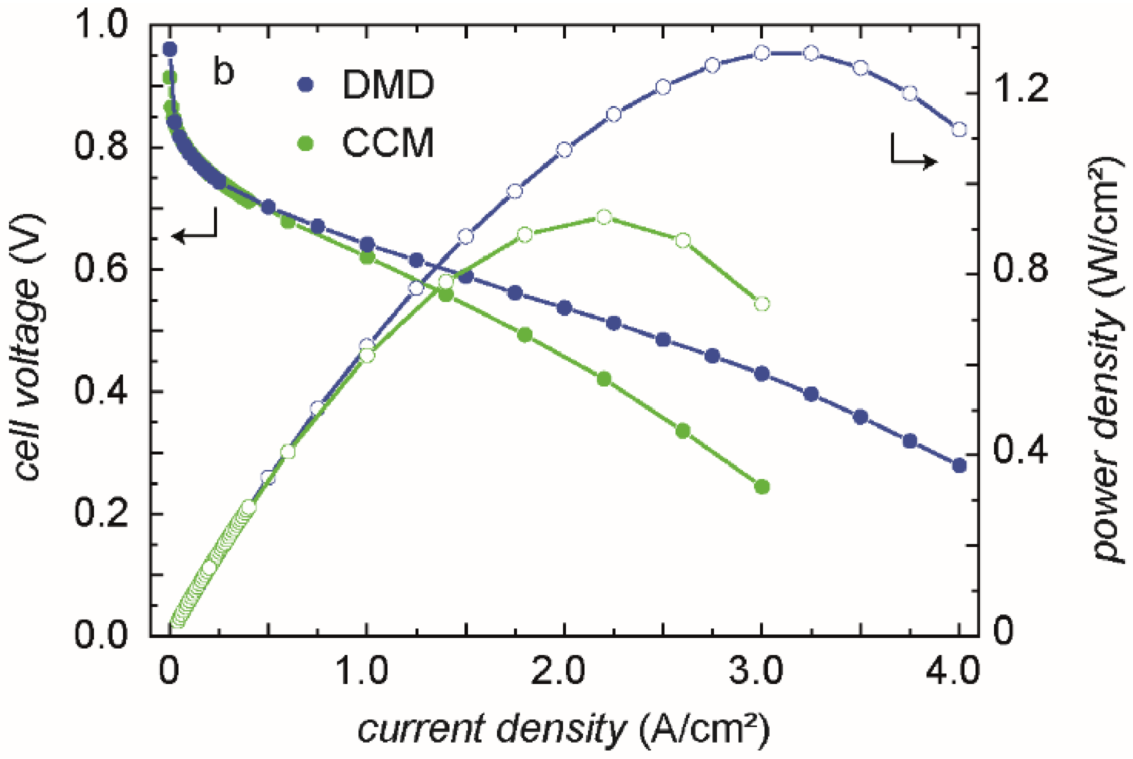

Figure 5.2: **a) LSV data of the spray-coated DMD and the CCM (80°C, 100 % RH, 0.2 slpm H_2, 0.05 slpm N_2). The crossover current density does not exceed 1.5 mA/cm² in the range of 0 – 0.6 V. b) Cell voltage and power density over current density of the spray-coated DMD fuel cell and the CCM reference (80°C, 92 % RH, 0.25 slpm H_2, 0.5 slpm O_2).**

Both samples show a crossover current density less than 1 mA·cm^{-2}. This shows that the spray-coated membrane is no less gas impermeable than the commercial Nafion NR211 membrane. In addition, no electrical shorting was identified (observed in LSVs as a linear increase of the current density with increasing cell voltage), proving excellent electrical insulation between electrodes by the spray-coated membrane.

Polarization and power density data comparing the completely spray-coated DMD fuel cell and CCM reference are shown in Figure 5.2b. A 1.39 times higher cell power density of the DMD fuel cell when compared to the CCM reference is observed. This result is surprising, since equally thick membranes and equal catalyst layers with respect to catalyst (46.4 wt.% Pt/C) at low loading (0.1 mg Pt/cm²) were used in both samples. These similarities would normally engender very similar fuel cell performances. The equally thick membranes result in a similar high-frequency resistance in the range of 41 – 43 mΩ·cm² in the Ohmic region of the polarization at a current density of 1.5 A·cm^{-2} (determined by the high frequency intercept of the Nyquist plot, as also shown in Figure 5.2b). The similarity (in terms of loading) of the catalyst layers is evident given the similar kinetic polarization of the spray-coated DMD fuel cell and the CCM in the range of 0 – 250 mA·cm^{-2}. A decreased effective charge-transfer resistance R_{LF-HF} can be identified throughout the whole range of current densities, to which the higher achievable power densities may be attributed. Here, R_{LF-HF} is defined as the subtraction of the high frequency resistance intercept with the real axis from the respective low frequency resistance, as determined from the Nyquist representation of EIS measurements.

R_{LF-HF} consists of charge transfer limited resistances at lower current densities, but contains contributions from oxygen transport resistance at high current densities. This leads to a characteristic evolution of R_{LF-HF} with current density, where R_{LF-HF} decreases with increasing current densities until purely Ohmic losses dominate. With further increasing current density, R_{LF-HF} increases again, as resistances from oxygen transport limitations are present. Such an evolution is shown for the DMD and CCM fuel cell in Figure 5.3b, while Figure 5.3a shows the Nyquist plots of the impedance spectra at current densities of 1, 2 and 3 A·cm^{-2}.

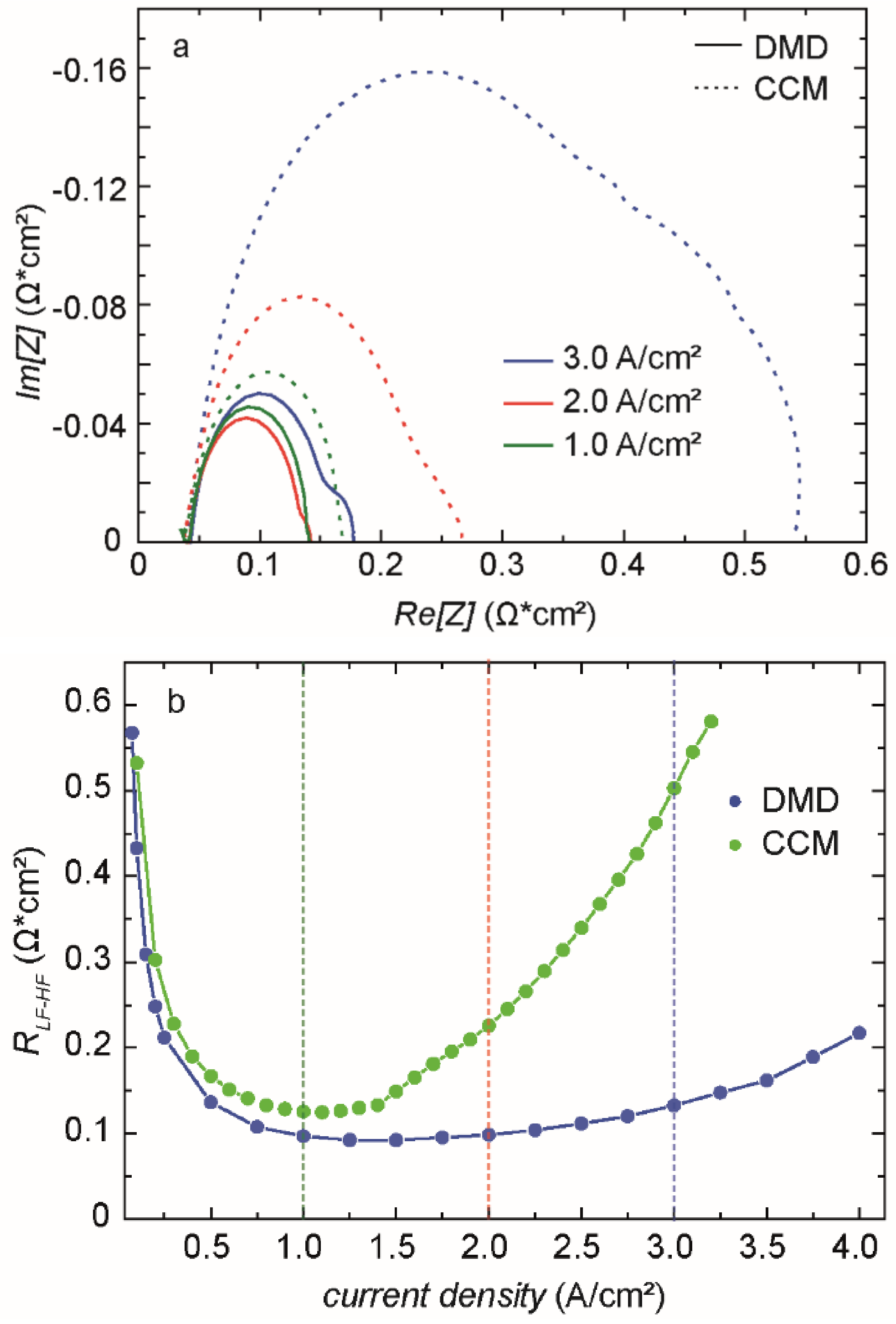

Figure 5.3: a) Nyquist representation of EIS data of the spray-coated DMD and the CCM reference at 1, 2 and 3 A·cm^{-2}. It is revealed that the DMD inhibits a generally lower $R_{LF\text{-}HF}$, which is especially pronounced at higher current densities. b) Fully resolved evolution of $R_{LF\text{-}HF}$ over the whole range of current densities.

It is revealed that the DMD inhibits an overall lower charge transfer resistance (92 mΩ·cm² at 1.5 A/cm², 133 mΩ·cm² at 3 A/cm²) compared to the CCM reference (149 mΩ·cm² at 1.5 A/cm², 503 mΩ·cm² at 3 A/cm²). This effect is especially pronounced at higher current densities, leading to the assumption that in this state of operation, oxygen diffusivity is favored compared to the CCM reference. This most likely originates from differences in water management within the catalyst layers of DMD and CCM, where it is assumed that flooding of pore space in the catalyst layer hinders oxygen diffusion throughout the catalyst layer. Water management can be influenced by operational conditions, back diffusion through the membrane, and catalyst layer morphology. Since operation conditions and membrane thickness are equal in both samples, it can be assumed that either the CL/PEM interface or the catalyst layer morphology of the DMD fuel cell improves water management. It is therefore theorized that the CL/PEM interface of the DMD fuel cell enhances water back-diffusion – likely due to a higher electrolyte contact area between CL and PEM – or that the CL of the DMD reveals a pore matrix that is more favorable for water removal. The latter would also hold true for the CL of a GDE MEA with a conventional membrane foil. In this case however, the disadvantageous interface of membrane and CL hinders good fuel cell performance.

Subsequent work on DMDs consisting of a detailed *in operando* EIS study of CCM, DMD, and GDE electrodes attempted to quantify the attributions presented above. DMDs exhibited a 52% reduction in ionic resistance compared to CCMs, from both a lowered membrane resistivity from an improved hydration state and reduced membrane-CL-MPL/GDL contact resistance effected by the construction methodology itself. However, the reduction in ionic resistance accounted for only 10% of the improvement to attainable power density, with reductions to mass transport losses accounting for 90%, primarily effected by enhanced water transport, including back-diffusion of water from the cathode.[277] It is suggested that a combination of improved interfaces and a reversed porosity gradient from catalyst layer deposition on the GDL/MPL rather than on the membrane (e.g. GDE-type rather than CCM-type) together enhance back-diffusion through the membrane, a combination only achievable with a DMD-type fuel cell construction methodology.

In order to evaluate the impact of the direct membrane deposition on catalyst layer proton conductivity, electrochemical impedance spectroscopy with an N_2-purged cathode has been performed.[164,278] Since in the DMD fuel cell production a liquid Nafion dispersion is spray-coated directly onto a porous catalyst layer, it is possible that a certain amount of Nafion dispersion infiltrates into the pore space of the catalyst layer, potentially changing its protonic transport characteristics. Figure 5.4 shows the impedance spectra of the DMD and CCM fuel cells.

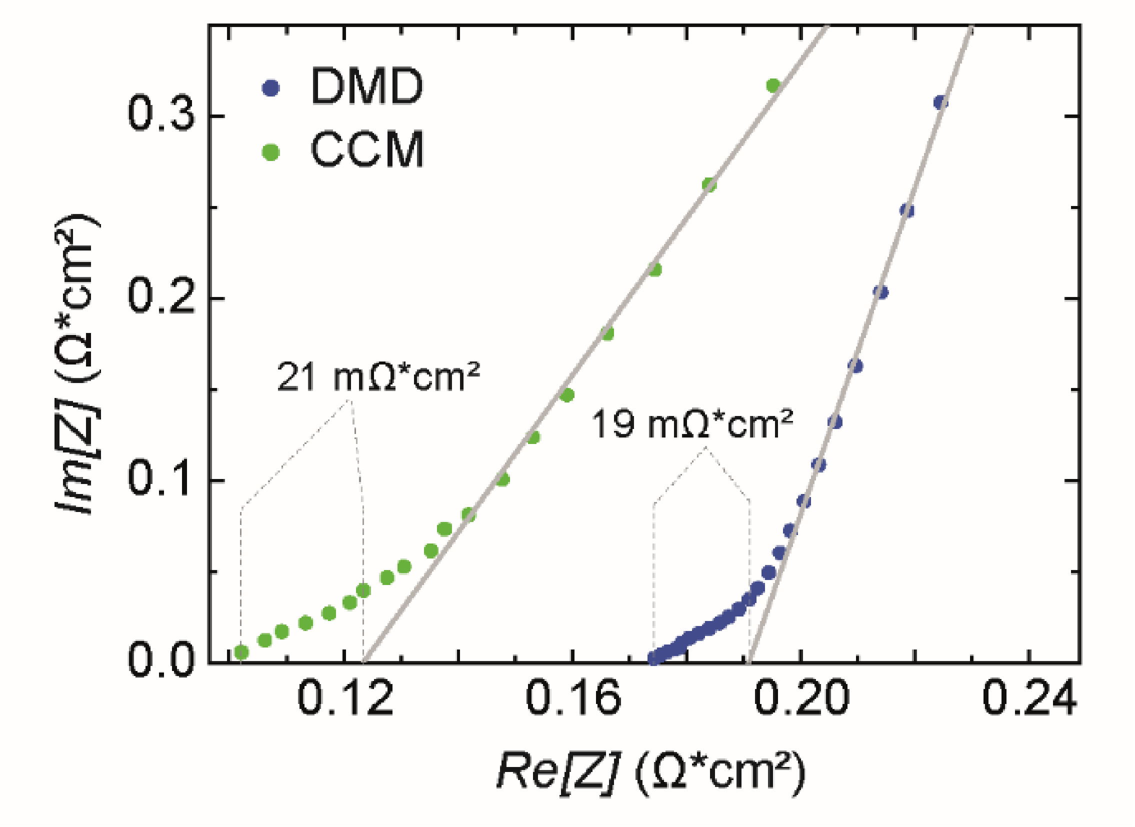

Figure 5.4: **H_2/N_2 impedance spectra of the spray-coated DMD and the CCM reference fuel cells. Operation conditions were H_2/N_2 0.25/0.25 slpm fixed flow, 80°C, 50% RH, ambient pressure. Catalyst ionic resistance accordingly are 63 mΩ*cm² (CCM) and 57 mΩ*cm² (DMD), which is comparable given the limited accuracy of the fit.**

The protonic resistivity is revealed to be comparable in both fuel cells (DMD: 57 mΩ·cm², CCM: 63 mΩ·cm². Calculated by three times the x-axis projection indicated in Figure 5.4.[164,278]). This indicates that negligible polymer electrolyte infiltrates the catalyst layer pore space in the deposition of the proton exchange membrane layer.

5.4. Conclusions

A proton exchange membrane fuel cell was constructed by consecutively spray-coating a catalyst layer and a proton exchange membrane layer directly onto a GDL/MPL substrate. This eliminates the need of expensive proton exchange membrane foils and presents a versatile technique by which MEAs can be inexpensively manufactured on the industrial scale with the potential to include additives into any layer and to develop asymmetric cells using a single system. Compared to a Nafion NR211 CCM reference, the equivalent spray-coated fuel cell with equal membrane thickness, catalyst material and loading exhibited a power density of 1.29 W/cm², outperforming the NR211 reference by a factor of 1.39. The origin of the superior performance was identified to be enhanced oxygen diffusivity throughout the entire range of current densities. Linear sweep voltammetry has proven the hydrogen impermeability and electrical insulation of the spray-coated membrane to be equal to that of the commercial Nafion NR211 membrane.

For the presented method for fuel cell manufacturing, nothing but a spray-coating device, a gas diffusion substrate, catalyst powder, Nafion polymer (powder, pellets, dispersion or any other form) and solvents are needed. Fuel cells can be manufactured up to industrial scale throughput without the necessity of purchasing costly membrane foils from third-party suppliers. The presented technique is especially interesting for hydrocarbon polymer electrolytes, where a much lower intrinsic gas cross-over allows the application of thinner membranes, leading to decreased cell resistance. Further, the technique is not restricted to proton exchange fuel cells, but can also be applied to any electrochemical device requiring MEAs, including anion exchange fuel cells and both acidic and alkaline membrane electrolyzers.

5.5. Critical Discussion

This paper established ‘direct membrane deposition’ as a technique of interest to large-scale manufacturing. Prior work using inkjet printing of membranes was not scalable for several reasons, including issues with reproducibility that would result in a high scrap rate at scale, difficult to scale equipment, and high fuel and electrical crossover (or low electrical membrane resistance).[279] Furthermore, system simplification in scale production is highly desirable, the main reason that significant resources were put towards the development of roll-to-roll catalyst layers deposited on a membrane substrate by slot-die casting. Inkjet printing of electrodes can be a viable way of producing electrodes given low-boiling solvents and extensive optimization of dielectric constant. However, the DMD method used spray-coated electrodes to achieve greater maximum power densities and consistent reproducibility. As a result, by the original method, two pieces of equipment were needed to produce a MEA – a spray coater for electrodes and an inkjet printer capable of processing high-viscosity, high wt% polymer dispersions. Inkjet printing of membrane required a piezoelectric printer designed for single-cell biotechnology applications to achieve the granular control. Despite this, the droplet volume was quite large. The only way to reduce crossover was to use a high wt% polymer dispersion, and that then required a single deposition layer to achieve a final membrane layer as thin as desired. The printer tubes were difficult to prime, clogged frequently, and needed to be replaced often. Because achieving viable low crossover values required the successful deposition of a single layer, if alignment was lost or the printer head jammed, the entire electrode was lost.

Spray-coating addressed all of these issues. Spray-coated DMDs reveal enhanced water transport far greater than the small gain shown by increased membrane surface roughness, more rigorously determine the reduction in PEM|CL interface resistance, and indicate that the ‘inverted’ catalyst layer assisted in creating an MEA with a catalyst layer porosity gradient more facile to mass transport.[181,277,280]

Chapter 6. Conclusions and Future Work

The work presented in Chapter 3 conclusively demonstrates that even very small quantities of high-boiling solvents (0.38%) anneal catalyst layer microstructure and substantially alter ionomer-catalyst/catalyst support interactions, with a concatenation of effects on the fuel cell *in operando*. In PEMFC cathodes, a direct comparison between catalyst inks comprised of low-boiling solvent and those containing small quantities of high-boiling solvent. This study revealed that high-boiling solvent anneals catalyst layers and results in increased Ohmic and mass-transport losses.

Combining these insights with subsequent work in the field, it is clear that the bulk properties of the ionomer (chemical stability, water uptake/swelling) and likely thin-film properties (e.g. transport properties in a thickness domain where nanophase segregation is difficult to impossible) – are insufficient to determine a construction for well-formed, high-efficiency electrodes, even when electrocatalyst/catalyst support is a set choice. The correspondence further decreases with low catalyst loadings and/or for cells designed to operate at high current densities. Solvent composition, deposition methodology, and interactions between the ionomer-catalyst/catalyst support all need to be optimized in concert to create consistently well-formed electrodes.

Compared to PFSAs, fully hydrocarbon sulfonated polyarylene structures as developed within the Holdcroft group possess solubility in low-boiling alcohols, rigid structures, high achievable ionic conductivities, promising oxygen permeabilities, innately high chemical stabilities, low-acidity breakdown products, and potentially tunable interactions with the catalyst support. Altogether, these should be investigated to overcome the limitations PFSAs exhibit, particularly towards the potential development of longer-lived, higher efficiency catalyst layers with low loadings of precious metal electrocatalysts or entirely non-precious catalysts (e.g. Fe-N-doped carbon structures). The differential interaction with advanced carbon supports (e.g. CNTs) or metal supports (e.g. Sn) should be additionally investigated, ideally aligning.

Chapter 4 presented the tunability of microstructure in AEMFCs, where mesoporosity, the total internal volume between ~20-100 nm, was found to be tunable as a function of the residence time of high-boiling solvent in the catalyst layer during deposition. Specifically, mesoporosity has significant impact on both the Ohmic and mass transport properties of these systems. Mesoporosity was confirmed to significantly affect water management in the electrode and was shown to be highly susceptible to solvent annealing. This annealing resulted in significantly reduced limiting current and peak power densities, and AEMFC lifetimes were reduced considerably. These factors are a result of the highly complex water management involved in AEMFC systems and the present necessity of full hydration to minimize membrane and ionomer degradation from hydroxide attack.

This result also strongly suggests the deposition method of the catalyst layer primarily determines its pore structure than the dielectric constant of or aggregates within the catalyst ink, of importance to the methods and conditions used in the mass manufacture of PEMFCs and AEMFCs, as well as catalyst layers generally.

In the past few years, materials development papers that include AEMFCs and catalyst layer specific papers have been preoccupied with achieving high power densities, particularly of note those using high-flux, heterogeneous catalyst layers. The attainment of higher power densities in CO_2-free air in these systems than in PEMFCs is unsurprising given the more facile kinetics of the ORR in alkaline versus acid as discussed in the introduction. However, using this technique, not only are system lifetimes untenably short, but system stability is markedly lower than in PEMFCs – stable balancing with backpressure is effectively impossible, and RH needs to be very carefully managed (i.e. within 1%) to cusp of flooded and dry states; the former reducing system efficiency far below desired (e.g. ¼ or less of the achievable power density), and the latter completely destructive to the ionomer and, if the state is extended, to the membrane, even for very stable base materials. For industry to trust academic data, not only does 'gold standard' 5 $min \cdot pt^{-1}$ data need to become the standard as suggested, but long-runs need to be valorized in the focus of the field. Existing long-run data in the literature bespeaks the large gap between polarization data measured transiently and potentials achieved in long-term, steady-state data, e.g. a 100-200 $mA \cdot cm^{-2}$ steady-state hold is not uncommon for systems capable of short-duration polarization data extending beyond 2 $A \cdot cm^{-2}$.

Industry presentations indicate that long-lived and efficient AEMFCs can be formed of an ultra-thin, high-flux membrane to back-diffuse the double-quantity of water produced at the anode in combination with differential catalyst layer design. In addition, GDL/MPL tuning, and gas manifolds designed for even gas flows and electrode hydration state are vital, although this is beyond the usual scope of materials-discovery groups. Finally, differential tuning of anode (hydrophobic) and cathode (hydrophilic) catalyst layer compositions, potentially including chemically stabilized ionomers, can be highly effective. Altogether, a combination of all these strategies is necessary to achieve long-term, whole-system function.

In the short-term, however, liquid fuels (e.g. alkaline DMFCs) offer several advantages to the advancement of AEM-based fuel cell technologies as a whole. A long-term developmental focus would be to use these fuels at high temperature, with fuel feeds as a vapour, harnessing the kinetic advantages high temperature provides. However, this strategy adds additional difficulties to that of hydrogen AEMFCs such as depolarization by fuel crossover, worse kinetics for fuel oxidation, and CO_2 production leading to carbonate formation *in situ*. By contrast, liquid-based systems offer a potential large advantage, specifically a chance to develop the cathode ORR separately while maintaining very high membrane hydration and water back-diffusion for cathodic operation and system lifetime without the highly variable effects of anode flooding. One exciting possibility that exists in alkaline systems without an acidic analogue stems from the relative non-susceptibility of electrocatalyst in alkaline to fouling and the potential to add conductive salts such as carbonate or hydroxide into the liquid fuel feed, e.g. 5 wt% MeOH with 1M KOH. This opens up the possibility not only for ionomer-free anodes with nanostructured catalysts without RH being a consideration, but potentially also for the development of ultra-thick anodes that are low-resistance when flooded, to increase the active band of electrocatalyst in a similar strategy to flow battery electrodes. Longer-term, in hydrogen fuel cell systems, bipolar membrane systems, where AEM and PEM interfacially adhered or otherwise blended to form a single membrane, offer the potential to pair the facile kinetics and highly developed acidic anode with the enhanced ORR activities and non-precious catalysts employable in the alkaline cathodes, together with a self-hydrating system for even greater back-diffusion attainable to the cathode catalyst layer.

Chapter 5 presented direct membrane deposition (DMD) onto electrodes as a method to reduce overall interfacial resistivity in fuel cells and allow easy integration of additives to any layer therein was adapted to conditions suitable for mass manufacture. As above, this construction is particularly desirable in the further development of electrodes with low precious metal contents, and the method itself can be further improved for this application – proof of concept work I conducted suggests the addition of a blocking layer reduced the penetration depth of cast membrane, making this method suitable for catalyst layers < 2 µm. Additionally, this construction allows additives (e.g. cerium oxide for radical scavenging or PTFE dispersion to enhance hydrophobicity) or supports (e.g. electrospun PVDF or PEEK) or custom, differentiated compositions to be added to any layer of the fuel cell – GDL, MPL, electrode, or membrane; furthermore, these compositions can be differentiated between anode and cathode. This could allow much more rapid and site-differentiated studies on the impacts to lifetime and stability fully hydrocarbon membranes and ionomer could achieve in PEMFCS.

DMD construction is also highly pertinent to the development of hydrogen AEMFCs in particular, where overall system stability is still a concern. Likely the high back-diffusion effected by DMDs is the origin of the significant stabilization found in initial proof-of-concept work, and DMD was the method recently employed on systems based on HMT-PMPI, a base material stable in 10M KOH at 100 °C.[281]

Altogether, as materials continue to be developed for PEMFC and AEMFCs and fully hydrocarbon ionomers move from the academy to industry, connecting the innate structure-property relations of ionomers to their interactions with electrocatalyst *in situ* remains highly pertinent to guide future materials discovery efforts, and the further investigation of the DMD constructions both to address significant challenges more difficult to address with other constructions and for its unprecedented ability to isolate variables for study in full MEAs.

References

(1) Gröger, O.; Gasteiger, H. a.; Suchsland, J.-P. *J. Electrochem. Soc.* **2015**, *162* (14), A2605–A2622.

(2) Vesborg, P. C. K.; Jaramillo, T. F. *RSC Adv.* **2012**, *2*, 7933.

(3) Atkinson, R. W.; Hazard, M. W.; Rodgers, J. A.; Stroman, R. O.; Gould, B. D. *J. Electrochem. Soc.* **2017**, *164* (2), F46–F54.

(4) van Biert, L.; Godjevac, M.; Visser, K.; Aravind, P. V. *J. Power Sources* **2016**, *327* (X), 345–364.

(5) Hickner, M. A.; Ghassemi, H.; Kim, Y. S.; Einsla, B. R.; Mcgrath, J. E.; Hickner, M. A.; Ghassemi, H.; Kim, Y. S.; Einsla, B. R.; Mcgrath, J. E. *Chem. Rev.* **2004**, *104* (10), 4587–4612.

(6) Ellamla, H. R.; Staffell, I.; Bujlo, P.; Pollet, B. G.; Pasupathi, S. *J. Power Sources* **2015**, *293*, 312–328.

(7) Giddey, S.; Ciacchi, F. T.; Badwal, S. P. S. *J. Power Sources* **2004**, *125* (2), 155–165.

(8) Dodds, P. E.; Staffell, I.; Hawkes, A. D.; Li, F.; Grünewald, P.; McDowall, W.; Ekins, P. *Int. J. Hydrogen Energy* **2015**, *40* (5), 2065–2083.

(9) Braunchweig, B.; Hibbitts, D.; Neurock, M.; Wieckowski, A. *Catal. Today* **2013**, *202*, 197–209.

(10) Zamel, N. *J. Power Sources* **2016**, *309*, 141–159.

(11) Kraytsberg, A.; Ein-Eli, Y. *Energy & Fuels* **2014**, *28* (12), 7303–7330.

(12) Merle, G.; Wessling, M.; Nijmeijer, K. *J. Memb. Sci.* **2011**, *377* (1–2), 1–35.

(13) Smith, M. J.; Irvine, J. T. S. In *The Economic Impact of Hydrogen and Fuel Cells in the UK – A Preliminary Assessment based on Analysis of the replacement of Refined Transport Fuels and Vehicles.*; Smith, M. J., Turner, K., Irvine, J. T. S., Eds.; H2FC SUPERGEN: London, 2017; pp 113–120.

(14) Haile, S. M. *Acta Mater.* **2003**, *51* (19), 5981–6000.

(15) Yoshida, T.; Kojima, K. *Interface Mag.* **2015**, *24* (2), 45–49.

(16) Carter, D.; Wing, J. *E4tech Reports* **2017**, 1–50.

(17) Kipf, E.; Erben, J.; Zengerle, R.; Gescher, J.; Kerzenmacher, S. *Bioresour. Technol. Reports* **2018**, #pagerange#.

(18) Bandodkar, A. J. *J. Electrochem. Soc.* **2017**, *164* (3), H3007–H3014.

(19) Ran, J.; Wu, L.; He, Y.; Yang, Z.; Wang, Y.; Jiang, C.; Ge, L.; Bakangura, E.; Xu, T. *J. Memb. Sci.* **2017**, *522*, 267–291.

(20) Ahlfield, J. M.; Liu, L.; Kohl, P. A. *J. Electrochem. Soc.* **2017**, *164* (12), F1165–F1171.

(21) Araya, S. S.; Zhou, F.; Liso, V.; Sahlin, S. L.; Vang, J. R.; Thomas, S.; Gao, X.; Jeppesen, C.; K??r, S. K. *Int. J. Hydrogen Energy* **2016**, *41* (46), 21310–21344.

(22) Hutzenlaub, T.; Becker, J.; Zengerle, R.; Thiele, S. *J. Power Sources* **2013**, *227*, 260–266.

(23) Li, H.; Tang, Y.; Wang, Z.; Shi, Z.; Wu, S.; Song, D.; Zhang, J. J. J.; Fatih, K.; Zhang, J. J. J.; Wang, H.; Liu, Z.; Abouatallah, R.; Mazza, A. *J. Power Sources* **2008**, *178* (1), 103–117.

(24) Schmidt, T. J.; Grgur, B. N.; Gasteiger, H. A.; Behm, R. J.; Ross, P. N. *J. Phys. Chem. B* **1999**, *103* (40), 8568–8577.

(25) Hickner, M. a.; Herring, A. M.; Coughlin, E. B. *J. Polym. Sci. Part B Polym. Phys.* **2013**, *51* (24), 1727–1735.

(26) St. John, S.; Atkinson, R. W.; Roy, A. L.; Unocic, R. R.; Papandrew, A. B.; Zawodzinski, T. A.; Papandrew, B.; Zawodzinski, T. A. *ECS Trans.* **2015**, *69* (17), 995–1005.

(27) Bai, J.; Zhu, Q.; Lv, Z.; Dong, H.; Yu, J.; Dong, L. *Int. J. Hydrogen Energy* **2013**, *38* (3), 1413–1418.

(28) Subbaraman, R.; Danilovic, N.; Lopes, P. P.; Tripkovic, D.; Strmcnik, D.; Stamenkovic, V. R.; Markovic, N. M. *J. Phys. Chem. C* **2012**, *116*, 22231–22237.

(29) Wang, Z.; Boucher, J. M.; Scheringer, M.; Cousins, I. T.; Hungerbühler, K. *Environ. Sci. Technol.* **2017**, *51* (8), 4482–4493.

(30) Peckham, T. J.; Schmeisser, J.; Holdcroft, S. *J. Phys. Chem. B* **2008**, *112* (10), 2848–2858.

(31) Kreuer, K.-D. *Chem. Mater.* **2014**, *26* (1), 361–380.

(32) Li, N.; Guiver, M. D. *Macromolecules* **2014**, *47* (7), 2175–2198.

(33) Tsang, E. M. W.; Zhang, Z.; Shi, Z.; Soboleva, T.; Holdcroft, S. **2007**, No. Ii, 95–98.

(34) Rezaei Niya, S. M.; Hoorfar, M. *J. Power Sources* **2013**, *240*, 281–293.

(35) Luo, X.; Holdcroft, S.; Mani, A.; Zhang, Y.; Shi, Z. *Phys. Chem. Chem. Phys.* **2011**, *13* (40), 18055–18062.

(36) Kim, Y. S.; Pivovar, B. S. *J. Electrochem. Soc.* **2010**, *157* (11), B1616.

(37) Naudy, S.; Collette, F.; Thominette, F.; Gebel, G.; Espuche, E. *J. Memb. Sci.* **2014**, *451*, 293–304.

(38) Kusoglu, A.; Kwong, A.; Clark, K. T.; Gunterman, H. P.; Weber, A. Z. *J. Electrochem. Soc.* **2012**, *159* (9), F530–F535.

(39) Zhao, Q.; Majsztrik, P.; Benziger, J. *J. Phys. Chem. B* **2011**, *115* (12), 2717–2727.

(40) Dang, Q. K.; Henkensmeier, D.; Krishnan, N. N.; Jang, J. H.; Kim, H.-J.; Nam, S. W.; Lim, T.-H. *J. Memb. Sci.* **2014**, *460*, 199–205.

(41) Peron, J.; Mani, A.; Zhao, X.; Edwards, D.; Adachi, M.; Soboleva, T.; Shi, Z.; Xie, Z.; Navessin, T.; Holdcroft, S. *J. Memb. Sci.* **2010**, *356* (1–2), 44–51.

(42) Weissbach, T.; Peckham, T. J.; Holdcroft, S. *J. Memb. Sci.* **2016**, *498*, 94–104.

(43) Macauley, N.; Ghassemzadeh, L.; Lim, C.; Watson, M.; Kolodziej, J.; Lauritzen, M.; Holdcroft, S.; Kjeang, E. *ECS Electrochem. Lett.* **2013**, *2* (4), F33–F35.

(44) Macauley, N.; Wong, K. H.; Watson, M.; Kjeang, E.; Hung, K.; Watson, M.; Kjeang, E.; Wong, K. H.; Watson, M.; Kjeang, E. *J. Power Sources* **2015**, *299*, 139–148.

(45) Kim, Y. S.; Welch, C. F.; Hjelm, R. P.; Mack, N. H.; Labouriau, A.; Orler, E. B. *Macromolecules* **2015**, *48* (7), 2161–2172.

(46) Kusoglu, A.; Weber, A. Z. *Chem. Rev.* **2017**, *117* (3), 987–1104.

(47) Ishikawa, H.; Teramoto, T.; Ueyama, Y.; Sugawara, Y.; Sakiyama, Y.; Kusakabe, M.; Miyatake, K.; Uchida, M. *J. Power Sources* **2016**, *325*, 35–41.

(48) Malek, K.; Mashio, T.; Eikerling, M. *Electrocatalysis* **2011**, *2* (2), 141–157.

(49) Kolde, J. A.; Bahar, B. *Electrochem. Soc. Proc.* **1995**, *95–23*, 193–201.

(50) Goulet, M. A.; Arbour, S.; Lauritzen, M.; Kjeang, E. *J. Power Sources* **2015**, *274*, 94–100.

(51) Sarode, H. N.; Yang, Y.; Motz, A. R.; Li, Y.; Knauss, D. M.; Seifert, S.; Herring, A. M. *J. Phys. Chem. C* **2017**, *121*, 2035–2045.

(52) Soboleva, T.; Zhao, X.; Malek, K.; Xie, Z.; Navessin, T.; Holdcroft, S. *ACS Appl. Mater. Interfaces* **2010**, *2* (2), 375–384.

(53) Soboleva, T.; Malek, K.; Xie, Z.; Navessin, T.; Holdcroft, S. *ACS Appl. Mater. Interfaces* **2011**, *3* (6), 1827–1837.

(54) El Hannach, M.; Soboleva, T.; Malek, K.; Franco, A. A.; Prat, M.; Pauchet, J.; Holdcroft, S. *J. Power Sources* **2014**, *247*, 322–326.

(55) Dekel, D. R.; Willdorf, S.; Ash, U.; Amar, M.; Pusara, S.; Dhara, S.; Srebnik, S.; Diesendruck, C. E. The critical relation between chemical stability of cations and water in anion exchange membrane fuel cells environment. *Journal of Power Sources*, 2017.

(56) Santiago, E. I.; Isidoro, R. A.; Dresch, M. A.; Matos, B. R.; Linardi, M.; Fonseca, F. C. *Electrochim. Acta* **2009**, *54* (16), 4111–4117.

(57) Amjadi, M.; Rowshanzamir, S.; Peighambardoust, S. J.; Sedghi, S. *J. Power Sources* **2012**, *210*, 350–357.

(58) Matos, B. R.; Santiago, E. I.; Fonseca, F. C. *Mater. Renew. Sustain. Energy* **2015**, *4* (4), 1–9.

(59) Sadeghi Alavijeh, A.; Khorasany, R. M. H.; Habisch, A.; Wang, G. G.; Kjeang, E. *J. Power Sources* **2015**, *285*, 16–28.

(60) Raamat, E.; Kaupmees, K.; Ovsjannikov, G.; Trummal, A.; Kütt, A.; Saame, J.; Koppel, I.; Kaljurand, I.; Lipping, L.; Rodima, T.; Pihl, V.; Koppel, I. A.; Leito, I. *J. Phys. Org. Chem.* **2013**, *26* (2), 162–170.

(61) George, M. G.; Liu, H.; Muirhead, D.; Banerjee, R.; Ge, N.; Shrestha, P.; Lee, J.; Chevalier, S.; Hinebaugh, J.; Messerschmidt, M.; Zeis, R.; Scholta, J.; Bazylak, A. *J. Electrochem. Soc.* **2017**, *164* (7), F714–F721.

(62) Jahnke, T.; Futter, G.; Latz, A.; Malkow, T.; Papakonstantinou, G.; Tsotridis, G.; Schott, P.; Gérard, M.; Quinaud, M.; Quiroga, M.; Franco, A. A.; Malek, K.; Calle-Vallejo, F.; Ferreira De Morais, R.; Kerber, T.; Sautet, P.; Loffreda, D.; Strahl, S.; Serra, M.; Polverino, P.; Pianese, C.; Mayur, M.; Bessler, W. G.; Kompis, C. *J. Power Sources* **2016**, *304*, 207–233.

(63) Cherevko, S.; Keeley, G. P.; Geiger, S.; Zeradjanin, A. R.; Hodnik, N.; Kulyk, N.; Mayrhofer, K. J. J. *ChemElectroChem* **2015**, *2* (10), 1471–1478.

(64) Helmly, S.; Eslamibidgoli, M. J.; Friedrich, K. A.; Eikerling, M. H. *Electrocatalysis* **2017**, 24–31.

(65) Hickner, M. A. *Mater. Today* **2010**, *13* (5), 34–41.

(66) Babanova, S.; Carpenter, K.; Phadke, S.; Suzuki, S.; Ishii, S.; Phan, T.; Grossi-Soyster, E.; Flynn, M.; Hogan, J.; Bretschger, O. *J. Electrochem. Soc.* **2017**, *164* (3), H3015–H3023.

(67) Mench, M. M.; Kumbur, E. C.; Veziroglu, T. N. *Polymer Electrolyte Fuel Cell Degradation*; Elsevier Academic Press: Oxford, 2012.

(68) Peron, J.; Shi, Z.; Holdcroft, S. *Energy Environ. Sci.* **2011**, *4* (5), 1575.

(69) Miyatake, K.; Hirayama, D.; Bae, B.; Watanabe, M. *Polym. Chem.* **2012**, *3* (9), 2517.

(70) Ng, F.; Bae, B.; Miyatake, K.; Watanabe, M. *Chem. Commun.* **2011**, *47* (31), 8895.

(71) Bae, B.; Hoshi, T.; Miyatake, K.; Watanabe, M. *Macromolecules* **2011**, *44* (10), 3884–3892.

(72) Danyliv, O.; Gueneau, C.; Iojoiu, C.; Cointeaux, L.; Thiam, A.; Lyonnard, S.; Sanchez, J. Y. *Electrochim. Acta* **2016**, *214*, 182–191.

(73) Danyliv, O.; Iojoiu, C.; Barbier, V.; Martin, V.; Sanchez, J. Y. *J. Fluor. Chem.* **2016**, *189*, 43–50.

(74) Park, C. H.; Lee, S. Y.; Hwang, D. S.; Shin, D. W.; Cho, D. H.; Lee, K. H.; Kim, T.-W.; Kim, T.-W.; Lee, M.; Kim, D.-S.; Doherty, C. M.; Thornton, A. W.; Hill, A. J.; Guiver, M. D.; Lee, Y. M. *Nature* **2016**, *532* (7600), 480–483.

(75) Miyatake, K.; Furuya, H.; Tanaka, M.; Watanabe, M. *J. Power Sources* **2012**, *204*, 74–78.

(76) Lee, H.-F.; Britton, B.; Huang, Y.-C.; Peckham, T. J.; Hsu, Y.-Y.; Tseng, Y.-C.; Huang, P.-C.; Lee, C.-C.; Chang, M.-Y.; Holdcroft, S.; Huang, W.-Y. *J. Mater. Sci.* **2016**.

(77) Si, K.; Wycisk, R.; Dong, D.; Cooper, K.; Rodgers, M.; Brooker, P.; Slattery, D.; Litt, M. *Macromolecules* **2013**, *46*, 422–433.

(78) Mochizuki, T.; Uchida, M.; Miyatake, K. *ACS Energy Lett.* **2016**, *1* (2), 348–352.

(79) Oshima, T.; Yoshizawa-Fujita, M.; Takeoka, Y.; Rikukawa, M. *ACS Omega* **2016**, *1* (5), 939–942.

(80) Adamski, M.; Skalski, T. J. G.; Britton, B.; Peckham, T. J.; Metzler, L.; Holdcroft, S. *Angew. Chemie* **2017**.

(81) Skalski, T. J. G.; Britton, B.; Peckham, T. J.; Holdcroft, S. *J. Am. Chem. Soc.* **2015**, *137* (38).

(82) Agel, E.; Bouet, J.; Fauvarque, J. F. *J. Power Sources* **2001**, *101* (2), 267–274.

(83) Gottesfeld, S.; Dekel, D. R.; Page, M.; Bae, C.; Yan, Y.; Zelenay, P.; Kim, Y. S. Anion exchange membrane fuel cells: Current status and remaining challenges. *Journal of Power Sources*, 2017.

(84) Varcoe, J. R.; Atanassov, P.; Dekel, D. R.; Herring, A. M.; Hickner, M. A.; Kohl, P. A.; Kucernak, A. R.; Mustain, W. E.; Nijmeijer, K.; Scott, K.; Xu, T.; Zhuang, L. *Energy Environ. Sci.* **2014**, *7*, 3135–3191.

(85) Knauth, P.; Pasquini, L.; Di Vona, M. L. *Solid State Ionics* **2017**, *300*, 97–105.

(86) Pivovar, B. S.; Kim, Y. S.; Hickner, M. A.; Spendlowe, J.; Weber, A. Z.; Arges, C. G.; Serov, A.; Neyerlin, K. C. *2016 Alkaline Membrane Fuel Cell Workshop*; 2016.

(87) Dekel, D. R.; Willdorf, S.; Ash, U.; Amar, M.; Pusara, S.; Dhara, S.; Srebnik, S.; Diesendruck, C. E. *J. Power Sources* **2017**, *375*, 351–360.

(88) Wright, A. G.; Fan, J.; Britton, B.; Weissbach, T.; Lee, H.-F.; Kitching, E. A.; Peckham, T. J.; Holdcroft, S. *Energy Environ. Sci.* **2016**, *9* (6), 2130–2142.

(89) Ertem, S. P.; Caire, B. R.; Tsai, T.-H.; Zeng, D.; Vandiver, M. A.; Kusoglu, A.; Seifert, S.; Hayward, R. A.; Weber, A. Z.; Herring, A. M.; Coughlin, E. B.; Liberatore, M. W. *J. Memb. Sci.* **2016**, No. submitted, 1–11.

(90) Mohanty, A. D.; Ryu, C. Y.; Kim, Y. S.; Bae, C. *Macromolecules* **2015**, *48* (19), 7085–7095.

(91) Biesheuvel, P. M.; Franco, A. a.; Bazant, M. Z. *J. Electrochem. Soc.* **2009**, *156* (2), B225.

(92) Spingler, F. B.; Phillips, A.; Schuler, T.; Tucker, M. C.; Weber, A. Z. *Int. J. Hydrogen Energy* **2017**, *42* (19), 13960–13969.

(93) Schmickler, W.; Santos, E. *Interfacial Electrochemistry, 2nd Ed.*; Springer-Verlag: Berlin, Heidelberg, 2010.

(94) Orfanidi, A.; Madkikar, P.; El-Sayed, H. A.; Harzer, G. S.; Kratky, T.; Gasteiger, H. A. *J. Electrochem. Soc.* **2017**, *164* (4), 418–426.

(95) Mamlouk, M.; Scott, K.; Horsfall, J. A.; Williams, C. *Int. J. Hydrogen Energy* **2011**, *36* (12), 7191–7198.

(96) Litster, S.; McLean, G. *J. Power Sources* **2004**, *130* (1–2), 61–76.

(97) Saha, M. S., Tam M., Berejnov V., Susac D., McDermid S., Hitchcock A., S. J. *ECS Trans. 58 797-806* **2013**, *58* (1), 797–806.

(98) Sassin, M. B.; Garsany, Y.; Gould, B. D.; Swider-Lyons, K. E. *Anal. Chem.* **2017**, *89* (1), 511–518.

(99) Akhgar, A.; Losier, V.; Putz, A.; Djilali, N. In *CaRPE-FC 2016*; 2016.

(100) Holdcroft, S. *Chem. Mater.* **2014**, *26* (1), 381–393.

(101) Singh, R.; Akhgar, A. R.; Sui, P. C.; Lange, K. J.; Djilali, N. *J. Electrochem. Soc.* **2014**, *161* (4), F415–F424.

(102) Thiele, S.; Zengerle, R.; Ziegler, C. *Nano Res.* **2011**, *4* (9), 849–860.

(103) Hegge, F.; Moroni, R.; Trinke, P.; Bensmann, B.; Hanke-Rauschenbach, R.; Thiele, S.; Vierrath, S. *J. Power Sources* **2018**, *393* (January), 62–66.

(104) Weber, a. Z.; Borup, R. L.; Darling, R. M.; Das, P. K.; Dursch, T. J.; Gu, W.; Harvey, D.; Kusoglu, A.; Litster, S.; Mench, M. M.; Mukundan, R.; Owejan, J. P.; Pharoah, J. G.; Secanell, M.; Zenyuk, I. V. *J. Electrochem. Soc.* **2014**, *161* (12), F1254–F1299.

(105) Sassin, M. B.; Garsany, Y.; Gould, B. D.; Swider-Lyons, K. *J. Electrochem. Soc.* **2016**, *163* (8), F808–F815.

(106) Antolini, E. *Appl. Catal. B Environ.* **2016**, *181*, 298–313.

(107) Xie, X.; Zhang, G.; Zhou, J.; Jiao, K. *Int. J. Hydrogen Energy* **2017**, *42* (17), 12521–12530.

(108) Schmittinger, W.; Vahidi, A. *J. Power Sources* **2008**, *180* (1), 1–14.

(109) Pistono, A.; Rice, C. A. *J. Electrochem. Soc.* **2017**, *164* (6), F582–F590.

(110) Eikerling, M. *J. Electrochem. Soc.* **2006**, *153* (3), E58–E70.

(111) Ban, S.; Malek, K.; Huang, C.; Liu, Z. *Carbon N. Y.* **2011**, *49* (10), 3362–3370.

(112) Trogadas, P.; Fuller, T. F.; Strasser, P. *Carbon N. Y.* **2014**, *75*, 5–42.

(113) Zhang, Z.; Han, S.; Wang, C.; Li, J.; Xu, G. *Nanomaterials* **2015**, *5* (4), 1732–1755.

(114) Sharma, S.; Pollet, B. G. *J. Power Sources* **2012**, *208*, 96–119.

(115) Zhang, Y.; Zhao, L.; Walton, J.; Liu, Z.; Tang, Z. *Int. J. Hydrogen Energy* **2017**, *42* (27), 17112–17121.

(116) Huang, S.-Y.; Ganesan, P.; Popov, B. N. *Appl. Catal. B Environ.* **2011**, *102* (1–2), 71–77.

(117) James, B. D.; Baum, K. N.; Spisak, A. B. **2012**, No. September.

(118) Debe, M. K. *Nature* **2012**, *486* (7401), 43–51.

(119) Kriston, Á.; Xie, T.; Gamliel, D.; Ganesan, P.; Popov, B. N. *J. Power Sources* **2013**, *243*, 958–963.

(120) Shao, M.; Chang, Q.; Dodelet, J.-P.; Chenitz, R. *Chem. Rev.* **2016**, *116* (6), 3594–3657.

(121) Kongkanand, A.; Mathias, M. F. *J. Phys. Chem. Lett.* **2016**, *7* (7), 1127–1137.

(122) Lv, H.; Li, D.; Strmcnik, D.; Paulikas, A. P.; Markovic, N. M.; Stamenkovic, V. R. *Nano Energy* **2016**, *29*, 149–165.

(123) Lu, Y.; Du, S.; Steinberger-Wilckens, R. *Appl. Catal. B Environ.* **2016**, *199*, 292–

314.

(124) Huang, J.; Li, Z.; Zhang, J. *Front. Energy* **2017**, *11* (3), 334–364.

(125) DeBonis, D.; Mayer, M.; Omosebi, A.; Besser, R. S. *Renew. Energy* **2016**, *89*, 200–206.

(126) Park, J. S.; Krishnan, P.; Park, S. H.; Park, G. G.; Yang, T. H.; Lee, W. Y.; Kim, C. S. *J. Power Sources* **2008**, *178* (2), 642–650.

(127) Klingele, M.; Breitwieser, M.; Zengerle, R.; Thiele, S. *J. Mater. Chem. A* **2015**, *3* (c), 11239–11245.

(128) Nonoyama, N.; Okazaki, S.; Weber, A. Z.; Ikogi, Y.; Yoshida, T. *J. Electrochem. Soc.* **2011**, *158* (4), B416.

(129) Weber, A. Z.; Kusoglu, A. *J. Mater. Chem. A* **2014**, *2* (c).

(130) Page, K. A.; Kusoglu, A.; Stafford, C. M.; Kim, S.; Kline, R. J.; Weber, A. Z. *Nano Lett.* **2014**, *14* (5), 2299–2304.

(131) Freiberg, A. T. S.; Tucker, M. C.; Weber, A. Z. *Electrochem. commun.* **2017**, *79* (March), 14–17.

(132) Kusoglu, A.; Weber, A. Z. *Chem. Rev.* **2017**, *117* (3), 987–1104.

(133) Kongkanand, A.; Subramanian, N. P.; Yu, Y.; Liu, Z.; Igarashi, H.; Muller, D. A. *ACS Catal.* **2016**, acscatal.5b02819.

(134) Editor, S.; Lockwood, D. J.; Ozoemena, K. I. *Nanomaterials for Fuel Cell Catalysis*; Ozeoemena, K. I., Chen, S., Eds.; Springer International Publishing Switzerland, 2016.

(135) Cho, Y. H. Y. H. Y.; Jeon, T. Y.; Lim, J. W.; Cho, Y. H. Y. H. Y.; Ahnb, M.; Jung, N.; Yoo, S. J.; Yoon, W. S.; Sung, Y. E.; Wan, J.; Cho, Y. H. Y. H. Y.; Ahnb, M.; Jung, N.; Jong, S.; Yoon, W. S.; Sung, Y. E. *Int. J. Hydrogen Energy* **2011**, *36* (7), 4394–4399.

(136) Banham, D.; Kishimoto, T.; Sato, T.; Kobayashi, Y.; Narizuka, K.; Ozaki, J. ichi;

Zhou, Y.; Marquez, E.; Bai, K.; Ye, S. *J. Power Sources* **2017**, *344*, 39–45.

(137) Stariha, S.; Artyushkova, K.; Workman, M. J.; Serov, A.; Mckinney, S.; Halevi, B.; Atanassov, P. *J. Power Sources* **2016**, *326*, 43–49.

(138) Serov, A.; Kwak, C. *Appl. Catal. B Environ.* **2009**, *90* (3–4), 313–320.

(139) Banham, D.; Ye, S.; Pei, K.; Ozaki, J.; Kishimoto, T.; Imashiro, Y. *J. Power Sources* **2015**, *285*, 334–348.

(140) Klingele, M.; Pham, C.; Vuyyuru, K. R.; Britton, B.; Holdcroft, S.; Fischer, A.; Thiele, S. *Electrochem. commun.* **2017**, *77*, 71–75.

(141) Saha, M. S.; Gullá, A. F.; Allen, R. J.; Mukerjee, S. *Electrochim. Acta* **2006**, *51* (22), 4680–4692.

(142) Martin, S.; Garcia-Ybarra, P. L.; Castillo, J. L.; Garcia-Ybarra, P. L.; Castillo, J. L. *Int. J. Hydrogen Energy* **2010**, *35* (19), 10446–10451.

(143) Martin, S.; Martinez-Vazquez, B.; Garcia-Ybarra, P. L.; Castillo, J. L.; Martinez-Vazquez, B.; Garcia-Ybarra, P. L.; Castillo, J. L. *J. Power Sources* **2013**, *229* (2013), 179–184.

(144) Breitwieser, M.; Klingele, M.; Britton, B.; Holdcroft, S.; Zengerle, R.; Thiele, S. *Electrochem. commun.* **2015**, *60*, 168–171.

(145) Meyers, J. P.; Mcgrath, J. E.; Borup, R.; Meyers, J.; Pivovar, B.; Kim, Y. S.; Mukundan, R.; Garland, N.; Myers, D.; Wilson, M.; Garzon, F.; Wood, D.; Zelenay, P.; More, K.; Stroh, K.; Zawodzinski, T.; Boncella, X. J.; Mcgrath, J. E.; Inaba, O. M.; Miyatake, K.; Hori, M.; Ota, K.; Ogumi, Z.; Miyata, S.; Nishikata, A.; Siroma, Z.; Uchimoto, Y. **2007**, *107* (NOVEMBER), 3904–3951.

(146) Banerjee, R.; Ge, N.; Lee, J.; George, M. G.; Chevalier, S.; Liu, H.; Shrestha, P.; Muirhead, D.; Bazylak, A. *J. Electrochem. Soc.* **2017**, *164* (2), 22–25.

(147) Wright, A. G.; Fan, J.; Britton, B.; Weissbach, T.; Lee, H.-F.; Kitching, E. A.; Peckham, T. J.; Holdcroft, S. *Energy Environ. Sci.* **2016**, *9*, 2130–2142.

(148) Ong, A. L.; Inglis, K. K.; Whelligan, D. K.; Murphy, S.; Varcoe, J. R. *Phys. Chem. Chem. Phys.* **2015**, *17* (18), 12135–12145.

(149) Hancock, C. a; Ong, A. L.; Varcoe, J. R. *RSC Adv.* **2014**, *4* (57), 30035.

(150) Smith, M.; Cooper, K.; Johnson, D.; Scribner, L. *Fuel Cell* **2005**, *3* (3).

(151) Petrone, R.; Hissel, D.; Péra, M. C.; Chamagne, D.; Gouriveau, R. *Int. J. Hydrogen Energy* **2015**, *40* (36), 12489–12505.

(152) Lim, C.; Ghassemzadeh, L.; Van Hove, F.; Lauritzen, M.; Kolodziej, J.; Wang, G. G.; Holdcroft, S.; Kjeang, E. *J. Power Sources* **2014**, *257*, 102–110.

(153) Lai, Y.-H.; Rahmoeller, K. M.; Hurst, J. H.; Kukreja, R. S.; Atwan, M.; Maslyn, A. J.; Gittleman, C. S. *J. Electrochem. Soc.* **2018**, *165* (6), F3217–F3229.

(154) Ous, T.; Arcoumanis, C. *J. Power Sources* **2013**, *240*, 558–582.

(155) Minke, C.; Turek, T. *J. Power Sources* **2015**, *286*, 247–257.

(156) Izuhara, D.; Umeda, H.; Ito, Y.; Shintaku, Y.; Adachi, S. *Meet. Abstr.* **2014**, *MA2014-02* (21), 1059.

(157) Umeda, H.; Adachi, S.; Izuhara, D. *ECS Meet. Abstr.* **2016**, *MA2016-02* (38), 2608.

(158) Okanishi, T.; Tsuji, Y.; Sakiyama, Y.; Matsuno, S.; Bae, B.; Miyatake, K.; Uchida, M.; Watanabe, M. *Electrochim. Acta* **2011**, *56* (24), 8989–8996.

(159) Okanishi, T.; Yoda, T.; Sakiyama, Y.; Miyahara, T.; Miyatake, K.; Uchida, M.; Watanabe, M. *Electrochem. commun.* **2012**, *24*, 47–49.

(160) Ishikawa, H.; Fujita, Y.; Tsuji, J.; Kusakabe, M.; Miyake, J.; Sugawara, Y.; Miyatake, K.; Uchida, M. *J. Electrochem. Soc.* **2017**, *164* (12), F1204–F1210.

(161) Miyake, J.; Kusakabe, M.; Tsutsumida, A.; Miyatake, K. *ACS Appl. Energy Mater.* **2018**, acsaem.7b00349.

(162) Skalski, T. J. G. T. J. G. T. J. G.; Britton, B.; Peckham, T. J. T. J. T. J.; Holdcroft, S. *J. Am. Chem. Soc.* **2015**, *137* (38), 12223–12226.

(163) Garrick, T. R.; Moylan, T. E.; Yarlagadda, V.; Kongkanand, A. *J. Electrochem. Soc.* **2017**, *164* (2), F60–F64.

(164) Albery, W. J.; Elliott, C. M.; Mount, A. R. *J. Electroanal. Chem. Interfacial Electrochem.* **1990**, *288* (1–2), 15–34.

(165) Li, G.; Pickup, P. G. *J. Electrochem. Soc.* **2003**, *150* (11), C745.

(166) Paul, D. K.; Karan, K.; Docoslis, A.; Giorgi, J. B.; Pearce, J. *Macro* **2013**, *46*, 3461–3475.

(167) Lei, C.; Bessarabov, D.; Ye, S.; Xie, Z.; Holdcroft, S.; Navessin, T. *J. Power Sources* **2011**, *196* (15), 6168–6176.

(168) Butt, H.-J.; Graf, K.; Kappl, M. *Physics and Chemistry of Interfaces*; Wiley-VCH Verlag GmbH & Co.: Weinheim, Germany, 2003.

(169) Page, K. A.; Kusoglu, A.; Sta, C. M.; Kim, S.; Kline, R. J.; Weber, A. Z. **2014**.

(170) Okumura, M.; Noda, Z.; Matsuda, J.; Tachikawa, Y.; Nishihara, M.; Lyth, S. M.; Hayashi, A.; Sasaki, K. *J. Electrochem. Soc.* **2017**, *164* (9), 928–934.

(171) Takahashi, K.; Kakinuma, K.; Uchida, M. *J. Electrochem. Soc.* **2016**, *163* (10), F1182–F1188.

(172) Jung, C. Y.; Kim, S. K.; Lee, S. J.; Yi, S. C. *Electrochim. Acta* **2016**, *211*, 142–147.

(173) Ohira, A.; Kuroda, S.; Mohamed, H. F. M.; Tavernier, B. *Phys. Chem. Chem. Phys.* **2013**, *15* (27), 11494.

(174) Kusoglu, A.; Dursch, T. J.; Weber, A. Z. *Adv. Funct. Mater.* **2016**, *26* (27), 4961–4975.

(175) Tesfaye, M.; MacDonald, A. N.; Dudenas, P. J.; Kusoglu, A.; Weber, A. Z. *Electrochem. commun.* **2018**, *87* (November 2017), 86–90.

(176) Modestino, M. a; Paul, D. K.; Dishari, S.; Petrina, S. a; Allen, F. I.; Hickner, M. a; Karan, K.; Segalman, R. a; Weber, A. Z. *Macromolecules* **2013**, *46*, 867–873.

(177) Xie, J.; More, K. L.; Zawodzinski, T. a.; Smith, W. H. *J. Electrochem. Soc.* **2004**, *151* (11), A1841.

(178) Xie, Z.; Navessin, T.; Shi, K.; Chow, R.; Wang, Q.; Song, D.; Andreaus, B.; Eikerling, M.; Liu, Z.; Holdcroft, S. *J. Electrochem. Soc.* **2005**, *152*, A1171.

(179) Gode, P.; Jaouen, F.; Lindbergh, G.; Lundblad, A.; Sundholm, G. *Electrochim. Acta* **2003**, *48* (28), 4175–4187.

(180) Passalacqua, E.; Lufrano, F.; Squadrito, G.; Patti, a.; Giorgi, L. *Electrochim. Acta* **2001**, *46* (6), 799–805.

(181) Breitwieser, M.; Klingele, M.; Vierrath, S.; Zengerle, R.; Thiele, S. *Adv. Energy Mater.* **2017**, *1701257*.

(182) Yang, D.; Yu, H.; Li, G.; Zhao, Y.; Liu, Y.; Zhang, C.; Song, W.; Shao, Z. *J. Power Sources* **2014**, *267*, 39–47.

(183) Strong, A.; Britton, B.; Edwards, D.; Peckham, T. J.; Lee, H.-F.; Huang, W. Y.; Holdcroft, S. *J. Electrochem. Soc.* **2015**, *162* (6), F513–F518.

(184) Peckham, T. J.; Holdcroft, S. *Adv. Mater.* **2010**, *22* (42), 10488.

(185) Park, C. H.; Lee, C. H.; Guiver, M. D.; Lee, Y. M. *Prog. Polym. Sci.* **2011**, *36* (11), 1443–1498.

(186) Zhang, S. S.; Yuan, X.-Z. Z.; Hin, J. N. C.; Wang, H. J.; Friedrich, K. A.; Schulze, M. *J. Power Sources* **2009**, *194* (2), 588–600.

(187) Peron, J.; Edwards, D.; Besson, A.; Shi, Z.; Holdcroft, S. *J. Electrochem. Soc.* **2010**, *157* (8), B1230.

(188) von Kraemer, S.; Puchner, M.; Jannasch, P.; Lundblad, A.; Lindbergh, G. *J. Electrochem. Soc.* **2006**, *153* (11), A2077.

(189) Carter, R.; Wycisk, R.; Yoo, H.; Pintauro, P. N. *Electrochem. Solid-State Lett.* **2002**, *5* (9), A195.

(190) Jorrissen, L.; Gogel, V.; Kerres, J.; Garche, J. *J. Power Sources* **2002**, *105* (2),

267–273.

(191) Kim, Y. S.; Kim, D. S.; Liu, B.; Guiver, M. D.; Pivovar, B. S. *J. Electrochem. Soc.* **2008**, *155* (1), B21.

(192) Wiles, K. B.; de Diego, C. M.; de Abajo, J.; McGrath, J. E. *J. Memb. Sci.* **2007**, *294* (1–2), 22–29.

(193) Huang, W. Y.; Chang, M. Y.; Han, Y. K.; Huang, P. T. *J. Polym. Sci. Part A Polym. Chem.* **2010**, *48* (24), 5872–5884.

(194) Adjemian, K. T.; Srinivasan, S.; Benziger, J.; Bocarsly, A. B. *J. Power Sources* **2002**, *109*, 356–364.

(195) Bae, B.; Miyatake, K.; Uchida, M.; Uchida, H.; Sakiyama, Y.; Okanishi, T.; Watanabe, M. *ACS Appl. Mater. Interfaces* **2011**, *3* (7), 2786–2793.

(196) Zhang, L.; Mukerjee, S. *J. Electrochem. Soc.* **2006**, *153* (6), A1062.

(197) Miyatake, K.; Chikashige, Y.; Higuchi, E.; Watanabe, M. *J. Am. Chem. Soc.* **2007**, *129* (13), 3879–3887.

(198) Gagnon, E.; Maris, T.; Arseneault, P. M.; Maly, K. E.; Wuest, J. D. *Cryst. Growth Des.* **2010**, *10* (2), 648–657.

(199) Lee, H.-F.; Wang, P.-H.; Huang, Y.-C.; Su, W.-H.; Gopal, R.; Lee, C. C.; Holdcroft, S.; Huang, W.-Y. *J. Polym. Sci. Part A Polym. Chem.* **2014**, *52* (18), 2579–2587.

(200) White, R. P.; Lipson, J. E. G. *Macromolecules* **2014**, *47* (12), 3959–3968.

(201) Bae, B.; Miyatake, K.; Watanabe, M. *ACS Appl. Mater. Interfaces* **2009**, *1* (6), 1279–1286.

(202) Bae, B.; Yoda, T.; Miyatake, K.; Uchida, M.; Uchida, H.; Watanabe, M. *J. Phys. Chem. B* **2010**, *114* (32), 10481–10487.

(203) Bae, B.; Yoda, T.; Miyatake, K.; Uchida, H.; Watanabe, M. *Angew. Chemie - Int. Ed.* **2010**, *49* (2), 317–320.

(204) Ng, F.; Bae, B.; Miyatake, K.; Watanabe, M. *Chem. Commun. (Camb).* **2011**, *47* (31), 8895–8897.

(205) Welch, C.; Labouriau, A.; Hjelm, R.; Orler, B.; Johnston, C.; Kim, Y. S. *ACS Macro Lett.* **2012**, *1* (12), 1403–1407.

(206) Kim, Y. S.; Welch, C. F.; Mack, N. H.; Hjelm, R. P.; Orler, E. B.; Hawley, M. E.; Lee, K. S.; Yim, S.-D.; Johnston, C. M. *Phys. Chem. Chem. Phys.* **2014**, *16* (13), 5927.

(207) Sood, R.; Iojoiu, C.; Espuche, E.; Gouanve, F.; Gebel, G.; Mendil-Jakani, H.; Lyonnard, S.; Jestin, J. *J. Phys. Chem. C* **2014**, *118* (26), 14157–14168.

(208) Moore, R. B.; Martin, C. R. *Macromolecules* **1988**, *21*, 1334–1339.

(209) Astill, T.; Xie, Z.; Shi, Z.; Navessin, T.; Holdcroft, S. *J. Electrochem. Soc.* **2009**, *156* (4), B499.

(210) Havránek, a.; Wippermann, K. *J. Electroanal. Chem.* **2004**, *567* (2), 305–315.

(211) Malek, K.; Eikerling, M.; Wang, Q.; Liu, Z.; Otsuka, S.; Akizuki, K.; Abe, M. *J. Chem. Phys.* **2008**, *129* (20).

(212) Rodgers, M. P.; Shi, Z.; Holdcroft, S. *J. Memb. Sci.* **2008**, *325* (1), 346–356.

(213) Sambandam, S.; Parrondo, J.; Ramani, V. *Phys. Chem. Chem. Phys.* **2013**, *15* (36), 14994–15002.

(214) Sambandam, S.; Ramani, V. *Phys. Chem. Chem. Phys.* **2010**, *12* (23), 6140.

(215) Peron, J.; Edwards, D.; Besson, A.; Shi, Z.; Holdcroft, S. *J. Electrochem. Soc.* **2010**, *157* (8), B1230.

(216) Saab, A. P.; Garzon, F. H.; Zawodzinski, T. a. *J. Electrochem. Soc.* **2002**, *149* (12), A1541.

(217) Kim, T.-H.; Yi, J.-Y.; Jung, C.-Y.; Jeong, E.; Yi, S.-C. *Int. J. Hydrogen Energy* **2017**, *42* (1), 478–485.

(218) Kim, Y. S.; Welch, C. F.; Mack, N. H.; Hjelm, R.; Orler, E. B.; Hawley, M.; Lee, K. S.; Yim, S. **2014**.

(219) Orfanidi, A.; Madkikar, P.; El-Sayed, H. A.; Harzer, G. S.; Kratky, T.; Gasteiger, H. A. *J. Electrochem. Soc.* **2017**, *164* (4), F418–F426.

(220) Harzer, G. S.; Orfanidi, A.; El-Sayed, H.; Madkikar, P.; Gasteiger, H. A. *J. Electrochem. Soc.* **2018**, *165* (10), F770–F779.

(221) Britton, B.; Holdcroft, S. *J. Electrochem. Soc.* **2016**, *163* (5), F353–F358.

(222) Cao, Y.-C.; Wang, X.; Scott, K. *J. Power Sources* **2012**, *201*, 226–230.

(223) Mclean, G. F.; Niet, T.; Djilali, N. *Int. J. Hydrogen Energy* **2002**, *27*, 507–526.

(224) Lu, S. F.; Pan, J.; Huang, A. B.; Zhuang, L.; Lu, J. T. *Proc. Natl. Acad. Sci. U. S. A.* **2008**, *105* (52), 20611–20614.

(225) Varcoe, J. R. *Phys. Chem. Chem. Phys.* **2007**, *9* (12), 1479–1486.

(226) Li, G.; Wang, Y.; Pan, J.; Han, J.; Liu, Q.; Li, X.; Li, P.; Chen, C.; Xiao, L.; Lu, J.; Zhuang, L. *Int. J. Hydrogen Energy* **2015**, *40* (20), 6655–6660.

(227) Thomas, O. D.; Soo, K. J. W. Y.; Peckham, T. J.; Kulkarni, M. P.; Holdcroft, S. *J. Am. Chem. Soc.* **2012**, *134* (26), 10753–10756.

(228) Henkensmeier, D.; Cho, H.-R.; Kim, H.-J.; Nunes Kirchner, C.; Leppin, J.; Dyck, A.; Jang, J. H.; Cho, E.; Nam, S.-W.; Lim, T.-H. *Polym. Degrad. Stab.* **2012**, *97* (3), 264–272.

(229) Couture, G.; Alaaeddine, A.; Boschet, F.; Ameduri, B. *Prog. Polym. Sci.* **2011**, *36* (11), 1521–1557.

(230) Li, Q.; Liu, L.; Miao, Q.; Jin, B.; Bai, R. *Polym. Chem.* **2014**, *5* (7), 2208.

(231) Wright, A. G.; Holdcroft, S. *ACS Macro Lett.* **2014**, *3* (5), 444–447.

(232) Li, C.; Wang, S.; Wang, W.; Xie, X.; Lv, Y.; Deng, C. *Int. J. Hydrogen Energy*

2013, *38* (25), 11038–11044.

(233) Yu Xu, P.; Zhou, K.; Lu Han, G.; Gen Zhang, Q.; Mei Zhu, A.; Lin Liu, Q. *J. Memb. Sci.* **2014**, *457*, 29–38.

(234) Hibbs, M. R. *J. Polym. Sci. Part B Polym. Phys.* **2013**, *51* (24), 1736–1742.

(235) Han, J.; Peng, H.; Pan, J.; Wei, L.; Li, G.; Chen, C.; Xiao, L.; Lu, J.; Zhuang, L. *ACS Appl. Mater. Interfaces* **2013**, *5* (24), 13405–13411.

(236) Ran, J.; Wu, L.; Xu, T. *Polym. Chem.* **2013**, *4* (17), 4612.

(237) Zhao, Y.; Yu, H.; Yang, D.; Li, J.; Shao, Z.; Yi, B. *J. Power Sources* **2013**, *221*, 247–251.

(238) Jiao, K.; Huo, S.; Zu, M.; Jiao, D.; Chen, J.; Du, Q. *Int. J. Hydrogen Energy* **2015**, *40* (8), 1–13.

(239) Danilovic, N.; Subbaraman, R.; Strmcnik, D.; Paulikas, a. P.; Myers, D.; Stamenkovic, V. R.; Markovic, N. M. *Electrocatalysis* **2012**, *3* (3–4), 221–229.

(240) Durst, J.; Siebel, a; Simon, C.; Hasche, F.; Herranz, J.; Gasteiger, H. a. *Energy Environ. Sci.* **2014**, *7* (2), 2255–2260.

(241) Arges, C. G.; Wang, L.; Parrondo, J.; Ramani, V. *J. Electrochem. Soc.* **2013**, *160* (11), F1258–F1274.

(242) Varcoe, J. R.; Slade, R. C. T.; Lam How Yee, E. *Chem. Commun. (Camb).* **2006**, No. 13, 1428–1429.

(243) Varcoe, J. R.; Slade, R. C. T. *Electrochem. commun.* **2006**, *8* (5), 839–843.

(244) Morris, D. R. P.; Liu, S. P.; Gonzalez, D. V.; Gostick, J. T. **2014**.

(245) Chisaka, M.; Matsuoka, E.; Daiguji, H. *J. Electrochem. Soc.* **2010**, *157* (8), B1218.

(246) Carmo, M.; Doubek, G.; Sekol, R. C.; Linardi, M.; Taylor, A. D. *J. Power Sources* **2013**, *230*, 169–175.

(247) Biros, J. *Collect.Czech.Chem.Commun.* **1972**, *37*, 3960–3964.

(248) Technique, T. D.; Chaudhari, A.; Khirade, P.; Singh, R.; Helambe, S. N.; Narain, N. K.; Mehrotra, S. C. *J. Mol. Liq.* **1999**, *82*, 245–253.

(249) Åkerlöf, G. *J. Am. Chem. Soc.* **1932**, *54* (11), 4125–4139.

(250) Maloney, J. O. *Chem. Eng. Prog.* **1952**, *48*, 192–200.

(251) Jiao, K.; He, P.; Du, Q.; Yin, Y. *Int. J. Hydrogen Energy* **2014**, *39* (11), 5981–5995.

(252) Matsumoto, K.; Fujigaya, T.; Yanagi, H.; Nakashima, N. *Adv. Funct. Mater.* **2011**, *21* (6), 1089–1094.

(253) Wang, Y.; Wang, G.; Li, G.; Huang, B.; Pan, J.; Liu, Q.; Han, J.; Xiao, L.; Lu, J.; Zhuang, L. *Energy Environ. Sci.* **2015**, *8* (1), 177–181.

(254) Stoica, D.; Alloin, F.; Marais, S.; Langevin, D.; Chappey, C.; Judeinstein, P. *J. Phys. Chem. B* **2008**, *112* (39), 12338–12346.

(255) Guo, Q.; Cayetano, M.; Tsou, Y.; De Castro, E. S.; White, R. E. *J. Electrochem. Soc.* **2003**, *150* (11), A1440.

(256) Shibayama, M.; Matsunaga, T.; Kusano, T.; Amemiya, K.; Kobayashi, N.; Yoshida, T. *J. Appl. Polym. Sci.* **2014**, *131* (3), 39842.

(257) Watanabe, M.; Tomikawa, M.; Motoo, S. *J. Electroanal. Chem. Interfacial Electrochem.* **1985**, *195* (1), 81–93.

(258) Switzer, E. E.; Olson, T. S.; Datye, A. K.; Atanassov, P.; Hibbs, M. R.; Fujimoto, C.; Cornelius, C. J. *Electrochim. Acta* **2010**, *55* (9), 3404–3408.

(259) Omasta, T. J.; Wang, L.; Peng, X.; Lewis, C. A.; Varcoe, J. R.; Mustain, W. E. *J. Power Sources* **2017**.

(260) Leng, Y.; Wang, L.; Hickner, M. A.; Wang, C. Y. *Electrochim. Acta* **2015**, *152*, 93–100.

(261) Ziv, N.; Dekel, D. R. *Electrochem. commun.* **2018**, *88* (2017), 109–113.

(262) Krewer, U.; Weinzierl, C.; Ziv, N.; Dekel, D. R. *Electrochim. Acta* **2018**, *263*, 433–446.

(263) Diesendruck, C. E.; Dekel, D. R. *Curr. Opin. Electrochem.* **2018**, 1–6.

(264) Gottesfeld, S.; Dekel, D. R.; Page, M.; Bae, C.; Yan, Y.; Zelenay, P.; Kim, Y. S. *J. Power Sources* **2018**, *375*, 170–184.

(265) Aili, D.; Wright, A. G.; Kraglund, M. R.; Jankova, K.; Holdcroft, S.; Jensen, J. O. *J. Mater. Chem. A* **2017**, *5* (10), 5055–5066.

(266) Klingele, M.; Britton, B.; Breitwieser, M.; Vierrath, S.; Zengerle, R.; Holdcroft, S.; Thiele, S. *Electrochem. commun.* **2016**.

(267) Bernhart, W.; Riederle, S.; Yoon, M.; Aulbur, W. G. *Auto Tech Rev* **2014**, *3* (3), 18–23.

(268) Marković, N. M.; Schmidt, T. J.; Stamenković, V.; Ross, P. N. *Fuel Cells* **2001**, *1* (2), 105–116.

(269) Brouzgou, A.; Song, S. Q.; Tsiakaras, P. *Appl. Catal. B Environ.* **2012**, *127*, 371–388.

(270) Dai, L.; Xue, Y.; Qu, L.; Choi, H.-J.; Baek, J.-B. *Chem. Rev.* **2015**, *115* (11), 4823–4892.

(271) Daems, N.; Sheng, X.; Vankelecom, I. F. J.; Pescarmona, P. P. *J. Mater. Chem. A* **2014**, *2* (12), 4085–4110.

(272) Smitha, B.; Sridhar, S.; Khan, A. A. *J. Memb. Sci.* **2005**, *259* (1–2), 10–26.

(273) Yee, R. S. L.; Rozendal, R. A.; Zhang, K.; Ladewig, B. P. *Chem. Eng. Res. Des.* **2012**, *90* (7), 950–959.

(274) Zhang, H.; Shen, P. K. *Chem. Rev.* **2012**, *112* (5), 2780–2832.

(275) Mehta, V.; Cooper, J. S. *J. Power Sources* **2003**, *114* (1), 32–53.

(276) De Bruijn, F. A.; Dam, V. A. T.; Janssen, G. J. M. *Fuel Cells* **2008**, *8* (1), 3–22.

(277) Vierrath, S.; Breitwieser, M.; Klingele, M.; Britton, B.; Holdcroft, S.; Zengerle, R.; Thiele, S. *J. Power Sources* **2016**, *326*, 170–175.

(278) Lefebvre, M. C. *Electrochem. Solid-State Lett.* **1999**, *2* (6), 259.

(279) Klingele, M.; Breitwieser, M.; Zengerle, R.; Thiele, S. *J. Mater. Chem. A* **2015**, *3* (21), 11239–11245.

(280) Cuynet, S.; Caillard, A.; Bigarré, J.; Buvat, P. *Int. J. Hydrogen Energy* **2017**, *42* (12), 7974–7985.

(281) Fan, J.; Wright, A. G.; Britton, B.; Weissbach, T.; Skalski, T. J. G.; Ward, J.; Peckham, T. J.; Holdcroft, S. *ACS Macro Lett.* **2017**, 1089–1093.

Appendix A. Reversible Cell Potentials in Relevant Conditions by Nernst Equation

Temp /°C	Temp /K	p_{H2} /atm	p_{O2} /atm	a_{H2O}	E_c, $H_2O_{(l)}$	p_{H2O} /atm	E_c, $H_2O_{(g)}$
0	273.15	1	1.000	1	1.229	0.006	1.18(0)
60	333.15	1	0.209	1	1.226	0.197	1.17(7)
60	333.15	1	1.000	1	1.229	0.197	1.18(0)
60	333.15	3	0.628	1	1.230	0.197	1.18(1)
60	333.15	3	3.000	1	1.233	0.197	1.18(4)
80	353.15	1	0.209	1	1.226	0.467	1.17(7)
80	353.15	1	1.000	1	1.229	0.467	1.18(0)
80	353.15	3	0.628	1	1.230	0.467	1.18(1)
80	353.15	3	3.000	1	1.233	0.467	1.18(4)
120	393.15	1	0.209	1	1.226	1.000	1.17(7)
120	393.15	1	1.000	1	1.229	1.000	1.18(0)
120	393.15	3	0.628	1	1.230	1.000	1.18(1)
120	393.15	3	3.000	1	1.234	1.000	1.18(5)

Table A1: Reversible cell potentials calculated from the Nernst equation in relevant conditions for temperature and pressure in an operating low-temperature fuel cell.

Appendix B. Comparison of PFSA and Hydrocarbon IECs

While hydrogen and fluorine atoms are very different with respect to their chemical properties, their physical sizes are quite similar. As a result, PFSAs and hydrocarbon materials could be close analogues spatially and functionally, but the PFSA will have a far higher mass per unit volume in the hydrophobic domain due to the ~19x heavier fluorine atoms in the place of hydrogens, that isn't fully accounted for by the differential in density (~2 for PFSAs and ~1.3 for sulfonated hydrocarbon PEMs). As a result, IECs for high-performance PFSAs are found in the 0.8-1.2 meq·g^{-1} range, while IECs for high-performance hydrocarbons are in the 2.25-3.5 meq·g^{-1} range. As a result, no studies cross-compare properties of these materials. However, replacing fluorines allows the calculation of a 'hydrocarbon equivalent IEC' that roughly aligns IEC-related properties between these two classes of materials.

	Hydrogen	**Fluorine**	Oxygen	Sulfur
Atomic Radius (pm)	**53**	**42**	48	87
Covalent Radius (pm)	**31**	**57**	66	105
Van der Waals Radius (pm)	**120**	**147**	152	180

Table B1: Physical properties of selected atoms.

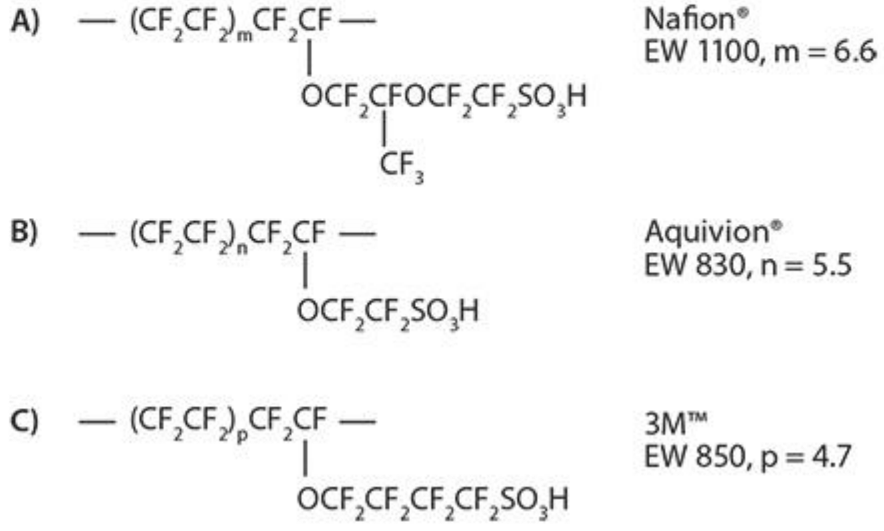

Figure B1: Common formulations of perfluonirated sulfonic acids (PFSAs), including A) the archetypal, long-chain Nafion, B) the archetypal short-chain PFSA, Solvay's Aquivion, and C) 3Mion, an early attempt at reducing side chain length.

Nafion 1100	Main repeat unit	Nafion 1100 F → H	Main repeat unit
	2 Carbons, 4 Fluorine, m = 6.6		2 Carbons, 4 Hydrogen, m = 6.6
	Side Chain repeat unit		Side Chain repeat unit
	7 Carbons, 1 Hydrogen, 13 Fluorines, 5 Oxygen, 1 Sulfur		7 Carbons, 14 Hydrogen, 5 Oxygen, 1 Sulfur
	Sum: 1104.297 (EW)		Sum: 368.800 (EW)
	IEC = 1/EW = **0.91** meq·g^{-1}		IEC = 1/EW = **2.71** meq·g^{-1}

Table B2: Simple calculation of IEC vs. the hydrocarbon equivalent IEC, IEC_{Heq}.

PFSA	IEC (meq·g^{-1})	IEC_{Heq} (meq·g^{-1})
Nafion 1100 (D521, D2021, N211, N212, N115, N117, N1110)	0.91	2.71
Nafion 1000 (D520, D2020, N105)	1.00	2.90
Aquivion 830	1.21	3.52
Aquivion 870	1.15	3.40
3Mion 850	1.08	3.20

Table B3: Results of IEC_{Heq} for common PFSAs.

Appendix C. Surface Area of Pt Nanoparticles & Produced Water

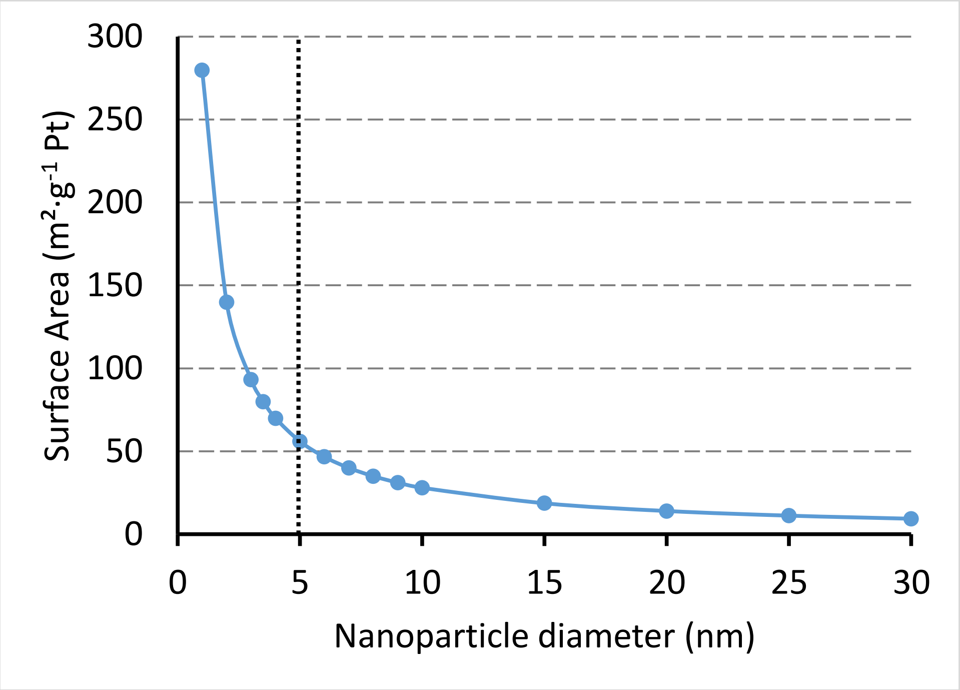

Figure C1: Nanoparticle surface area as a function of nanoparticle diameter for modelling spherical nanoparticles.

Results for surface area calculated by the equation:

$$\text{S.A.} = \frac{4\pi r^2}{\frac{4}{3}\pi r^3 \cdot \rho_{Pt}} \quad \text{(D1)}$$

Where Pt density, $\rho = 21.45\ g \cdot cm^3$. Notably, the common TKK 10e50e has a nominal nanoparticle diameter of 5 nm.

Water production per unit area of cathode is a function of current density. This can be used to describe the amount of water produced per unit time in terms of the thickness of the catalyst, i.e. water volume over infinitesimal area becomes water production as a distance in the z-direction over time, by the equation:

$$R_{H2O} = \frac{JCM_{H_2O}}{n\mathrm{N}_A\rho_{H_2O}P}$$

Where water production rate, R_{H2O} (z-direction in the CL filled with water per unit time, converted into units of $\mu m \cdot s^{-1}$) is a function of J, current density, e.g. 1 $A \cdot cm^{-2}$ with constants C, the definition of the Coulomb, $6.24 \cdot 10^{18}$ $e^{-} \cdot C^{-1}$; n representing the number of electrons required per water produced, e.g. 2 e^{-} required per H_2O produced in the acidic ORR (see eq. 1.1 for acidic cathode and 1.4 for alkaline anode water-producing reations); M_{H2O}, the molecular weight of water, 18.016 g·mol-1; N_A, Avogadro's number, 6.022·1023 mol-1; ρ_{H2O}, the density of water at 80 °C, 0.9718 $g \cdot cm^{-3}$; and P_{CL} the percent free volume in the catalyst layer in question as a measure of porosity e.g. 0.6 (60%). For the examples listed, a PEMFC operating at 1 $A \cdot cm^{-2}$ and 80 °C would fill 0.8 $\mu m \cdot s^{-1}$ of a 60% porous catalyst layer.

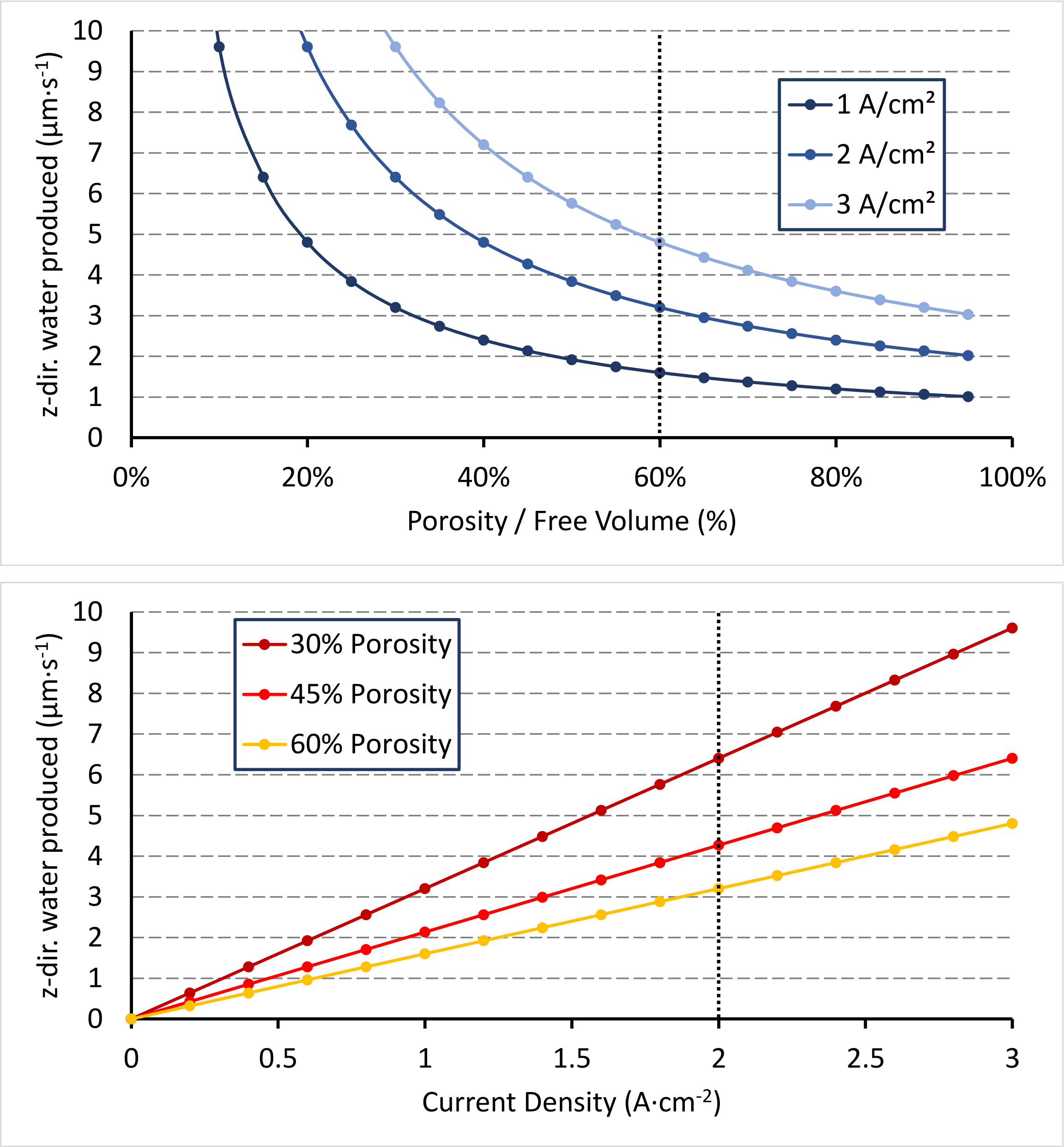

Figure C2: Water produced per unit area in acidic conditions of a water-producing CL (e.g. PEMFC cathode), A) as a function of CL porosity, showing three typical current densities in an operating fuel cell with vertical line representative of a well-formed CL and low-swelling ionomer; and B) as a function of current density showing three different typical free volumes / porosities, with vertical line representative of high power density operation in air in commercial systems.

Appendix D. Additional Manuscripts

PEMFC-Focused

4) T.J.G. Skalski, B. Britton, T.J. Peckham, and S. Holdcroft, "Structurally defined, sulfo-phenylated, oligophenylenes and polyphenylenes." J. Am. Chem. Soc., 137(38), 12223-12226 (2015).

BB: All work related to the integration of hydrocarbon PEM membranes into fuel cells with *in situ* and *ex situ* electrochemical characterization; catalyst layer study conducted but to be incorporated in a subsequent work.

5) H.F. Lee, B. Britton, Y.C. Huang, P-H Wang, Y.Y. Hsu, Y.C. Tseng, P.C. Huang, C.C. Lee, S. Holdcroft, and W.Y. Huang, "Effect of Ketone vs. Sulfone Groups on the Properties of Poly(arylene ether)-Based Proton Exchange Membranes" J. Mater. Sci., 51(21), 9805-9821 (2016).

BB: All work related to the integration of hydrocarbon PEM membranes into fuel cells with *in situ* and *ex situ* electrochemical characterization.

6) M. Adamski, T.J.G. Skalski, B. Britton, T.J. Peckham, L. Metzler, and S. Holdcroft, “Highly Stable, Low Gas Crossover, Proton-Conducting Phenylated Polyphenylenes” Angew. Chem. Intl. Ed., 129(31), 9058-9061 (2017).

BB: All work related to the integration of hydrocarbon PEM membranes into fuel cells with *in situ* and *ex situ* electrochemical characterization; catalyst layer study conducted but to be incorporated in a subsequent work.

7) H.F. Lee, M. Killer, B. Britton, Y. Wu, H.D. Nguyen, C. Iojoiu, and S. Holdcroft, “Fuel Cell Catalyst Layers and Membrane-Electrode Assemblies Containing Multiblock Poly(arylene ether sulfones) Bearing Perfluorosulfonic Acid Side Chains,” J. Electrochem. Soc., 165(10), F891-F897 (2018).

BB: Initial work in the project integrating and characterizing hydrocarbon materials as CLs, membranes, and attempts at fully hydrocarbon systems *in situ*; training.

8) T.J.G. Skalski, M. Adamski, B. Britton, E.M. Schibli, T.J. Peckham, T. Weissbach, T. Moshisuki, S. Lyonnard, B.J. Frisken, and S. Holdcroft, "Sulfophenylated Terphenylene Copolymer Membranes and Ionomers," ChemSusChem, 11(23), 4044-4043 (2018).

BB: All work related to the integration of hydrocarbon PEMs into fuel cells, as both membrane and ionomer to create fully hydrocarbon fuel cells, with *in situ* and *ex situ* electrochemical characterization; a catalyst layer and membrane with reference electrodes study also conducted but to be incorporated in a subsequent work.

AEMFC-Focused

9) A.G. Wright, J. Fan, B. Britton, T. Weissbach, H-F. Lee, E.A. Kitching, T.J. Peckham, and S. Holdcroft, "Hexamethyl-p-terphenyl poly(benzimidazolium): a universal hydroxide-conducing polymer for energy conversion devices," Energy Environ. Sci., 9, 2130-2142 (2016).

BB: All work related to the integration and characterization of hydrocarbon membranes and catalyst layer into fuel cells and alkaline membrane electrolyzers, including the development of both *in situ* and *ex situ* conditioning protocols; the development of lifetime and performance characterization methodologies; *in situ* electrochemical and *ex situ* physical characterization; construction of and method development for the alkaline membrane electrolysis test system; AEM water electrolysis MEA fabrication and subsequent electrochemical characterization using the test system.

10) M. Klingele, C. Van Pham, K.R. Vuyyuru, B. Britton, S. Holdcroft, A. Fischer, S. Thiele, "Sulfur doped reduced graphene oxide as metal-free catalyst for the oxygen reduction reaction in anion and proton exchange fuel cells," Electrochem. Comm., 77, 71-75 (2017).

BB: All electrode formulation development and MEA fabrication, with interaction on characterization of these MEAs subsequently performed at IMTEK (Freiburg).

11) C. Van Pham, M. Klingele, B. Britton, K.R. Vuyyuru, T. Unmuessig, S. Holdcroft, A. Fischer, and S. Thiele, "Tridoped Reduced Graphene Oxide as a Metal-Free Catalyst for Oxygen Reduction Reaction Demonstrated in Acidic and Alkaline Polymer Electrolyte Fuel Cells," Adv. Sustainable Syst., 1(5), 160038;1-10 (2017).

BB: All electrode formulation development and MEA fabrication, with interaction on characterization of these MEAs subsequently performed at IMTEK (Freiburg).

12) J. Fan, A.G. Wright, B. Britton, T. Weissbach, T.J.G. Skalski, J. Ward, T.J. Peckham, and S. Holdcroft, “Cationic Polyelectrolytes, Stable in 10 M KOHaq at 100 °C,” ACS Macro Lett., 6, 1089-1093 (2017).

BB: The integration of hydrocarbon AEMFC membranes and ionomers as fuel cells with *in situ* and *ex situ* electrochemical characterization; significant method development for *in situ* characterization at high temperatures.

13) C. Van Pham, B. Britton, T. Böhm, S. Holdcroft, and S. Thiele, “Doped, Defect-Enriched Carbon Nanotubes as an Efficient Oxygen Reduction Catalyst for Anion Exchange Membrane Fuel Cells,” 5, 1800184;1-9 (2018).

BB: All electrode formulation development and MEA fabrication, with interaction on characterization of these MEAs subsequently performed at IMTEK (Freiburg).

DMD-Focused

14) M. Breitwieser, M. Klingele, B. Britton, S. Holdcroft, R. Zengerle, and S. Thiele. "Improved Pt-utilization efficiency of low Pt-loading PEM fuel cell electrodes using direct membrane deposition," Electrochem. Comm. 60, 168-171 (2015).

BB: Extension of method development in Chapter 3; all GDE fabrication with interaction on characterization of these MEAs subsequently performed at IMTEK (Freiburg).

15) S. Vierrath, M. Breitwieser, M. Klingele, B.Britton, S. Holdcroft, R. Zengerle, S. Theiele, “The reasons for the high power density of fuel cells fabricated with directly deposited membranes,” J. Power Sources, 326, 170-175 (2016).

BB: All GDE fabrication with interaction on characterization of these MEAs subsequently performed at IMTEK (Freiburg).